Simulating DNA Behavior in Microfluidic Devices

by

Daniel Warner Trahan

B.S. Chemical Engineering, Rice University (2005),
M.S. Chemical Engineering Practice, Massachusetts Institute of Technology (2008).

Submitted to the Department of Chemical Engineering
in partial fulfillment of the requirements for the degree of

Doctor of Philosophy in Chemical Engineering

at the

MASSACHUSETTS INSTITUTE OF TECHNOLOGY

August 2010
[September 2010]

Author_____
Department of Chemical Engineering
August 27, 2010

Certified by_____
Patrick S. Doyle
Doherty Associate Professor of Chemical Engineering
Thesis Supervisor

Accepted by_____
William M. Deen
Chairman, Department Committee on Graduate Students

Simulating DNA Behavior in Microfluidic Devices

by
Daniel Warner Trahan

Submitted to the Department of Chemical Engineering
on August 27, 2010, in partial fulfillment of the
requirements for the degree of
Doctor of Philosophy in Chemical Engineering

Abstract

During most of the twentieth century, direct study of individual polymer molecules was impossible due to their small size. Therefore, polymers were typically studied in bulk solutions, and their behavior and interactions had to be understood through average bulk property measurements. Because the scale of most industrial applications greatly exceeded the size of these molecules, this level of analysis was satisfactory. In the last twenty years, however, the appearance of microfluidic devices, whose smallest length scales are comparable to the size of a polymer molecule, has offered ways to visually study the behavior of individual polymer molecules and made possible new and exciting applications that exploit the precise control afforded by the small size of these devices.

One such application is gene mapping, which extracts, at a coarse level, the information embedded in the base pair sequence of genomic DNA. This technology relies on the ability to manipulate single DNA molecules in order to perform such tasks as separating DNA based on length and stretching DNA away from its entropically coiled equilibrium state. Recently, many novel methods have been proposed to accomplish these tasks using microfabricated devices, and much experimental work has been focused on identifying and characterizing the underlying physics governing these devices. Current understanding, however, is greatly hampered by the fact that experiments can only provide limited information about the behavior of DNA molecules (e.g., they are unable to resolve details on small time and length scales). Therefore, simulations are an invaluable tool in the study of DNA behavior in microfluidic devices by complementing and guiding experimental investigations.

In this thesis, we present Brownian Dynamics simulations of the single molecule behavior of DNA in microfluidic devices related to gene mapping. In particular, we have considered the use of a post array to "precondition" the configuration of molecules for subsequent stretching in a contraction and compared our results to previous experiments. We found good qualitative agreement between experiments and simulations for DNA behavior in the post array, but our simulations consistently overpredicted the final stretch of molecules at the end of the contraction, which we attributed to nonlinear electrokinetic effects. We also investigate the electrophoretic collision of a DNA molecule with a large, ideally conducting post. Field-induced compression was shown to play a critical role in the escape process of a molecule trapped on the post surface, and an extensive theoretical analysis is performed, describing both the local field-induced compression and the larger collision problem. Finally, we study the relaxation process of an initially stretched molecule in slitlike confinement. We present the first simulation results that exhibit two distinct relaxation times in the linear force regime, as previously reported in recent experiments. Our analysis is focused on the experimentally

inaccessible dynamics in the transverse directions, particularly at short times and on small length scales. Comparisons to the predictions of a recent mechanistic model of confined relaxation were found to be satisfactory.

Thesis Supervisor: Patrick S. Doyle
Title: Doherty Associate Professor of Chemical Engineering

Acknowledgments

A PhD thesis is a journey. Certainly it is an academic endeavor, a type of intellectual odyssey, but it is much more than this. It is also a personal exploration, a time for self-discovery. You learn about yourself. You are tested. You find that you have limits but also that you have more strength than you knew. A thesis evolves over five years of your life, and the chapters evoke memories of all that transpired during that time. Each page contains a story hidden between the lines that no outsider can possibly read. And like any good story or play, there are many characters along the way. Mine is certainly no different.

The principal player during my thesis was my adviser Professor Pat Doyle. He guided my work, always challenging me to think deeply about the task at hand. In his group, I learned to choose problems of significance and to approach them ambitiously. He trained me to think about problems starting from fundamentals and to not be tempted to treat them superficially. I am deeply indebted to him for his tutelage.

The award for best supporting actor certainly goes to my partner Matt. He was my rock through years of volatile emotions, sharing in my disappointments and triumphs alike. Many late nights in the office were brightened by personal deliveries of food, despite his own long days at the hospital. I truly believe that it is only with his constant support and encouragement that I was able to complete this thesis.

I think my family played the role of the audience. They may have watched my story unfold from afar, but they never failed to applaud vigorously at the end of each act. I am deeply grateful to

my parents for always pushing me to do the best that I can, while still offering unwavering support when I fall short. And to my sister Denise, I say, "Thank you," for all our conversations where I can freely vent my frustrations of the day.

My numerous friends provided the backup that I desperately needed over my graduate career, but I can only name a few here. I have to give special recognition to Gary Chia. Although I did not remember him from the first time we met during our prospective visit to MIT, I could never forget him now. I will also greatly miss Andrew Guerra and Bradley Niesner. Our brunches always reinvigorated me for a long week (and probably provided me with some of my only sustenance for the week as well!). Thank you to Kathryn Macapagal for commiserating with me about the life of a graduate student.

Of course, there were many other important players along the way, especially in the Doyle group. In particular, I must thank Jing Tang for his help over the past five years. Whether it was at Practice School or in the office, he was always there to listen to my ideas and to offer his suggestions. I can only hope that I have done the same. I owe Pat Underhill and Ju Min Kim a great deal of thanks for their guidance when I first joined the Doyle group. Anthony Balducci, Chih-Chen Hsieh, and Will Uspal all deserve my gratitude for patiently answering my endless stream of questions. And to Priyadarshi Panda and Jason Rich, thank you for approaching me with your research problems that allowed me to feel useful and provided needed distractions from my own.

Table of Contents

List of Figures

List of Tables

CHAPTER 1

Introduction

1.1 Motivation

1.1.1 Gene Mapping

The human genome contains most of the details required both to construct a complete individual and to maintain his or her continuous functioning for a lifetime. Accordingly, the amount of information stored within the sequence of the constituent base pairs is massive and complex. It specifies such mundane traits as hair and eye color, while also defining more significant features, including an individual's susceptibility to myriad maladies, such as cancer and disease. Indeed, it also encodes the body's response to these same afflictions.

Consequently, a great deal of effort has been expended to determine the exact sequence of the entire human genome [1]. This considerably detailed information is then used by researchers for varied purposes, from locating particular genes within the vast sequence, to studying how the genetic material is regulated and interacts with its cellular environment. However, many diverse applications do not require fine detail about the exact sequence of individual base pairs, including gene therapy and medical diagnostics, identification and crime investigation, and even national defense programs. In these cases, performing DNA sequencing is excessive, and gene "mapping" techniques, which are less expensive and provide lower resolution than sequencing, are sufficient.

DNA or gene mapping involves determining the location of different short base pair sequences or genes relative to one another. This coarser view of the genome is faster and cheaper to obtain and

more accessible to analysis for the aforementioned applications. Most mapping techniques currently rely on indirect methods of obtaining these relative locations, typically by restriction mapping [2]. In this technique, restriction enzymes cut DNA at specific sequences to form short strands of many different lengths which are then length-separated, often by gel electrophoresis. By using multiple sets of restriction enzymes, the various band patterns that are obtained can be interpreted to construct a map of the genome. This technique, however, has several major drawbacks. Firstly, it often requires numerous sets of restriction enzymes and many separations to obtain the correct mapping, and secondly, separations, particularly gel electrophoresis, are time consuming and have upper limits on the length of the strands that can be resolved [3]. Therefore, the development of a method to rapidly map large, genomic length DNA molecules is highly desirable.

Two different paths have been followed to attack this problem. The first is to optimize methods that rely upon indirect analysis by devising novel separation techniques that are faster and and able to separation large DNA molecules. The second route is to engineer a direct analysis method that completely bypasses the need to perform separations.

Indirect Analysis: Separations

Indirect gene mapping techniques rely upon the ability to separate fragments of DNA based upon their length. This has traditionally been accomplished through gel electrophoresis, where the gel network acts as a "sieve." However, gel electrophoresis is not possible for many of the large DNA strands seen in modern gene mapping. This is because the pore size of the gel cannot be made large enough to efficiently separate large molecules without compromising the integrity of the gel. Therefore, there has been considerable interest in developing new techniques that allow for the rapid separation of large DNA strands.

Many studies have relied upon the same basic sieving mechanism found in gel electrophoresis but have exploited microfluidics to design devices with "artificial pores" whose size and geometry can be chosen arbitrarily and precisely controlled by microfabrication techniques. Volkmuth and Austin [4] pioneered this technique by electrophoresing DNA through an array of microfabricated posts. It was observed that molecules tended to "hook" on the posts leading to a size-dependent unhooking process [5, 6, 7, 8, 9, 10]. Arrays of variously shaped obstacles have also been used to create diffusion arrays [11, 12, 13] where small molecules with high diffusivities tend to follow tortuous paths through the array while large molecules typically move quickly through the channels between the obstacles. Confinement effects have also been exploited for separation purposes. Nanochannels with varying cross-sections have been constructed to create entropic traps [14, 15, 16] which have an entropic energy barrier to move from regions of wide cross-section to those with a narrow cross-section. Nanopores have also been used for separations by exploiting the entropic recoil [17, 18, 19] of a molecule that is partially inserted in a nanopore. Some studies have not relied upon device geometries to achieve separation. For example, one technique attaches uncharged molecules to the end of DNA to act as a sort of "parachute" during electrophoresis leading to size-dependent mobility [20]. All of the separation techniques, however, tend to suffer from limited resolution, particularly for large molecules and when operated at high speeds.

Direct Analysis: Stretching

Direct analysis techniques attempt to literally "read off" the location of genes and specific base sequences directly from a single molecule of intact DNA, thereby circumventing the separation prob-

lem entirely. The most promising example of this technique is called direct linear analysis (DLA) [2]. In this method, a DNA molecule is labeled with fluorescent tags (often modified biomolecules) that attach to specific sequences of interest. The DNA molecule is then stretched into a straight line and driven past a detector which uses optical sensors to measure the physical distance between the fluorescent tags along the DNA backbone (see Figure 1.1). This provides a simple, direct, and easily analyzed physical map of the molecule. The advantages to this technique are that it is fast, it works for large DNA strands, and can easily be automated in a microfluidic device.

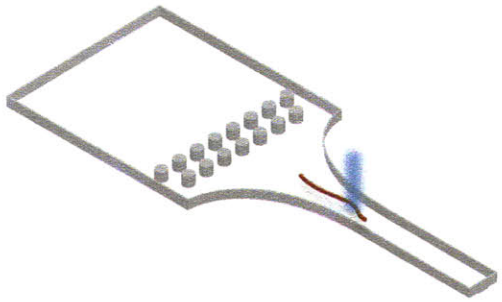

Fig. 1.1: *Visualization of a Direct Linear Analysis (DLA) device. The hyperbolic contraction creates an elongational flow to stretch the DNA (shown in red), and the array of posts pre-conditions the chain configurations before it enters the contraction to be analyzed by a sensor (shown in blue).*

On the other hand, a major difficulty with DLA currently is overcoming the entropic tendency of polymeric DNA to adopt a coiled configuration which is unsuitable for optical analysis. Therefore, developing effective methods to consistently stretch DNA molecules close to their full contour length in a continuous and uniform manner is paramount to the success of DLA devices. It has been shown that electric field gradients can accomplish this task [21, 22], and stretching DNA in electric fields is similar to stretching polymers in hydrodynamic flow fields [23]. Electric fields, however, are better suited to stretch DNA in microfluidic devices: they are simple to apply and are purely elongational. Even so, stretching DNA with field gradients suffers from a phenomenon termed "molecular individualism" [24]. This refers to the nonuniform way a population molecules stretches due to the random nature of their initial configurations. This is a significant obstacle that must be overcome since DLA requires a uniformly stretched population of molecules to accurately determine the distance between the tags.

1.1.2 Polymer Physics of Confinement

During much of the twentieth century, the scale of most industrial applications greatly exceeded the size of individual polymer molecules. This meant that the molecules were never physically confined and any fields or forces applied to the molecules looked homogeneous on the length scale of a polymer chain [25]. Therefore, a great deal of research examining bulk properties and homogeneous flow fields was completed. In the last twenty years, however, the appearance of microfluidic devices, whose smallest length scales are typically near the size of the polymer, has created a need to study

polymer behavior in confined environments and in non-homogeneous flow fields that vary over the length scale of the polymer [26, 27, 21]. Already, there has been theoretical work done on the behavior of polymers in confinement [28, 29]; however, experiments have only recently begun to catch up with the theory [30, 31, 32]. An understanding of the equilibrium properties and the dynamics of confined polymers is fundamentally important to the rational design of future novel devices. It will allow researchers to exploit the advantages of confinement, while avoiding and overcoming the obstacles it presents.

1.2 Objectives

The goal of this research is to develop an understanding of the behavior of DNA in microfluidic devices that have potential application in gene mapping. In particular, we are interested in studying the effects of confined environments and small length scale device features (e.g., microfabricated posts) on the properties and dynamics of DNA. We examine how post arrays can effect conformational changes in a population of molecules, and we consider two types of slitlike confinement: physical confinement imposed on a molecule by the channel geometry, and field-induced confinement when a molecule is pushed against a flat surface by a transverse field. We attack these problems with a combination of heavy theory and Brownian Dynamics simulations. The following studies will be presented:

- Conformational preconditioning by a microfabricated array of posts;
- Electrophoretic collisions of DNA molecules with a large, ideally conducting post;
- Relaxation of an initially stretched DNA molecule in slitlike confinement.

1.3 Overview of Results

In Chapter 2, we present a primer on general polymer physics that will be useful to understanding our studies. In addition, some of the important work in the field is reviewed along with an introduction to our simulation technique. Chapter 3 presents the results of a study on using collisions with an array of posts to conformationally precondition DNA molecules for subsequent stretching in a contraction. This creates a more uniform distribution for the stretch of the polymers in the array during gene mapping analysis. Chapter 4 lays out the first study to consider the electrophoretic collision of a DNA molecule with a conducting post. These collisions are qualitatively different from those with insulating posts, which have been studied extensively. The phenomenon of field-induced confinement is also exhaustively studied. Chapter 5 investigates the relaxation of DNA in slitlike confinement. The findings are compared to the predictions of a recently developed mechanistic model, and good agreement is found. Finally, in Chapeter 6, the results of our research are briefly summarized and their impact assessed. We also discuss the future directions suggested by our work.

CHAPTER 2

Background

In this chapter, we present the much of the basic background to understand the work contained in this thesis. To begin, we present a general review of the most important physics that affects polymer dynamics in confinement. We then offer a survey of some of the literature surrounding specific problems studied in this work. Finally, we consider the idea of coarse-graining and mesoscopic simulation techniques that will be used throughout this thesis.

2.1 General Polymer Physics

A polymer is a large molecule consisting of many, often repeating, elementary units, called monomers. These chemical subunits are connected together via covalent bonds to form a long chain that can adopt myriad conformations. This diversity of possible spatial arrangements confers upon polymers many of their unique properties. In fact, polymers have been studied with interest because their global structure can be profoundly affected by the local behavior of its constituent building blocks, including the flexibility of the chain, interactions between monomers along the chain, and interactions of the chain with its surroundings. This provides the scientist or engineer with many ways to manipulate polymers and fine-tune their equilibrium and dynamic properties to the situation at hand. However, in order to this in a rational manner, a basic understanding of the properties of polymers at their most fundamental level must be established.

In this section, we present the... general polymer physics including equilibrium properties and dynamic behavior. We present several physical models used to study and represent polymers. We also begin to introduce the idea of coarse-graining which is important to being able to distill out the essential physics while keeping the analysis tractable.

2.1.1 Equilibrium Properties

At its simplest, a polymer can be described as a collection of N rods of length ℓ connected end-to-end to form a linear chain. The rods are representative of the underlying structural subunits of the chain such as the chemical monomers. There are several length scales and measures of the chain's conformation that are significant. The simplest is the contour length of the chain L_c. As its name implies, this is defined as the total length of the chain as measured along the chain backbone and is given by $L_c = N\ell$. The contour length is the maximum length to which a polymer can be stretched, and it represents the largest length scale of the chain.

Coil Size

To describe the conformation of the chain, each segment is assigned a "bond vector" $\mathbf{r}_i$ of length ℓ that points in the direction that the ith rod is oriented. The most straightforward descriptor of the chain's conformation is the end-to-end vector $\mathbf{R}_{ee}$. This is defined as the vector connecting the two ends of the chain and is found by summing all of the N bond vectors

$$\mathbf{R}_{ee} = \sum_{i=1}^{N} \mathbf{r}_i. \tag{2.1}$$

Because at equilibrium a chain is isotropic, there is no preferred orientation of the bonds. Therefore, the ensemble averaged end-to-end vector for a polymer in bulk at equilibrium is zero

$$\langle \mathbf{R}_{ee} \rangle = \left\langle \sum_{i=1}^{N} \mathbf{r}_i \right\rangle = \sum_{i=1}^{N} \langle \mathbf{r}_i \rangle = \mathbf{0}. \tag{2.2}$$

The second moment of $\mathbf{R}_{ee}$, however, is non-zero. The average end-to-end vector squared can be written as

$$\langle {\mathbf{R}_{ee}}^2 \rangle = \langle \mathbf{R}_{ee} \cdot \mathbf{R}_{ee} \rangle = \left\langle \left(\sum_{i=1}^{N} \mathbf{r}_i \right) \cdot \left(\sum_{j=1}^{N} \mathbf{r}_j \right) \right\rangle = \sum_{i=1}^{N} \sum_{j=1}^{N} \langle \mathbf{r}_i \cdot \mathbf{r}_j \rangle = \ell^2 \sum_{i=1}^{N} \sum_{j=1}^{N} \langle \cos\theta_{ij} \rangle , \tag{2.3}$$

where θ_{ij} is the angle between bond vectors $\mathbf{r}_i$ and $\mathbf{r}_j$. The most basic polymer model is the freely jointed chain (FJC). In this case, the angle between different bond vectors is entirely uncorrelated at equilibrium so that $\langle \cos_{ij} \rangle = \delta_{ij}$, where δ_{ij} is the Kronecker delta, and therefore,

$$\langle {\mathbf{R}_{ee}}^2 \rangle = \ell^2 \sum_{i=1}^{N} \sum_{j=1}^{N} \delta_{ij} = N\ell^2. \tag{2.4}$$

Taking the square root of this quantity gives the root mean square of the end-to-end vector

$R_{ee} = \sqrt{\langle \mathbf{R}_{ee}{}^2 \rangle}$, which is often referred to as the end-to-end distance. R_{ee} represents the most rudimentary characteristic length of the chain's size at equilibrium. For the FJC, $R_{ee} = N^{1/2}\ell$ which is significantly smaller than L_c. In fact, the fractional extension of the end-to-end distance $X_{ee} = R_{ee}/L_c = N^{-1/2} \ll 1$ and decreases as the number of rods N increases.

On the other hand, a more realistic model for a polymer should acknowledge that neighboring bond vectors are correlated. For example, long alkane molecules contain a carbon backbone where the carbon atoms are able to rotate around the bonds but the angle between two successive bonds varies little. The simplest model to incorporate such correlations is the freely rotating chain (FRC). In this case, θ_{ij} is assumed to have a constant value of θ between neighboring bonds, and through a recursion formula, $\langle \cos_{ij} \rangle$ can be shown to decay as the distance between bonds increases:

$$\langle \cos\theta_{ij} \rangle = (\cos\theta)^{|j-i|}. \tag{2.5}$$

This decay is very rapid and is readily apparent when the RHS of Equation 2.5 is recast as

$$(\cos\theta)^{|j-i|} = \exp\left[|j-i|\ln(\cos\theta)\right] = \exp\left(-\frac{|j-i|}{s_p}\right), \tag{2.6}$$

where $s_p = -1/\ln(\cos\theta)$ and represents the number of rods over which the correlations between bond angles decay. This allows us to describe another length scale, the persistence length $\ell_p = s_p\ell$, which is the contour length over which directional correlations die off between different segments of the chain.

The end-to-end distance squared for the FRC can be written as

$$\begin{aligned} R_{ee}{}^2 = \langle \mathbf{R}_{ee}{}^2 \rangle &= \ell^2 \textstyle\sum_{i=1}^{N}\sum_{j=1}^{N} (\cos\theta)^{|j-i|} \\ &= \ell^2 \left\{ N + \textstyle\sum_{i=1}^{N} \left[\sum_{j=1}^{i-1} (\cos\theta)^{i-j} + \sum_{j=i+1}^{N} (\cos\theta)^{j-i} \right] \right\} \\ &= \ell^2 \left[N + \textstyle\sum_{i=1}^{N} \left(\sum_{k=1}^{i-1} \cos^k\theta + \sum_{k=1}^{N-i} \cos^k\theta \right) \right]. \end{aligned} \tag{2.7}$$

Because the correlations decay exponentially, we can extend the sums over k to infinite series:

$$\sum_{i=1}^{N} \left(\sum_{k=1}^{i-1} \cos^k\theta + \sum_{k=1}^{N-i} \cos^k\theta \right) = 2\sum_{i=1}^{N}\sum_{k=1}^{\infty} \cos^k\theta = 2N\sum_{k=1}^{\infty} \cos^k\theta = 2N\frac{\cos\theta}{1-\cos\theta}. \tag{2.8}$$

So for the FRC

$$R_{ee}{}^2 = N\ell^2\frac{1+\cos\theta}{1-\cos\theta}. \tag{2.9}$$

As in the case of the FJC, the equilibrium size of the FRC is much smaller than the contour length. Additionally, the size of the FRC has the same scaling with N. In fact, this is a general property of all chain models that take into account only local interactions and correlations along the chain and neglect all interactions between distant segments. Models based upon this assumption are referred to as ideal chain models.

The equilibrium size of an ideal chain is always of the form

$$R_{ee}{}^2 = C_\infty N\ell^2, \tag{2.10}$$

where C_∞ is Flory's characteristic ratio and is a proportionality constant that represents the ratio of the chain's ${R_{ee}}^2$ to that of the FJC (i.e., $N\ell^2$). This universal behavior is a consequence of the Central Limit Theorem. In the case of the FRC, the characteristic ratio is

$$C_\infty = \frac{1+\cos\theta}{1-\cos\theta}. \tag{2.11}$$

Ideal chains can always be recast to behave like the FJC in a model known as the equivalent freely jointed chain. In order to do this, an effective bond length called the Kuhn length b_K is introduced. The equivalent chain must have the same contour length as the old chain, so the number of Kuhn "monomers" is given by $N_\mathrm{K} = N\ell/b_\mathrm{K}$. The Kuhn length is chosen, so that the equivalent chain has the same ${R_{ee}}^2$ as a FJC (i.e., $N_\mathrm{K}{b_\mathrm{K}}^2 = C_\infty N\ell^2$). From these equalities, the equivalent freely jointed chain is defined by

$$b_\mathrm{K} = C_\infty \ell \text{ and } N_\mathrm{K} = \frac{N}{C_\infty}. \tag{2.12}$$

The final ideal chain model that will be discussed is the worm-like chain (or Kratky-Porod model). This model is used to describe very stiff polymers that tend to bend continuously over long length scales rather than have sharp turns or kinks as in the standard FJC or FRC models. In particular, it is used to model the fairly rigid DNA double helix and, therefore, is of considerable importance to the present work.

The worm-like chain is actually a special case of the FRC model for very small values of θ. For $\theta \ll 1$, the Flory characteristic ratio is given by

$$C_\infty = \frac{1+\cos\theta}{1-\cos\theta} \approx \frac{2-\theta^2/2}{\theta^2/2} \approx \frac{4}{\theta^2}, \tag{2.13}$$

where we have used the the fact that $\cos\theta \approx 1-\theta^2/2$ for θ near zero. It can also be shown that the persistence length is given by

$$\ell_p = s_p\ell = \frac{-\ell}{\ln(\cos\theta)} \approx \frac{2\ell}{\theta^2}, \tag{2.14}$$

where the identity $\ln(1-x) \approx -x$ for small x has been used. With these two expressions, we can find the relation between the Kuhn length and the persistence length for the worm-like chain:

$$b_\mathrm{K} = C_\infty \ell \approx \frac{4\ell}{\theta^2} \approx 2\ell_p. \tag{2.15}$$

So for the worm-like chain, the Kuhn length is twice the persistence length ($b_\mathrm{K} \approx 2\ell_p$). As can be seen in Equation 2.15, the ratio ℓ/θ^2 defines both the Kuhn length and the persistence length. The true worm-like chain is defined in the limits $\ell \to 0$ and $\theta \to 0$ while both ℓ_p and $L_c = N\ell$ remain constant. In this limit, the chain becomes a continuous smooth curve with a bending potential and the mean-square end-to-end distance is found by considering the decay of the directional correlations

along the chain backbone:

$$R_{ee}{}^2 = \ell^2 \sum_{i=1}^{N}\sum_{j=1}^{N} (\cos\theta)^{|j-i|} = \ell^2 \sum_{i=1}^{N}\sum_{j=1}^{N} \exp\left(\frac{-|j-i|\ell}{\ell_p}\right). \tag{2.16}$$

By converting the discrete summations long the bond vectors to continuous integrals over the chain contour length, it can be shown that

$$R_{ee}{}^2 = 2\ell_p L_c - 2\ell_p{}^2\left[1 - \exp\left(\frac{-L_c}{\ell_p}\right)\right]. \tag{2.17}$$

For our present work, we are interested in the long chain limit $L_c \gg \ell_p$ so that $R_{ee}{}^2 \approx 2\ell_p L_c = N_K b_K{}^2$, which is precisely the result expected for any ideal chain model.

The last topic we will consider concerning the equilibrium size of an ideal chain is the radius of gyration R_g. The end-to-end distance R_{ee} is typically not directly obtainable from experiments. For example, in single molecule fluorescent microscopy, the ends of the molecule are indistinguishable from other segments of the chain. Additionally, the end-to-end distance is only well defined for linear chains. Therefore, a measure of the chain size based on an average over all of the chain segments is needed. The square radius of gyration is defined as

$$R_g{}^2 = \frac{1}{N_K}\sum_{i=1}^{N_K} (\mathbf{R}_i - \mathbf{R}_{cm})^2, \tag{2.18}$$

where $\mathbf{R}_i$ is the position of the ith Kuhn monomer and $\mathbf{R}_{cm} = \sum_{i=1}^{N} \mathbf{R}_i$ is the center of mass of the chain. The equilibrium averaged square radius of gyration is given by

$$\left\langle R_g{}^2 \right\rangle = \frac{1}{N_K{}^2}\sum_{i=1}^{N_K}\sum_{j=i}^{N_K} \left\langle (\mathbf{R}_i - \mathbf{R}_j)^2 \right\rangle = \frac{N_K b_K{}^2}{6} = \frac{\left\langle \mathbf{R}_{ee}{}^2 \right\rangle}{6}. \tag{2.19}$$

This result is obtained by converting the discrete summations to continuous integrals and making use of the fact that the mean-square distance $R_{ij}{}^2$ between any two Kuhn monomers i and j is given by the FJC result (i.e., $R_{ij}{}^2 = |j-i| b_K{}^2$). For an ideal chain, the radius of gyration is related to the end-to-end distance by a simple, constant numerical factor $R_g = R_{ee}/\sqrt{6}$. Again, it is clear that the equilibrium size of the chain is much smaller than its maximum possible extension L_c.

In fact, this is a general feature of polymers. At equilibrium, they exist as "coils" whose sizes are much smaller than that of their contour lengths, and the two measures continue to diverge further as the numbers of constituent segments are increased. This is entirely due to entropy, and in fact, a force is required to deform a chain away from its equilibrium coil size.

Elasticity

At equilibrium, a polymer is a fluctuating object that samples all of its possible configurations. Many more configurations are available to the polymer when it adopts a coiled state than when it is extended. A consequence of this fact, is that any attempt to deform the polymer chain away from its equilibrium size to a more extended state, leads to a reduction in the number of configurations

available to the chain. This reduction in the available configuration space induces an opposing force that attempts to return the chain to its equilibrium size. Therefore, any device or method that aims to stretch a polymer molecule such as DNA, must overcome this entropic "spring" force.

A scaling approach is instructive for understanding the origin of this force and for obtaining its analytical form. The key to this scaling approach is to

This scaling method is accomplished by using a tension blob framework. A polymer molecule can be represented as a string of N_T "submolecules" each containing g_T Kuhn monomers such that $(N_T g_T) b_K = L_c = N_K b_K$. The number of submolecules is, therefore, given by

$$N_T = \frac{N_K}{g_T}. \tag{2.20}$$

As long as $g_T \gg 1$, then the statistics of the FJC discussed in Section 2.1.1 can be used to describe each submolecule. This means that the equilibrium coil size of a submolecule follows the scaling $\sim b_K \sqrt{g_T}$. Now, we must recognize that a force f applied to the ends of a polymer molecule deforms the global structure of the chain, but locally along the chain, the organization of the Kuhn monomers tends to remain unperturbed from the equilibrium configurations predicted by the FJC model. This means there is a length scale ξ_T above which the chain appears deformed, but below this length scale, the chain segments appear near equilibrium. If we allow ξ_T to be the size of our submolecules or "tension blobs", then we can say that equilibrium FJC chain statistics apply within the blobs:

$$\xi_T{}^2 \sim g_T b_K{}^2. \tag{2.21}$$

But on lengths greater than the ξ_T, the blobs tend to align in the direction of stretch, so that the stretched length of the molecule R can be approximated by the total length of the string of blobs:

$$R \sim N_T \xi_T. \tag{2.22}$$

In order to determine the energy $F(R)$ required to extend the molecule to a length of R, we note that the alignment of each blob along the direction of stretch restricts a degree of freedom of the chain. Each degree of freedom removed from the system requires an energy on the order of $k_B T$, so

$$F(R) \sim N_T k_B T \sim k_B T \frac{R^2}{N_K b_K{}^2}, \tag{2.23}$$

where N_T is obtained from considering Equations 2.20-2.22. To obtain the entropic restoring force $f(R)$, we simply differentiate the negative of the energy with respect the stretched length:

$$f(R) = -\frac{\partial F}{\partial R} \sim -k_B T \frac{R}{N_K b_K{}^2}. \tag{2.24}$$

So the entropic spring force is linear with Hookean spring constant $H \sim k_B T / N_K b_K{}^2$. This also suggests that probability distribution function for the end-to-end vector $P(\mathbf{R}_{ee})$ is Gaussian, and in fact, a more detailed calculation based upon the statisitics of random walks bears this out:

$$P(\mathbf{R}_{ee}) = \left(\frac{3}{2\pi N_K b_K{}^2} \right)^{3/2} \exp\left(-\frac{3 \mathbf{R}_{ee}{}^2}{2 b_K{}^2} \right). \tag{2.25}$$

This expression is valid for long chains and end-to-end distances much smaller than the contour length (i.e., $N_K \gg 1$ and $R \ll N_K b_K$) and is, again, a consequence of the Central Limit Theorem. That the distribution of Kuhn monomer positions is Gaussian is an important result of ideal chain models and is often used to analytically study problems in the polymer physics literature. Indeed, we shall make use of this result in our present work as well. For now, we note that we can derive the exact linear spring force for an ideal chain from Equation 2.25:

$$f(R) = -\frac{3k_BT}{N_K {b_K}^2} R. \tag{2.26}$$

Nonlinearities

There is a problem with the linear force law given by Equation 2.26. It clearly allows the chain to be stretched beyond its contour length, which is clearly aphysical. As previously mentioned, the linear force law is only applicable when the chain's extension is much less than its maximum extension. Our tension blob model can explain why this is.

We assumed that the configurations of the Kuhn segments within each blob are unperturbed by the stretching. However, at some point the chain is so stretched that the size of blob approaches that of a Kuhn segment. At this point, the chain configuration is perturbed from its equilibrium at all length scales, and the force law becomes nonlinear. As the chain extension approaches the contour length, the force diverges, making it impossible to stretch a chain beyond its maximum extension. A detailed statistical mechanics analysis shows that the exact force-extension behavior of the FJC is given by

$$\frac{R}{L_c} = \mathcal{L}\left(\frac{fb_K}{k_BT}\right) = \coth\left(\frac{fb_K}{k_BT}\right) - \left(\frac{fb_K}{k_BT}\right)^{-1}, \tag{2.27}$$

where $\mathcal{L}(x)$ is called the Langevin function. This force law recovers the expected linear behavior at low extensions and diverges as the chain approaches its maximum extension.

The way the spring law diverges changes depending upon the nature of the local, small length scale detail of the chain. For example, the worm-like chain bends continuously unlike the FJC, which is composed of solid rods connected by free hinges. Therefore, the worm-like chain follows a different force law as it approaches its maximum extension. No closed form analytical solution exists to describe this force law, but Marko and Siggia [33] have suggested an approximate expression that captures the correct behavior at large and small extensions:

$$\frac{f\ell_p}{k_BT} = \frac{R}{L_c} + \frac{1}{4(1-R/L_c)^2} - \frac{1}{4}. \tag{2.28}$$

Excluded Volume

The ideal chain model is very useful for explaining many of the most basic phenomenon observed in polymer physics. However, it lacks realism because it neglects interactions between distant monomers along the chain backbone as well as monomer interactions with the solvent. These additional interactions are known as excluded volume effects (EV), and their inclusion in models leads to qualitatively different results for the equilibrium coil size and other quantities of interest. For example, if the interactions between the monomers and solvent molecules are more energetically

favorable than those between monomers and monomers, the coil tends to pull it solvent molecules which leads to swelling of the coil beyond the predicted size of the ideal chain models. This is referred to as "good solvent" behavior. On the other hand, "poor solvent" behavior, where the monomer-solvent interactions are weak, leads to expulsion of solvent molecules from the coil, and the coil size is smaller than the ideal chain prediction. Indeed, if the monomer-monomer interactions are strong enough compared to the monomer-solvent interactions, complete collapse of the coil can occur. However, for the current systems of interest in this work (i.e., DNA in aqueous solutions), only good solvent behavior is relevant, and we restrict our analysis to this regime.

To introduce the effects of EV, we look to the approach of Flory, which provides a simple and elegant scaling theory that paints of a physical picture of the swelling phenomenon and very nearly predicts the correct behavior for polymers in good solvents. Flory attempted to find the free energy of the chain by estimating both the energetic contributions, which tend to swell the coil, and the entropic contributions, which try to limit the size of the coil. Because these two effects act in opposition, they can be balanced against one another to obtain a scaling for the coil size.

The effects of monomer-solvent versus monomer-interactions, as well as the effects of finite monomer size, are all taken into account through a single parameter v, which is the effective excluded volume of a Kuhn monomer. Therefore, the total excluded volume for the chain is $N_{\mathrm{K}}\mathrm{v}$. If the equilibrium coil size of the chain is R, then the pervaded volume of the chain is $\sim R^3$, and the fraction of the pervaded volume represented by the excluded volume of the chain is $\sim N_{\mathrm{K}}\mathrm{v}/R^3$. In a mean field sense, this also represents the probability that a single Kuhn monomer overlaps the excluded volume of another Kuhn monomer. So for N_{K} Kuhn monomers, there are on average $\sim {N_{\mathrm{K}}}^2\mathrm{v}/R^3$ overlaps. Each overlap restricts a degree of freedom of the chain, leading to an energetic penalty on the order of $k_{\mathrm{B}}T$. Therefore, the energetic contribution F_{int} to the free energy due to excluded volume is

$$F_{\mathrm{int}}(R) \sim k_{\mathrm{B}}T\mathrm{v}\frac{{N_{\mathrm{K}}}^2}{R^3}. \tag{2.29}$$

For the entropic contribution F_{ent}, we use that of an ideal chain (see Equation 2.23) stretched to size R:

$$F_{\mathrm{ent}}(R) \sim k_{\mathrm{B}}T\frac{R^2}{N_{\mathrm{K}}{b_{\mathrm{K}}}^2}. \tag{2.30}$$

The total free energy is the sum of these two contributions $F \sim F_{\mathrm{int}} + F_{\mathrm{ent}}$, and the equilibrium size R_0 is determined by finding the minimum of the free energy ($\partial F/\partial R = 0$). This gives the equilibrium coil size for a polymer in a good solvent:

$$R_0 \sim \mathrm{v}^{1/5}{b_{\mathrm{K}}}^{2/5}{N_{\mathrm{K}}}^{3/5}. \tag{2.31}$$

This result, which agrees well with experiments, benefits from the cancellation of a couple errors. First, due to its mean field approximation, Flory theory overestimates the number of exclusions and, therefore, the energetic contribution to the free energy F_{int}. However, it also overestimates the the entropic contribution F_{ent} because it makes use of the ideal chain result. It turns out that both of these overestimates nearly cancel each other out, and Flory theory gives a very good estimate for the good solvent universal scaling exponent ν for the coil size with N_{K}. Flory theory predicts $\nu = 3/5$ while more accurate estimates give a value of $\nu = 0.59$. This is larger than the case of an ideal chain where $\nu = 1/2$, which is indicative of the fact that excluded volume effects lead to a larger coil size.

2.1.2 *Dynamics*

Polymer molecules in solution are constantly fluctuating entities that perpetually change their shape, orientation, and position to due to thermal motion. It is not enough just to study the equilibrium properties of polymers; it is equally important to understand the dynamical processes that govern polymer behavior both at equilibrium and away from it. In reality, a polymer molecule is immersed in a sea of solvent molecules with which it interacts through thermal collisions (assuming we neglect any energetic interactions). This system could theoretically be modeled by solving the equations of motion for each solvent molecule and each segment of the polymer chain; however, this is both intractable and unnecessary.

On the length and time scales of interest to this work, the effect of the solvent molecules is to provide seemingly random, thermal "kicks" to the different segments of the polymer chain, referred to as Brownian motion. Therefore, the solvent molecules are usually replaced by a stochastic force applied to the polymer chain, and the resulting stochastic differential equations (SDEs) of motion for the chain segments is solved. In this case, the molecule is represented by a series of connected beads, similar to the analysis of equilibrium chain in Section 2.1.1. The general Langevin equation for the ith bead position $\mathbf{R}_i$ is given by

$$\frac{\partial \mathbf{R}_i}{\partial t} = \sum_{j=1}^{N_b} \mathbf{H}_{ij} \cdot \left(-\frac{\partial U}{\partial \mathbf{R}_j} + \mathbf{f}_j \right) + \frac{1}{2} k_\mathrm{B} T \sum_{j=1}^{N_b} \frac{\partial}{\partial \mathbf{R}_j} \cdot \mathbf{H}_{ij} \tag{2.32}$$

where N_b is the total number of beads, $\mathbf{H}_{ij}$ is the mobility matrix, U is the total energy of the chain, including any external potential field, and $\mathbf{f}_j$ is the Brownian force on the jth bead. For most polymer dynamics models, the beads are assumed to be connected by Hookean springs with a spring constant equal to

$$H_s = \frac{3 k_\mathrm{B} T}{{b_\mathrm{K}}^2}, \tag{2.33}$$

so that each spring represents a Kuhn segment (see Equation 2.26). This leads to a total energy of

$$U = \frac{H_s}{2} \sum_{i=2}^{N_b} \left(\mathbf{R}_i - \mathbf{R}_{i-1} \right)^2, \tag{2.34}$$

and provides the starting point for our analysis of chain dynamics (for internal beads):

$$\frac{\partial \mathbf{R}_i}{\partial t} = \sum_{j=1}^{N_b} \mathbf{H}_{ij} \cdot \left[H_s \left(\mathbf{R}_{j+1} - 2\mathbf{R}_j + \mathbf{R}_{j-1} \right) + \mathbf{f}_j \right] + \frac{1}{2} k_\mathrm{B} T \sum_{j=1}^{N_b} \frac{\partial}{\partial \mathbf{R}_j} \cdot \mathbf{H}_{ij}. \tag{2.35}$$

Rouse Model

The simplest model for polymer dynamics is the Rouse model. In this case, EV is ignored, and all hydrodynamics interactions (HI) between beads is neglected. Hydrodynamic interactions occurs when the movement of a polymer segment disturbs the surrounding solvent and sets up a decaying velocity field that is felt by nearby segments. When HI is neglected, the molecule is said to be "free-draining," and the movement of one bead does not affect the mobility of another. Therefore,

the mobility tensor for the Rouse model is written as

$$\mathbf{H}_{ij} = \zeta_b{}^{-1}\mathbf{I}\delta_{ij}, \tag{2.36}$$

where ζ_b is the drag coefficient of a single bead and $\mathbf{I}$ is the identity tensor. This leads to the equations of motion for the Rouse model:

$$\zeta_b \frac{d\mathbf{R}_i}{dt} = H_s\left(\mathbf{R}_{i+1} - 2\mathbf{R}_i + \mathbf{R}_{i-1}\right) + \mathbf{f}_i, \tag{2.37}$$

which is a linear system of ordinary stochastic differential equations. The Brownian force, which is Gaussian and must satisfy the fluctuation-dissipation theorem, is defined by the moments

$$\langle \mathbf{f}_i(t) \rangle = \mathbf{0}, \tag{2.38}$$

$$\left\langle f_{i\alpha}(t) f_{j\beta}(t') \right\rangle = 2k_{\mathrm{B}}T\zeta_b\delta_{ij}\delta_{\alpha\beta}\delta(t-t'). \tag{2.39}$$

This system of ordinary differential equations can be transformed into a single partial differential equation. In this case, the discrete index i becomes a continuous variable n that represents the positions along the contour of the chain:

$$\zeta_b \frac{\partial \mathbf{R}_n}{\partial t} = H_s \frac{\partial^2 \mathbf{R}_n}{\partial n^2} + \mathbf{f}_n. \tag{2.40}$$

The stochastic force becomes

$$\langle \mathbf{f}_n(t) \rangle = \mathbf{0}, \tag{2.41}$$

$$\left\langle f_{m\alpha}(t) f_{n\beta}(t') \right\rangle = 2k_{\mathrm{B}}T\zeta_b\delta(n-m)\delta_{\alpha\beta}\delta(t-t'), \tag{2.42}$$

and for the case of zero tension at the ends of the chain, the boundary conditions are

$$\left.\frac{\partial \mathbf{R}_n}{\partial n}\right|_{n=0} = \left.\frac{\partial \mathbf{R}_n}{\partial n}\right|_{n=N_b} = 0. \tag{2.43}$$

A normal mode analysis can be performed for this system by solving the associated eigenvalue problem. Many dynamical quantities of interest can then be determined based upon the time correlations of the various contributing modes. In the case of the of the overall diffusivity of the chain D, the Rouse model predicts

$$D = \frac{k_{\mathrm{B}}T}{N_b\zeta_b} \tag{2.44}$$

This is exactly the result expected for a free-draining chain, where the overall chain drag coefficient ζ should simply be the sum of all the bead drag coefficients (i.e., $\zeta = N_b\zeta_b$). Making use of the Stokes-Einstein relation, this means $D = k_{\mathrm{B}}T/\zeta = k_{\mathrm{B}}T/N_b\zeta_b$, precisely as predicted by Equation 2.44. The longest conformational relaxation time τ_c can also be determined. This is the time scale over which global rearrangement of the chain segments occurs. For the Rouse model,

$$\tau_c = \frac{{N_b}^2\zeta_b{b_{\mathrm{K}}}^2}{3\pi^2 k_{\mathrm{B}}T}. \tag{2.45}$$

Table 2.1: *Summary of the scaling results of Section 2.1.2 for the overall chain diffusivity D and the longest conformational relaxation time τ_c. The predicted scalings with chain length N_b are shown depending upon the physics included.*

	Free-draining $D \sim {N_b}^{-1}$, $\tau_c \sim {N_b}^{1+2\nu}$	**HI** $D \sim {N_b}^{-\nu}$, $\tau_c \sim {N_b}^{3\nu}$
Ideal, $\nu = 1/2$	$D \sim {N_b}^{-1}$, $\tau_c \sim {N_b}^{2}$	$D \sim {N_b}^{-1/2}$, $\tau_c \sim {N_b}^{1.5}$
EV, $\nu = 3/5$	$D \sim {N_b}^{-1}$, $\tau_c \sim {N_b}^{2.2}$	$D \sim {N_b}^{-3/5}$, $\tau_c \sim {N_b}^{1.8}$

The important findings from the Rouse model are, that for a free-draining, ideal chain, $D \sim {N_b}^{-1}$ and $\tau_c \sim {N_b}^{2}$.

Zimm Model

It turns out that the Rouse model does not correctly predict the experimental scalings with chain length for the diffusivity and the relaxation time. This is due to the exclusion of hydrodynamic interactions. Their effect may be included by modifying the mobility tensor to include the Oseen tensor which gives the solvent disturbance due to a point force on the fluid:

$$\mathbf{H}_{ij} = {\zeta_b}^{-1}\mathbf{I}\delta_{ij} + \frac{1}{8\pi\eta_s \left|\mathbf{r}_{ij}\right|}\left(\hat{\mathbf{r}}_{ij}\hat{\mathbf{r}}_{ij} + \mathbf{I}\right)\left(1 - \delta_{ij}\right), \tag{2.46}$$

where $\mathbf{r}_{ij} = \mathbf{R}_i - \mathbf{R}_j$, $\hat{\mathbf{r}}_{ij}$ is the unit vector pointing in the $\mathbf{r}_{ij}$ direction, and η_s is the solvent viscosity. However, the governing Langevin equation (see Equation 2.35) becomes nonlinear using this mobility tensor. This can be overcome by approximating $\mathbf{H}_{ij}$ using its equilibrium preaveraged form:

$$\left\langle \mathbf{H}_{ij} \right\rangle_{\mathrm{eq}} = \frac{\mathbf{I}}{\left(6\pi^3 \left|i - j\right|\right)\eta_s b_{\mathrm{K}}}. \tag{2.47}$$

A normal mode analysis of the resulting linear partial differential equation finds that the scalings for the chain diffusivity and the longest conformational relaxation time are given by

$$D \sim \frac{k_{\mathrm{B}}T}{\eta_s\sqrt{N_{\mathrm{K}}}b_{\mathrm{K}}} \text{ and } \tau_c \sim \frac{\eta_s\left(\sqrt{N_{\mathrm{K}}}b_{\mathrm{K}}\right)^3}{k_{\mathrm{B}}T}. \tag{2.48}$$

2.2 Polymer Stretching

Polymer stretching can be achieved by either direct manipulation or interaction with a flow field. The appeal of direct manipulation, such as optical tweezing, is that the effects of the applied forces are usually obvious and predictable [34]. But while this gives very precise control over the deformation, it is not simple to perform and certainly seems difficult to scale-up. Therefore, flow fields, which are easily imposed and extremely scalable, provide an attractive alternative and have traditionally been used. The difficulty, however, is that their effects on the polymer conformation

are not necessarily obvious.

2.2.1 Direct Manipulation and Tethering

Direct manipulation uses optical tweezers [35] to directly apply forces to DNA. A small bead is attached to an end of a DNA molecule, and then a focused laser beam is used to apply a trapping force on the bead as shown in Fig. 2.1. Bustamante et al. [34] studied the force-extension behavior of DNA using this technique. They attached beads at both ends of a DNA molecule and stretched the polymer by holding one bead stationary in an optical trap and moving the other one with a pipette. Stretching has also been accomplished by only trapping one end of the molecule and placing the tethered DNA in a flow field. The loose end is then pulled or dragged by the field causing the polymer to deform. Optical tweezing has been used to study the relaxation of DNA [36] and the stretching of DNA in a uniform hydrodynamic flow [37]. Blanch et al. [38] verified the theory of hydrodynamic equivalence in a similar way but without the optical trap. Instead, they tethered one end of a DNA molecule to a stationary post in a microfluidic channel and examined the stretching in both hydrodynamic and electric flow fields.

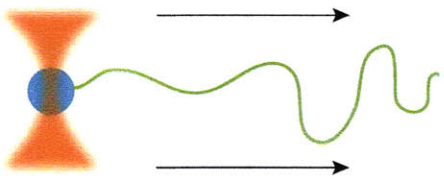

Fig. 2.1: *Depiction of an optical trap. A laser (shown in red) traps a plastic bead (shown in blue) that is attached to the end of a polymer chain (shown in green). The free end of the polymer deforms due to the uniform hydrodynamic flow surrounding it.*

2.2.2 Flow Fields

The effects of homogeneous flow fields have been widely studied and are typically organized into a few broad categories of flow types each with its own characteristic polymer dynamics [39]. Shear flows, for example, are able to moderately stretch polymers, but the fields also have strong rotational components that cause the molecules to "tumble" and retract back into coils [40]. The best homogeneous fields for stretching are extensional flows which have no rotational components but each have axes of extension and compression [39]. When new methods of stretching are considered, they are often compared to the effectiveness of extensional flows. Of particular importance to polymer stretching is the idea of a critical strain rate. This is the strain rate at which the fluid elements are moving apart from each other just fast enough to overcome the entropic forces that keep the molecule coiled. The strength of the flow is usually represented by the dimensionless group *De*

which compares the strain rate to the relaxation time of the chain; it has been found that the critical Deborah number De_c for polymers in extensional flows is about 0.5 [41]. The dynamics of the stretching is also dependent upon the initial configurations of the chains when the field is applied. Some configurations rapidly uncoil while others take a very long time to unravel; therefore, the total strain required to fully extend a polymer is not a single number but a broad distribution based on molecular individualism [41, 24]. It has been shown that molecules can be "preconditioned" for stretching by biasing their configurations away from equilibrium through using a different type of flow field initially [42, 43].

While homogeneous flow fields have received much attention, there have only been a few studies that have observed flows involving non-homogeneous fields where polymer dynamics and deformation were examined [25, 42, 44, 45, 46]. Typically most work has been confined to situations where the flow field can be found analytically, and often the effects of the field have not been fully analyzed. Leal et al. [47] have predicted that polymer stretching even in a locally homogeneous field should be qualitatively different from that in a completely homogeneous case. Even less work has been performed on fields that vary over the length of the polymer [48]. Randall et al. [21] have shown, however, that the idea of accumulated strain at a critical strain rate is still be applicable in non-homogeneous flow fields [21, 49].

2.2.3 Obstacle Arrays

Currently, the most common design for microfluidic DLA devices contains a contraction that sets up a flow field with a strong extensional component to stretch the DNA molecules [2, 22] (see Fig. 1.1). The difficulty with this approach is that molecular individualism prevents the chains from stretching uniformly; indeed, some chains hardly stretch at all [22]. In order to overcome this problem, Randall et al. [22] placed a gel directly before the contraction which forced the molecules to stretch and reptate through the small pores of the matrix. Upon exiting the gel, most of the DNA easily stretched in the contraction due to this "preconditioning" of the configurations. The use of a gel, however, to perform the preconditioning is not desirable due to difficulties assembling the gel in the device and gel degradation. Microlithographically constructed obstacle arrays could circumvent these issues while still providing a preconditioning mechanism. Fabricated arrays also have the advantage of extremely precise control over the obstacle features and placement so that the geometries can be tailored for optimal results.

Obstacle arrays have been highly studied over the past decade, and a great deal has been learned about the effects of DNA collisions. This work began with simulations of gel electrophoresis where the gel fibers were modeled as a regular array of posts [26, 50, 51]. It was found that the dynamics of the DNA movement and deformation were governed by the collisions which often lead to stretching followed by a rope-and-pulley motion and finally collapse of the fully extended chain. This process was termed "geometration" and was experimentally corroborated [27, 4, 52].

In order to simplify the problem, many studies have focused on collisions between a DNA molecule and a single post. Most of the research assumed that the dominant type of impacts, besides glancing blows, were hooking events that subsequently led to the rope-and-pulley motion reported by Deutsch et al. [26]. Therefore, many aspects of hooking were examined and a great deal of theory was developed (some of which is summarized in Table 2.2). But Randall et al. [9] found that several different classes of collisions were statistically important. They observed the classic hooking collisions, which they called U and J collisions, but they also noticed similar

Table 2.2: *A list of some of the single obstacle studies that have been performed. A few of the important findings of each are listed.*

Investigators	Findings
Sevick et al. [6]	Unhooking is faster than tension equilibration in the polymer
Slater et al. [5]	Large variations in impact dynamics even for direct collisions
Sevick et al. [7]	Offset of DNA center of mass from the center of the post greatly affects hooking probability
Ajdari et al. [53]	HI can generally be neglected when considering unhooking
Sevick et al. [8]	Obstacle size is very important in determining whether a hooking or a roll-off event occurs
Randall et al. [21]	Non-homogeneous electric fields around the obstacle are significant in polymer deformation

impacts that they called X collisions which sometimes occurred more often than the U and J cases. In this case, two unraveling arms form just as in the U and J situation, but one of the arms finishes unraveling long before the other arm. Therefore, the rope-and-pulley motion begins before the molecule becomes fully stretched.

There has been much less work involving more than one obstacle. Sevick et al. [54] examined the unhooking dynamics of a chain draped over two posts simultaneously. Other groups have looked at a full array of obstacles [55, 56] which has been shown to be capable of electrophoretically separating long strands of DNA [57]. However, the dynamics of the DNA moving through the arrays have generally been ignored in favor of examining the overall dispersion within the system [55, 56]. These large arrays are periodic, and as a polymer molecule makes its way through the array, a dynamic steady-state behavior develops in a manner analogous to steady shear flows where polymers repeatedly stretch, tumble, and contract [26]. Almost all the work on arrays of posts has been done on very large arrays and has focused on the resulting steady-state behavior of the polymers as they move through the array. The end effects, however, are important. Turner et al. [17] have shown that as a DNA molecule enters a tight array where the post spacing is about the same as the persistence length of the DNA, there is an entropic force that tries to drive the chain out of the array due to the loss of configurational entropy [17, 18]. Randall et al. [22] have also shown that exit effects are important by their observation that as an electrophoresing DNA molecule exits a gel in a microfluidic device, it behaves as a tethered molecule.

2.3 Simulation Methods

Because polymers are large molecules, it is currently impossible to simulate them at the atomisitic level over time scales that are relevant to their dynamics in flow fields. Therefore, polymers are coarse-grained to develop a simple model that smears out the details that have little effect on dynamics over the time scales of interest. The resulting polymer model is then incorporated into a mesoscopic simulation method that somehow coarse-grains the individual solvent molecules as well.

2.3.1 Coarse-graining Models

The most common polymer coarse-graining is the bead-spring model. Due to their extreme size and large variation in chemical composition, polymers are difficult to both understand and simulate.

Despite all of this variability, the behavior of most polymer chains is qualitatively similar because at length scales much larger than the atomistic level, the fine details of chemical structure seem to vanish. At the typical length scales of interest, the important features of polymer chains are their random nature which results in an entropic spring force. This has led to coarse-graining models which represent a polymer as a set of beads that are attached by springs [58] as shown in Fig. 2.2. In these so-called bead-spring models, the springs each represent a certain amount of the contour length of the polymer, and the beads act as discrete positions on the polymer backbone where all the forces that the molecule experiences are applied. The stretch of the springs is governed by a force law which contains the finer details of the polymer being modeled; however, great care must be taken when developing these spring laws as the effects of coarse-graining are not straightforward and are often quite subtle [59]. The various forces that polymers experience and how they are applied, including spring force laws, will be discussed in more detail later (see Sec. 2.3.3).

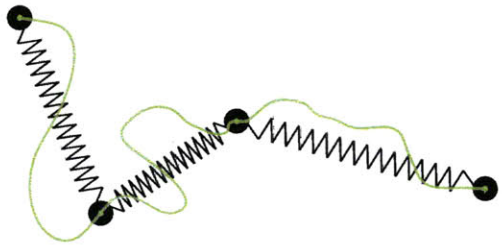

Fig. 2.2: *A representation of the bead-spring model where the springs each represent a certain portion of the polymer contour length.*

Another common coarse-graining is the bead-rod model where the springs in the bead-spring chain are replaced by rigid rods that each represent a Kuhn length [58]. The idea is to model the polymer as an equivalent freely jointed chain (see Sec. 2.3.3). The bead-rod model is often used in situations where current spring force laws do not adequately describe the dynamics of the chain because the bead-rod model is less coarse-grained and contains more fine detail. For example, bead-rod chains are often used in highly confined environments [60, 61].

2.3.2 Brownian Dynamics

Brownian dynamics (BD) is a mesoscopic simulation technique that uses coarse-graining of the solvent molecules in order to remove them from explicitly appearing in the simulation. This simplification is both necessary and possible because polymer sizes are typically orders of magnitude greater than the size of solvent molecules. Removing the solvent molecules from the simulation vastly reduces the computational time and space needed. Instead, their interactions with a polymer chain are incorporated by applying various forces on the beads in the bead-spring model resulting in an equation of motion for each of the N bead positions $\boldsymbol{r}_i$ [62],

$$m_i \frac{d^2 \boldsymbol{r}_i}{dt^2} = \boldsymbol{F}_i^{\mathrm{d}} + \boldsymbol{F}_i^{\mathrm{s}} + \boldsymbol{F}_i^{\mathrm{nh}} + \boldsymbol{F}_i^{\mathrm{B}}. \tag{2.49}$$

One of the most important ways in which solvent molecules interact with a polymer is through thermal randomizing forces caused by collisions which are recreated by applying random forces $\boldsymbol{F}_i^{\mathrm{B}}$ to the beads. The solvent molecules also act as carriers of momentum which is imparted to the polymer chain through the inclusion of a viscous drag force $\boldsymbol{F}_i^{\mathrm{d}}$ providing the chain with "knowledge" of its surroundings. This drag force is taken to be the Stokes drag on a sphere

$$\boldsymbol{F}_i^{\mathrm{d}} = -\zeta \left[\frac{d\boldsymbol{r}_i}{dt} - \boldsymbol{u}(\boldsymbol{r}_i) \right] \tag{2.50}$$

where ζ is the drag coefficient and $\boldsymbol{u}(\boldsymbol{r}_i)$ is the velocity of the solvent surrounding the bead, including any disturbances to the unperturbed flow field [21]. Forces due to any surrounding hydrodynamic velocity field are represented by this drag force. The connectivity of the polymer is taken into account through the spring forces between beads $\boldsymbol{F}_i^{\mathrm{s}}(t)$ allowing beads to "communicate" with each other. All other forces, such as body forces, excluded volume effects, etc., are contained in $\boldsymbol{F}_i^{\mathrm{nh}}$.

Due to the small mass that each bead represents, the inertia of the beads is typically neglected indicating that the sum of all the forces on a bead is nearly zero. This leads to the simplified equation of motion for each bead known as a Langevin equation, [62]

$$\frac{d\boldsymbol{r}_i}{dt} = \boldsymbol{u}(\boldsymbol{r}_i) + \frac{1}{\zeta} \left[\boldsymbol{F}^{\mathrm{s}}\left(\{\boldsymbol{r}_i\}\right) + \boldsymbol{F}^{\mathrm{nh}}\left(\{\boldsymbol{r}_i\}\right) + \boldsymbol{F}_i^{\mathrm{B}}(t) \right]. \tag{2.51}$$

This is a stochastic differential equation where, in order to comply with the fluctuation-dissipation theorem, the Brownian force $\boldsymbol{F}_i^{\mathrm{B}}$ must satisfy the expectations

$$\left\langle \boldsymbol{F}_i^{\mathrm{B}}(t) \right\rangle = \boldsymbol{0} \tag{2.52}$$

$$\left\langle \boldsymbol{F}_i^{\mathrm{B}}(t) \boldsymbol{F}_j^{\mathrm{B}}(t') \right\rangle = 2k_B T \zeta \delta_{ij} \delta(t - t') \boldsymbol{\delta} \tag{2.53}$$

where k_B is Boltzmann's constant and T is temperature [62]. The set of differential equations for all bead in a polymer can then be solved by integrating forward in time.

One difficulty with BD is that when hydrodynamics interactions are included (see Sec. 2.3.3) the computational time required for a simulation scales badly with chain length ($\sim N^3$/time step). Other mesoscopic simulation techniques that avoid this problem include dissipative particle dynamics (DPD) [63, 64] and the lattice Boltzmann method [65, 66], but these methods are not as well-understood as BD.

2.3.3 Included Physics

Force Law

Each spring in the bead-spring model is a coarse-grained representation of a polymer chain segment. The important characteristic captured by the springs is the entropic elasticity that results from the enormous number of configurations that the segment can adopt [67]. The spring law used in the bead-spring model describes the entropic tension force in the chain segment when its ends are separated by a given distance. Because polymer properties like bending rigidity and bond angles can affect the overall polymer elasticity, different models have been developed to describe the resulting spring force laws. An important example is the freely jointed chain where the molecule is represented as a set of rigid rods of fixed length connected together at random angles. This

model has the benefit that it is simple enough to solve for its spring force exactly using statistical mechanics. Therefore, many polymers are modeled as equivalent freely jointed chains that have the same contour length L and equilibrium mean-squared end-to-end distance $\langle \boldsymbol{R}^2 \rangle_0$ [68].

DNA is not well-described by the freely jointed chain because it is a very rigid molecule that does not easily bend. Instead, the worm-like chain model is used. Recently, Underhill and Doyle [69] have developed a modified Marko-Siggia force law that better predicts the behavior of the chain for a large range of the coarse-graining parameter $\upsilon = \ell_s/\ell_p$. This result was based on their study of the effect that coarse-graining has on the force-extension behavior of a bead-spring model [59, 70].

Generally, spring laws assume that the polymer is in the bulk or in a bulk-like state where they can sample their full, uninhibited configuration space. In highly confined environments, however, this assumption is invalid, and the configurations available to the chains are restricted. There have been few attempts to address this issue, and those that have tried to develop new models and spring forces have had limited success [71].

Hydrodynamic Interactions and Electrophoresis

Hydrodynamic interactions (HI) play an important role in polymer dynamics. Inclusion of HI into models can lead to different scalings for physical parameters such as viscosity and relaxation time as seen in the differences between the free-draining Rouse model and the Zimm model which includes equilibrium-averaged HI [58]. In some situations, neglecting HI can lead to behavior that is even qualitatively incorrect [72, 73, 74, 75].

HI occur when polymer movements disturb the solvent flow around them. In essence, any movements of the polymer chain that are not in perfect unison with the surrounding velocity field will perturb the field and set up a decaying velocity disturbance. When a polymer is coarse-grained into a bead-spring chain, each bead disturbs the field and affects all the other beads. These disturbances are often modeled as Stokeslets, or point forces, and are incorporated into BD through the Oseen-Burgers tensor $\boldsymbol{H}^0(\boldsymbol{r})$ which decays as $1/r$ [39]

$$\left[\boldsymbol{H}^0(\boldsymbol{r})\right]_{ij} = \frac{1}{8\pi\eta r}\left(\delta_{ij} + \frac{r_i r_j}{r^2}\right) \tag{2.54}$$

where $\boldsymbol{r}$ is taken from the origin of the disturbance, η is the solvent viscosity, and δ_{ij} is the Kronecker delta. For neutral polymers, all forces exerted on a bead, such as Brownian forces, spring forces, and excluded volume forces, lead to HI. When the velocity term $\boldsymbol{u}(\boldsymbol{r}_i)$ in Eq. 2.51 is expanded to explicitly include HI, the Langevin equation becomes

$$\begin{aligned} \tfrac{d\boldsymbol{r}_i}{dt} &= \boldsymbol{u}^\infty(\boldsymbol{r}_i) + \tfrac{1}{\zeta}\left[\boldsymbol{F}^{\mathrm{s}}(\{\boldsymbol{r}_i\}) + \boldsymbol{F}^{\mathrm{EV}}(\{\boldsymbol{r}_i\}) + \boldsymbol{F}_i^{\mathrm{B}}(t)\right] \\ &+ \sum_{i\neq j} \boldsymbol{H}^0(\boldsymbol{r}_i - \boldsymbol{r}_j) \cdot \left[\boldsymbol{F}^{\mathrm{s}}(\{\boldsymbol{r}_j\}) + \boldsymbol{F}^{\mathrm{EV}}(\{\boldsymbol{r}_j\}) + \boldsymbol{F}_j^{\mathrm{B}}(t)\right]. \end{aligned} \tag{2.55}$$

where $\boldsymbol{u}^\infty(\boldsymbol{r}_i)$ is the unperturbed velocity of the solvent.

The physics of polyelectrolytes undergoing electrophoresis is much more complicated than the case of neutral polymers. When an electric field is applied there is no bulk movement of the solvent due to its average electroneutrality, but the charged polymer does feel a net force and moves through the fluid. This perturbs the quiescent bulk fluid just as in the case of the neutral

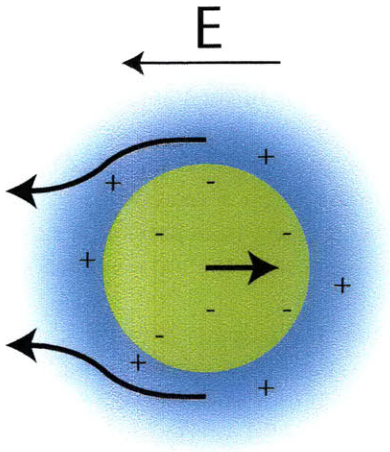

Fig. 2.3: *The effect of an electric field on a charged particle (shown in green) and the counterion cloud that it attracts (shown in blue).*

polymer. The differences appear because the charged backbone attracts a cloud of oppositely charged counterions that surrounds it over the length scale of the Debye length as shown in Fig. 2.3. Therefore, the solvent near the polymer is not electroneutral and also reacts to the applied field moving in the opposite direction as the polyelectrolyte. The movement of this counterion cloud has two effects. One is that it increases the drag on the chain which leads to an electrophoretic mobility μ, the electrical equivalent to the hydrodynamic drag coefficient. The second effect is that it also perturbs the bulk fluid by setting up its own small velocity field opposing the disturbances of the polymer. This latter effect leads to the conclusion that the HI tensor due to electrical forces $\boldsymbol{H}^{\mathrm{EL}}$ is not equivalent to the one created by non-electrical forces $\boldsymbol{H}^{0}$. When using BD to simulate electrophoresis Eq. 2.55 becomes

$$\frac{d\boldsymbol{r}_i}{dt} = \boldsymbol{u}^{\infty}(\boldsymbol{r}_i) + \mu \boldsymbol{E}(\boldsymbol{r}_i) + e\lambda \sum_{i \neq j} \boldsymbol{H}^{\mathrm{EL}}(\boldsymbol{r}_i - \boldsymbol{r}_j) \cdot \boldsymbol{E}(\boldsymbol{r}_j)$$
$$+ \frac{1}{\zeta}\left[\boldsymbol{F}^{\mathrm{s}}(\{\boldsymbol{r}_i\}) + \boldsymbol{F}^{\mathrm{EV}}(\{\boldsymbol{r}_i\}) + \boldsymbol{F}_i^{\mathrm{B}}(t)\right] + \sum_{i \neq j} \boldsymbol{H}^{0}(\boldsymbol{r}_i - \boldsymbol{r}_j) \cdot \left[\boldsymbol{F}^{\mathrm{s}}(\{\boldsymbol{r}_j\}) + \boldsymbol{F}^{\mathrm{EV}}(\{\boldsymbol{r}_j\}) + \boldsymbol{F}_j^{\mathrm{B}}(t)\right] \quad (2.56)$$

where e is the fundamental charge and λ is the charge per bead [76].

The increased drag on the chain causes the electrophoretic mobility μ to be dependent on the size of the counterion cloud which is determined by the ionic strength of the solution. Surprisingly, at high salt concentrations the electrophoretic mobility becomes independent of the length or the conformation of the polymer [77]. Also, the counterion movements counteract those of the chain almost exactly so that the velocity disturbances are screened over the length scale of the counterion cloud which is the Debye length. Therefore, if the ionic strength of the solution is high so that the Debye length is small, the electric field does not cause HI amongst the polymer segments, and

$\boldsymbol{H}^{\mathrm{EL}} \approx \mathbf{0}$ so eq. 2.56 becomes

$$\begin{aligned}\frac{d\boldsymbol{r}_i}{dt} &= \boldsymbol{u}^{\infty}(\boldsymbol{r}_i) + \mu \boldsymbol{E}(\boldsymbol{r}_i) + \tfrac{1}{\zeta}\left[\boldsymbol{F}^{\mathrm{s}}(\{\boldsymbol{r}_i\}) + \boldsymbol{F}^{\mathrm{EV}}(\{\boldsymbol{r}_i\}) + \boldsymbol{F}_i^{\mathrm{B}}(t)\right] \\ &\quad + \sum_{i \neq j} \boldsymbol{H}^0(\boldsymbol{r}_i - \boldsymbol{r}_j) \cdot \left[\boldsymbol{F}^{\mathrm{s}}(\{\boldsymbol{r}_j\}) + \boldsymbol{F}^{\mathrm{EV}}(\{\boldsymbol{r}_j\}) + \boldsymbol{F}_j^{\mathrm{B}}(t)\right]. \end{aligned} \tag{2.57}$$

Eq. 2.57 shows that in high salt solutions, electric fields and hydrodynamic fields act in the same manner on polymer chains. This principle is known as hydrodynamic equivalence [78, 79, 23, 76], and although there have been some theoretical challenges against it [80], experimental evidence seems to corroborate the model's validity [30, 38].

Excluded Volume Effects

Excluded volume interactions describe the forces that prevent a polymer from overlapping onto itself, and therefore, they tend to be repulsive forces between segments of the chain. They also help account for polymer-solvent interactions which cause expansion of the chains for good solvents. Often such forces can be modeled as the result of a potential field such that the polymer pays an energetic penalty for adopting a configuration that is too dense. The use of a Lennard-Jones potential might be appropriate, for example.

The difficulty for polymer simulations using a Lennard-Jones potential is that the steepness of the potential necessitates the use of small time steps which vastly increases the computational time. Polymer models, however, are typically coarse-grained to neglect the fine details that occur at small length scales which means a steep potential is not necessary. Instead, a softer potential that always remains bounded allows for much larger time steps and provides the correct physics at large length scales [81]. An exponentially decaying potential accomplishes this goal, and for this project, the potential developed by Jendrejack et al. [82] will be used

$$U_{ij}^{\mathrm{EV}} = \frac{1}{2} v^{EV} k_B T N_{K,s}^2 \left(\frac{3}{4\pi R_s^2}\right) \exp\left(\frac{-3r_{ij}^2}{4R_s^2}\right) \tag{2.58}$$

where U_{ij}^{EV} is the excluded volume between bead i and bead j, v is defined as the parameter for excluded volume, $N_{K,s}$ denotes the number of Kuhn lengths per spring, R_s is the equilibrium end-to-end distance of each spring, and r_{ij} is the distance between bead i and bead j.

Polyelectrolytes also have an additional excluded volume effect due to electrostatic repulsions between charged chain segments that cause additional conformational swelling. These forces, however, are exponentially screened on length scales larger than the Debye length. Therefore, in solutions of high ionic strength where the Debye length is small, intrachain electrostatic repulsions can be ignored [83].

CHAPTER 3

Post Array for Conformational Preconditioning in a Stretching Device

One of the great obstacles in implementing DLA is overcoming molecular individualism in order to obtain a population of uniformly stretched molecules for analysis. This is particularly relevant in strain-limited devices. One approach to tackling this challenge is to use electrophoretic collisions with an array of posts to "preconfigure" DNA molecules for later stretching. This technique has been studied experimentally and was shown to modestly increase the final stretch of DNA molecules that are subsequently exposed to an extensional field for a finite period. In this chapter, we attempt to replicate the experimental results using our BD-FEM simulation technique. We compare our results to the experiments and note where agreement between the two is seen. We also hypothesize that nonlinear electrokinetic effects are responsible for certain quantitative and qualitative differences.

3.1 Overview

Recently our group has reported experiments using an obstacle array to precondition the conformations of DNA molecules to facilitate their stretch in a microcontraction. Based upon previous successes simulating electrophoretic stretching in microcontractions without obstacles, we use our simulation model to study the deformation of DNA chains in a microcontraction preceded by an array of cylindrical obstacles. We compare our data to the experimental results and find good qualitative, and even quantitative, agreement concerning the behavior of the chains in the array; however, the simulations over predict the mean stretch of the chains as they leave the contraction. We examine the amount of stretch gained between leaving the array and reaching the end of the contraction and speculate that the differences seen are caused by non-linear electrokinetic effects that become important in the contraction due to a combination of field gradients and high field strengths.

3.2 Introduction

Biological studies have long relied on the genetic information encoded within DNA molecules. Traditionally, this information is extracted using sequencing techniques, such as gel electrophoresis, that provide single base-pair resolution. [3] While often extraordinarily powerful for molecular biological studies, genetic information at this level of detail is unnecessary for many applications. An often used alternative is DNA mapping which provides lower-resolution genomic information. But the state-of-the-art mapping scheme still requires multiple sets of restriction enzymes and numerous separations by gel electrophoresis. [2] Such techniques are time-consuming and expensive, and these drawbacks have spurred interest in mapping technologies that are not based on gel separations.

One such method is direct linear analysis (DLA) [2, 84] which involves measuring the physical distance between specific sequences along the DNA backbone. This measurement gives a simple and direct physical map of the molecule without the use of restriction enzymes or separation techniques. [85, 2, 84] In DLA, the strands are tagged with sequence-specific fluorescent probes, stretched to their full contour length, and passed by an optical sensor that measures the distance between the probes. The main obstacle in implementing DLA is that the DNA strands, which at equilibrium are entropically coiled, [86] must be fully stretched in order for the measured distance between probes to have a physically relevant meaning.

Many ways have been developed to stretch DNA. Some involve changing the equilibrium conformation from a coil to a more elongated structure by confining DNA. [87, 88] Others have attached beads to the ends of DNA and applied forces directly to the molecule using magnetic [89, 90] or optical traps. [37, 91] Collisions with microfabricated obstacles have also been shown to linearize DNA. [4, 92, 93] But a very practical method for simple, inexpensive, high-throughput devices is using field gradients to deform the molecules. [41, 94]

In DLA devices, the molecules are typically stretched by field gradients in microcontractions. [2, 84, 95, 22, 96, 97] However, in these strain-limited devices, molecular individualism [24] leads to a large population of molecules that do not reach full extension. Recent studies have shown that the effects of molecular individualism can be mitigated by "preconfiguring" the initial conformation of a molecule before it is stretched. [43, 22, 97] Several different methods to preconfigure molecules have been shown to increase the uniformity of stretch, including pre-shearing [43] and passing through a gel matrix. [22] A promising technique is placing a microfabricated obstacle array just

before the contraction to induce molecular collisions with the obstacles [85, 97] (see Figure 3.1A). The collision of DNA with a post often leads to hooking events that change the conformation of the molecules thereby reducing the proportion of slowly-stretching conformations. The collision of a DNA molecule with a single post is a well-studied problem both experimentally [52, 21, 9] and numerically. [5, 8, 10] Several qualitatively different types of hooks have been identified, [9] and their stretching and unhooking dynamics have been investigated. [9, 10] The effect of large arrays of posts has been considered as well, with studies focussed on the start-up behavior of the molecules as they enter the array [93] and their subsequent steady-state behavior. [55, 98, 99] Placing a post array just before the contraction to preconfigure the molecules is also advantageous because the resulting device is simple to fabricate, reusable, and easily scaled.

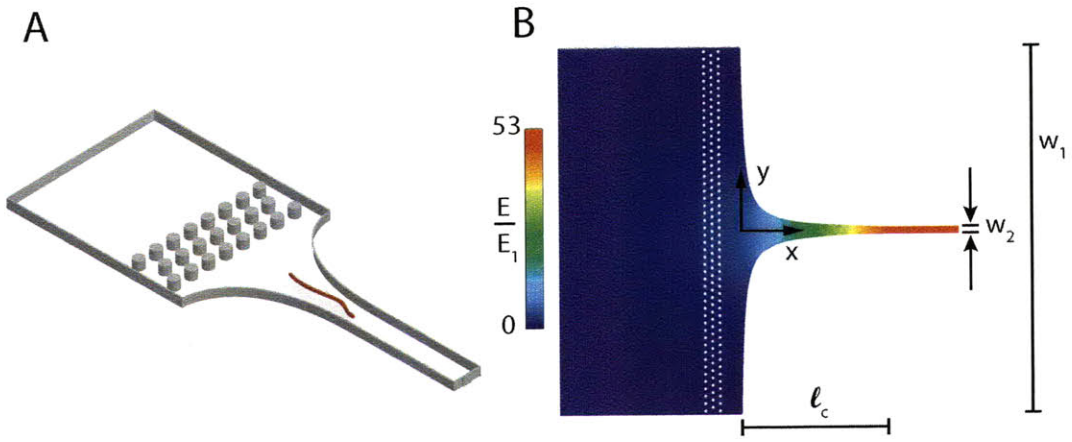

Fig. 3.1: *(A) A cartoon schematic of the general composition of the stretching device (not drawn to scale). The red line represents a strand of DNA stretching as it moves through the contraction. (B) The FEM solution for the magnitude of the electric field normalized by the value of the electric field at the channel inlet (E_1).*

Previously, Kim and Doyle [100] developed a simulation method to study DNA electrophoresis in complex device geometries with non-homogeneous electric fields. They have shown that this model can accurately predict experimental results, even at a quantitative level, for the cases of DNA stretching in microcontractions without posts [96] and the collision of a DNA molecule with a single post in a uniform field. [10] The previous success of the model leads us to consider whether or not it will be useful in studying the effects of placing an obstacle array in front of a microcontraction.

The objectives of this study are to use the numerical model of Kim and Doyle [100] to predict the stretching behavior of DNA molecules in a microdevice composed of a hyperbolic contraction preceded by a post array. These predictions will then be compared to the experimental results of Balducci and Doyle, [97] establishing when the model performs well and when it does not. Finally, in cases where the numerical results are not accurate, reasons for the poor performance will be hypothesized.

3.3 Background

3.3.1 Polymer Deformation in Field Gradients

Electric fields are useful for stretching DNA in microfluidic devices because locally they are purely extensional with no rotational component. [49] This is important because fields with a rotational component, such as shear flows, can lead to periodic behavior where the molecule stretches, collapses, and stretches again. [101, 40] Practically, this reduces the effectiveness of the stretching device, and theoretically, it complicates the analysis of the molecular behavior.

Extensional fields cause stretching when the field gradients deform the molecule faster than it can rearrange itself. [86] The time scale for this molecular rearrangement is the longest relaxation time τ. When the relaxation time is balanced against the characteristic strain rate $\dot{\varepsilon}$ of the field, the result is the Deborah number, $\mathrm{De} = \dot{\varepsilon}\tau$, which is the governing dimensionless parameter for molecular deformation. It has been shown theoretically, [102] and confirmed experimentally, [41, 103] that strong stretching occurs around $\mathrm{De} = 0.5$.

A crude, but effective, model to describe DNA stretching in a homogeneous extensional field can be built using a simple dumbbell. By balancing the drag forces against the wormlike chain spring force [33] and neglecting Brownian motion and any other forces, the dynamic equation for the stretch can be expressed as:

$$\frac{d}{d\varepsilon}\left(\frac{X}{L}\right) = \frac{X}{L} - \frac{1}{3\mathrm{De}}\left[\frac{1}{4\left(1 - X/L\right)^2} - \frac{1}{4} + \frac{X}{L}\right], \tag{3.1}$$

where X is the extension of the molecule, L is the contour length, and ε is the applied strain. This model is particularly useful for predicting the final stretch of a DNA molecule after it has reached steady state, i.e., after an infinite amount of strain has been applied.

One of the greatest difficulties in stretching molecules in an extensional field is overcoming molecular individualism. [24] This phenomenon was first observed in early fluorescent microscopy work on DNA [41, 103] and refers to the fact that the initial conformation of a molecule greatly affects its rate of stretching. This often leads to a broad distribution of molecular extensions in stretching devices because each molecule has reached a different stage of deformation. Large amounts of strain ($\approx$ 10 units) [104] are typically needed to uniformly stretch a population of molecules initially in their equilibrium state. This amount of strain is difficult to apply in most devices unless a field with a stagnation point is employed; [41, 103, 105, 106] however, stagnation points typically cannot be used for high-throughput devices.

3.3.2 Model Assumptions

We briefly consider the theory of DNA electrophoresis which underlies the assumptions of the numerical model. First, the electric field in the device can be determined by solving Laplace's equation because the buffer solution is assumed to be everywhere electroneutral. This assumption is valid because the Debye length κ^{-1} of the solution is typically $O(\mathrm{nm})$ which is much smaller than any other length scale in the problem. Additionally, we neglect any local disturbances of the electric field due to the charged phosphate backbone of DNA because, again, κ^{-1} is smaller than the molecule's persistence length, $A_p = 0.053$ μm, [107] the smallest pertinent length scale of the polymer. This allows us to assume that DNA behaves as a neutral polymer without intramolecular

electrostatic interactions. [108] We also assume the applied electric fields are weak and that we can neglect any non-linear electrokinetic phenomena (although we will later question this assumption).

We invoke the theory of electro-hydrodynamic equivalence [76, 38] which states that in the case of small Debye lengths, DNA dynamics in an electric field $\boldsymbol{E}$ can be treated the same as if the electric field were replaced with a hydrodynamic flow field equal to $\mu\boldsymbol{E}$ where μ is the electrophoretic mobility. This is due to the fact that flow disturbances in the fluid caused by the electrophoretic movement of DNA segments are screened over κ^{-1} due to the opposite movement of the surrounding counterion cloud. [3] Finally, we neglect all other forms of hydrodynamic interactions (HI) as the bulk radius of gyration of T4-DNA which was studied here ($R_g = 1.4$ μm) is comparable to the channel height $h = 2$ μm. [109]

3.3.3 Device Geometry

The device we simulated is identical to that used by Balducci and Doyle [97] and is shown in Figure 3.1B. It consists of two straight channels of different widths connected by a hyperbolic contraction. The wide inlet channel has a width of $w_1 = 200$ μm, and the outlet channel has a width of $w_2 = 3.8$ μm. The shape of the hyperbolic contraction was chosen to create a uniform strain rate within the contraction [95, 96] and has a length of $\ell_c = 80$ μm. In front of the contraction are three rows of posts with each post having a 1 μm radius. The posts are spaced 4 μm center-to-center within each row, and the distance between rows is also 4 μm center-to-center. The center of the first (most upstream) row of posts is located 20 μm in front of the contraction at $x = -20$ μm with the subsequent rows located at $x = -16$ μm and $x = -12$ μm. Finally, the corners of the device were rounded with a 1 μm radius.

The electrophoretic strain rate $\dot{\varepsilon}$ is nearly constant in much of the contraction, [22, 96] and the nominal strain accumulated by a molecule moving down the centerline of the device is $\varepsilon \approx \ln(w_1/w_2) = 4$. The electric field gradient in the contraction can be approximated using the scaling $\nabla E \approx (E_2 - E_1)/\ell_c = [E_1(w_1/w_2 - 1)]/\ell_c$ where E_1 and E_2 are the electric field strengths at the inlet and the outlet of the channel, respectively. This leads to the form of the Deborah number within the contraction:

$$\mathrm{De} = \frac{\mu E_1 \left(w_1/w_2 - 1\right)}{\ell_c}\tau. \tag{3.2}$$

Additional Deborah numbers can also be defined just before the post array and within the array, [97] but we do not consider them here. Finally, the kinematic history is not the same for each streamline. [96] Molecules that enter the contraction from the center of the channel deform differently than those that enter from the edges of the channel. In order to mitigate this effect, we adopted the method used by Balducci and Doyle [97] and only considered molecules whose centers of mass were within 45 μm of the centerline when they entered the post array.

3.4 Simulations

We used a simulation method for DNA electrophoresis in arbitrary geometries that was developed by Kim and Doyle [100]. The method uses Brownian dynamics (BD) to model the behavior of a DNA molecule electrophoresing in an electric field. In order to solve for the electric field in complicated geometries, the finite element method (FEM) is employed. A difficulty that Kim and Doyle [100] addressed is how to find the electric field at an arbitrary point in the solution domain

given that the finite element mesh is unstructured. They developed an efficient way to overcome this problem with the so called 'target-induced searching algorithm'. A brief description of the numerical model is presented here.

3.4.1 Brownian Dynamics

DNA molecules are modeled as chains of N_b beads connected by $N_s = (N_b - 1)$ springs. The equation of motion for the position $\boldsymbol{r}_i$ of the ith bead is:

$$\frac{d\boldsymbol{r}_i}{dt} = \mu^b \boldsymbol{E}(\boldsymbol{r}_i) + \frac{1}{\zeta^b}\left[\boldsymbol{F}_i^B(t) + \boldsymbol{F}_i^S(t) + \boldsymbol{F}_i^{EV}(t) + \boldsymbol{F}_i^{EV,wall}(t)\right], \tag{3.3}$$

where μ^b is the electrophoretic mobility of a bead, ζ^b is the bead drag coefficient, $\boldsymbol{F}_i^B$ is the Brownian force, $\boldsymbol{F}_i^S$ is the total spring force felt by the bead, $\boldsymbol{F}_i^{EV}$ is the intrachain excluded volume force due to nearby beads, and $\boldsymbol{F}_i^{EV,wall}$ represents the interaction of the bead with the wall of the device.

We non-dimensionalize the variables as follows:

$$\hat{\boldsymbol{r}} \equiv \frac{\boldsymbol{r}}{l_s}, \hat{t} \equiv \frac{t}{\zeta^b l_s^2/k_B T}, \hat{\boldsymbol{E}} \equiv \frac{\boldsymbol{E}}{E_1}, \tag{3.4}$$

where $\boldsymbol{r}$ is position, l_s is the maximum extension of a single spring ($l_s \equiv L/N_s$), t is time, k_B is Boltzmann's constant, and T is the absolute temperature. We non-dimensionalize the forces $\boldsymbol{F}$ as follows:

$$\hat{\boldsymbol{F}}(\hat{\boldsymbol{r}}) \equiv \frac{\boldsymbol{F}}{k_B T/l_s}. \tag{3.5}$$

This leads to the non-dimensional form of eq. (3.3):

$$\frac{d\hat{\boldsymbol{r}}_i}{d\hat{t}} = \mathrm{Pe}^b \hat{\boldsymbol{E}}(\hat{\boldsymbol{r}}_i) + \hat{\boldsymbol{F}}_i^B + \hat{\boldsymbol{F}}_i^S + \hat{\boldsymbol{F}}_i^{EV} + \hat{\boldsymbol{F}}_i^{EV,wall}, \tag{3.6}$$

where Pe^b is the bead Peclet number ($\mathrm{Pe}^b \equiv \mu^b E_1 l_s/D^b$) given that the bead diffusivity $D^b = k_B T/\zeta^b$. The non-dimensional Brownian force is given by:

$$\hat{\boldsymbol{F}}_i^B = \sqrt{\frac{24}{\Delta\hat{t}}}(\boldsymbol{r}_n)_i, \tag{3.7}$$

where $\Delta\hat{t}$ is the dimensionless time step and $(\boldsymbol{r}_n)_i$ are uniform random numbers such that each component $(\boldsymbol{r}_n)_i^j \in [-1/2, 1/2]$, where j denotes the coordinate x, y, or z. The net non-dimensional spring force on the ith bead is:

$$\hat{\boldsymbol{F}}_i^S = \begin{cases} \hat{\boldsymbol{f}}_{i,2}^s, & i = 1, \\ \hat{\boldsymbol{f}}_{i,i+1}^s + \hat{\boldsymbol{f}}_{i,i-1}^s, & 1 < i < N_b, \\ \hat{\boldsymbol{f}}_{i,N_b-1}^s, & i = N_b, \end{cases} \tag{3.8}$$

where the spring force $\hat{\boldsymbol{f}}^{\mathrm{s}}_{i,j}$ is given by a modified Marko-Siggia spring force law: [33, 59]

$$\hat{\boldsymbol{f}}^{\mathrm{s}}_{i,j} = \frac{\upsilon}{\lambda}\left[\hat{r}_{ji} - \frac{1}{4} + \frac{1}{4\left(1-\hat{r}_{ji}\right)^2}\right]\frac{\hat{\boldsymbol{r}}_j - \hat{\boldsymbol{r}}_i}{\hat{r}_{ji}}, \tag{3.9}$$

where λ is the ratio of the effective persistence length to the true persistence length ($\lambda \equiv A_{\mathrm{eff}}/A_{\mathrm{p}}$), υ is the number of true persistence lengths represented by each spring ($\upsilon \equiv l_{\mathrm{s}}/A_{\mathrm{p}}$), and $\hat{r}_{ji}$ represents the distance between $\hat{\boldsymbol{r}}_j$ and $\hat{\boldsymbol{r}}_i$. The intrachain excluded volume force $\hat{\boldsymbol{F}}^{\mathrm{EV}}_i$ is modeled with the soft potential used by Jendrejack et al.: [82]

$$\hat{\boldsymbol{F}}^{\mathrm{EV}}_i = -\sum_{j=1(j\neq i)}^{N_{\mathrm{b}}} \frac{9}{2}\hat{\nu}^{\mathrm{ev,p}}\left(\frac{3}{4\sqrt{\pi}}\right)^3 \upsilon^{9/2}\exp\left[-\frac{9}{4}\upsilon\hat{r}^2_{ij}\right]\hat{\boldsymbol{r}}_{ji}, \tag{3.10}$$

where $\hat{\nu}^{\mathrm{ev,p}} \equiv \nu^{\mathrm{ev,p}}/l^3_{\mathrm{s}}$ is the dimensionless form of the excluded volume parameter $\nu^{\mathrm{ev,p}}$.

The interactions between a bead and the walls represented by $\hat{\boldsymbol{F}}^{\mathrm{EV,wall}}_i$ are resolved using a modified Heyes-Melrose algorithm. [110, 100] Whenever a bead moves outside the domain during a time step, it is moved to the nearest point on the domain boundary before commencing the next time step:

$$\Delta\hat{\boldsymbol{r}}^{\mathrm{HM}}_i = \Delta\boldsymbol{p}_i H\left(\Delta p_i\right), \tag{3.11}$$

where $\Delta\hat{\boldsymbol{r}}^{\mathrm{HM}}_i$ is the displacement vector due to the Heyes-Melrose algorithm, $\Delta\boldsymbol{p}_i$ is the vector pointing from the bead outside the domain to the nearest boundary point, and the Heaviside step function $H\left(\Delta p_i\right)$ restricts the application of the algorithm to only the beads that have penetrated the domain boundaries.

3.4.2 Determination of Electric Field

In order to determine the electric field in the device, we use Laplace's equation for the electric potential ϕ within the channel as previously discussed:

$$\nabla^2\phi = 0. \tag{3.12}$$

We assume that the PDMS channel walls are insulating and that the electric fields at the device inlet and outlet are uniform. This leads to the boundary conditions:

$$\phi|_{\mathrm{inlet}} = \phi_1, \quad \phi|_{\mathrm{outlet}} = \phi_2, \quad \text{and} \quad \boldsymbol{n}\cdot\boldsymbol{\nabla}\phi|_{\mathrm{walls}} = 0, \tag{3.13}$$

where ϕ_1 and ϕ_2 are the imposed electric potentials at the inlet and the outlet of the device, respectively, and $\boldsymbol{n}$ is the unit normal to the walls.

Eqs. 3.12 and 3.13 are solved using Galerkin FEM where ϕ is interpolated using a 6-node P^0_2 shape function. The electric field $\boldsymbol{E}$ is found by applying FEM again to the relation $\boldsymbol{E} = -\boldsymbol{\nabla}\phi$ and using a 3-node P^0_1 shape function to interpolate $\boldsymbol{E}$. After obtaining $\boldsymbol{E}$, its nodal values are saved. During the simulations, whenever the value of $\boldsymbol{E}$ is needed at a given point, the target-induced searching algorithm is called to find the element in which the point is located. The nodal values for $\boldsymbol{E}$ in that element are then retrieved, and the value of $\boldsymbol{E}$ at the specified point is interpolated.

3.4.3 Parameters

In this study, T4-DNA was modeled in the same manner as Kim and Doyle [100] in their simulations of DNA collisions with a single post. They assumed a stained contour length of $L = 71.4$ μm and used $N_b = 128$ beads such that $\upsilon = 10.61$. The corresponding λ was 1.89, and an excluded volume parameter $\nu^{ev,p}$ of 0.0004 μm^3 was found to accurately reproduce the radius of gyration of λ-DNA. At this discretization, along with sufficiently small time steps, the aphysical situation where a chain can move "through" a post is precluded. We found the simulated non-dimensional relaxation time of the 128-bead chain to be $\hat{\tau} = 60.1$ in a 2 μm tall channel.

Due to the low field strengths in the inlet of the channel, it takes a very long time to simulate the movement of a chain from the inlet to the beginning of the contraction. In order to decrease the simulation time, point particles possessing the same diffusivity as the 128-bead chains were placed at $x/\ell_c = -2$ and were distributed randomly across the width of the channel with a uniform distribution. The movement of the particles toward the contraction was then simulated until the local dimensionless strain rate $\hat{\dot{\varepsilon}} = l_s^2\dot{\varepsilon}/D_b$ along the centerline reached $\hat{\dot{\varepsilon}} = 0.1/\hat{\tau}$ (but no farther than $x = -30$ μm for the low De cases). At this point, equilibrated chains were placed with their center of masses located at the positions of the particles. The electrophoresis of the chains was then simulated until the most downstream part of the chains reached $x = 250$ μm. The time step scheme was as follows: $\Delta\hat{t} = 0.005$ for $x < -24$ μm at which point it switched to:

$$\Delta\hat{t} = \begin{cases} 0.005, & \mathrm{De} < 3, \\ 0.005\left(\frac{3}{\mathrm{De}}\right), & \mathrm{De} \geq 3. \end{cases} \tag{3.14}$$

For each De considered, 300 chains were simulated although only those within 45 μm of the centerline when they entered the post array were used in this study as discussed earlier.

3.5 Results

The major global observable in the study was the average extension of the molecules as they reached the end of the contraction. In our simulations, the extension of a chain X_{ex} is defined as the distance between the most upstream and downstream beads of the chain, and the extension at the end of the contraction $X_{ex,c}$ was determined when the most downstream part of the chain first passed the end of the contraction. Figure 3.2 compares results from experiments and simulations for $X_{ex,c}$. It is clear from Figure 3.2A that the simulation model does an excellent job of predicting the mean stretch of the molecules in an open channel as was previously shown by Kim and Doyle. [100] But when posts are introduced in front of the contraction, the simulations consistently over predict the average extension by 10-15% as shown in Figure 3.2B. Nonetheless, the results are in qualitative agreement with the experimental trend.

In order to explore why the performance of the simulation model changes so abruptly when posts are added, we have attempted to isolate and analyze the behavior of the chains in each component of the device, i.e., the post array and the contraction. Although this is not strictly possible because the effects of each are certainly coupled, it still provides clues as to why the simulations and experiments differ. In particular, we are interested in whether the differences between the two are simply due to quantitative inaccuracies within the numerical model or due to the failure of the model to predict qualitative features of the experiments.

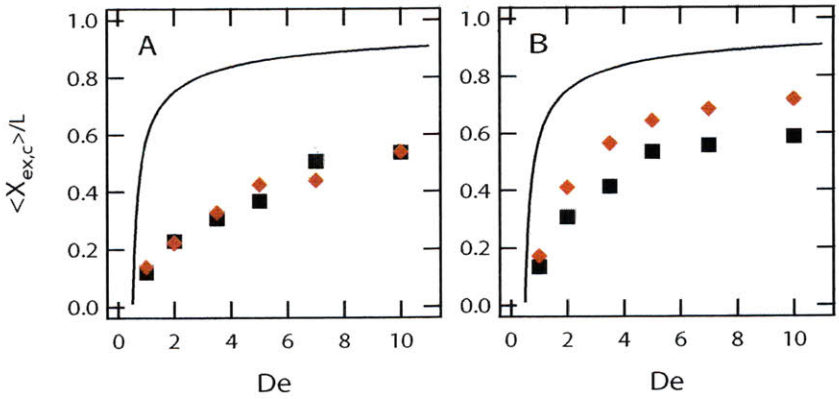

Fig. 3.2: *Ensemble-averaged relative stretch of the chains as they reach the end of the contraction vs De (A) in an open channel and (B) in a channel with posts. The black squares are the experimental data, and the red diamonds are the simulation data. The line represents the theoretical infinite-strain stretch as predicted by the simple dumbbell model given in eq. 3.1. The error bars, which have been suppressed for clarity, are approximately the size of the markers themselves.*

3.5.1 Interactions with the Post Array

To assess the ability of the simulations to correctly describe the interactions between the molecules and the posts, we calculated chain hooking probabilities. A hook was defined as when portions of the chain exist in all four quadrants surrounding a post in a coordinate system whose origin is located at the center of the post; in addition, the chain must cross the upstream face of the post. Unlike in experiments, the coordinate system used to define the quadrants was not rotated to coincide with the direction of the local impinging electric field; however, this was not found to affect the determination of a hooking event. Figure 3.3 shows the results of this hooking analysis. The overall hooking probabilities on any post (A) show near quantitative agreement between the experiments and simulations except at De = 1 and 2 where the simulations give a moderate over prediction. The probability of hooking on the first row is also shown (B), and again there is near quantitative agreement except at De = 2.

It should be noted that the hooking probability on a post is known to depend on both the local De and Pe. [49, 21] In the simulations, however, only a single time scale can be matched to experiments which, in this case, is the relaxation time. This means that while De is the same between experiments and simulations, other time scales are not necessarily equivalent. This includes the diffusive time scale which is represented non-dimensionally by Pe. Indeed, we estimate Pe for the simulations is 15-40% higher than in experiments. This difference in Pe might account for some of the discrepancy between the hooking probabilities in experiments and simulations at De = 1 and 2. A better explanation, however, is that the number of experimental hooking events were undercounted at low De due to the limited resolution of images and the fact that many molecules barely deformed around the posts in the weak fields. This explanation is supported by movies of the

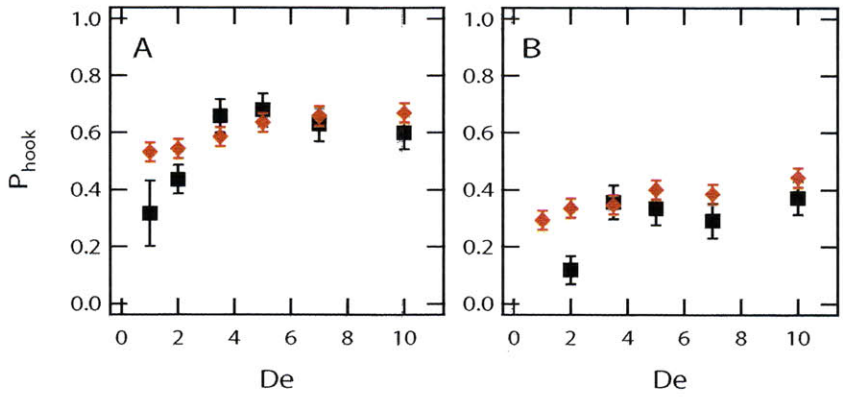

Fig. 3.3: *(A) Overall hooking probabilities on all rows in the post array vs De. (B) The hooking probabilities for only the first row of the array vs De. The black squares are the experimental data, and the red diamonds are the simulation data.*

simulated chains where many hooking events are seen to barely meet the above definition of a hook with the chains just crossing into all four quadrants surrounding the post for a very shot period of time. Simulations easily find and count this event as a hook while the reliability of experimental movie analysis is questionable at low field strengths.

An even more sensitive measure of the performance of the simulation model in predicting the DNA-post array interactions is given by the extension distribution of the chains as they leave the array. The extension $X_{ex,p}$ of the chains was measured when the most upstream part of the chain first left the post array. Figure 3.4 compares the extension distributions for experiments and simulations, and very good qualitative agreement is evident with the exception of De = 5. It is seen that with increasing electric field strength, the presence of the obstacle array leads to two distinct populations of molecules: those that only mildly stretch in the array and those that stretch significantly. Very few molecules stretch only moderately. Quantitatively, the simulations tend to show a sharper peak for the highly stretched population which also exists at a slightly higher extension, but this difference could be magnified by the simulations having a slightly higher Pe as previously discussed. But due to poor statistics, it is difficult to discern the actual behavior of the distributions at the experimental conditions of De = 3.5 and 5. Another consideration is that as the molecules unhook, their arms often hang off into the contraction. This means that the stretch leaving the post array is influenced by the behavior in the contraction. If the simulations have difficulty correctly predicting the stretch due to the field gradients in the contraction, it can taint the stretch coming off the post array as well.

Overall, we see that qualitatively, and often quantitatively, the experiments and simulations agree with respect to the behavior of the molecules as they interact with the post array. This is expected as Kim and Doyle [10] have shown the simulation model is fairly capable of reproducing experimental data for the collision of a molecule with a single post. Additionally, other Brownian dynamics simulation methods have had success reproducing the behavior of DNA being hydrodynamically driven through post arrays [93].

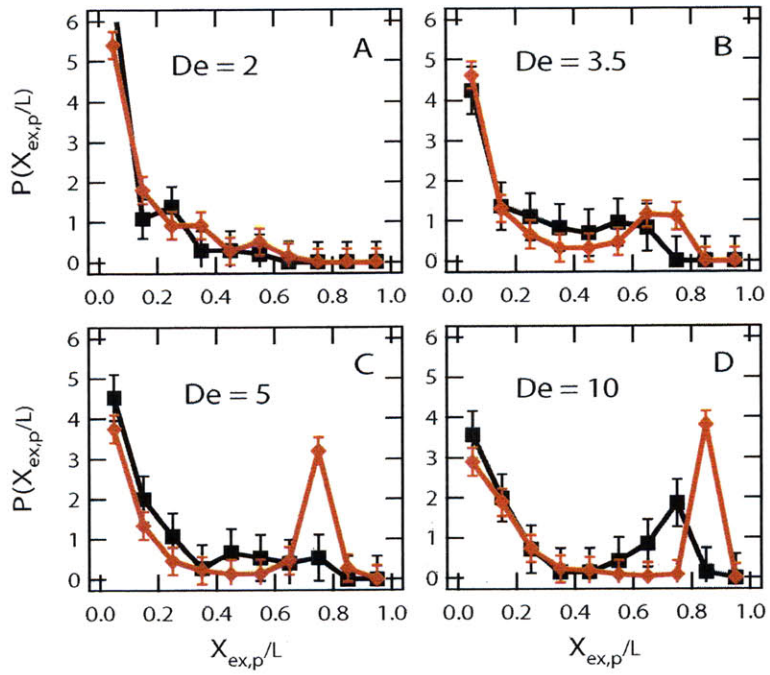

Fig. 3.4: *Distribution of the relative extensions of the chains as they pass the end of the post array for several values of De. The black squares are the experimental data, and the red diamonds are the simulation data.*

3.5.2 Stretching in the Contraction

We now consider the extension distributions of the chains as they reach the end of the contraction as shown in Figure 3.5. The simulations show that with increasing De more chains reach high extensions, in agreement with experimental results. However, simulations show a very sharp peak in the distribution at high extensions which is not mirrored in the experimental results. This discrepancy cannot be explained by unmatched Pe, and while poor experimental statistics may exacerbate the differences, statistics certainly cannot fully account for the discrepancies either, especially given their systematic nature. This suggests that the molecules are somehow more difficult to stretch in experiments than in simulations. However, it is also possible that the slightly higher extensions coming off the post array in the simulations could increase the final stretch at the end of the contraction.

In order to mitigate the influence of the post array on the analysis of the stretching within the contraction, we display in Figure 3.6 scatter plots that show for each chain the final stretch at the end of the contraction versus the intermediate stretch at the exit of the post array. This allows us to compare the deformation of molecules in the contraction that had the same initial stretch leaving the array. Again, the simulations are in qualitative agreement with experiments that DNA deformation in the post array leads to very strong stretching in the contraction. In particular, the simulations predict that a stretch of approximately 20% at the exit of the post array virtually

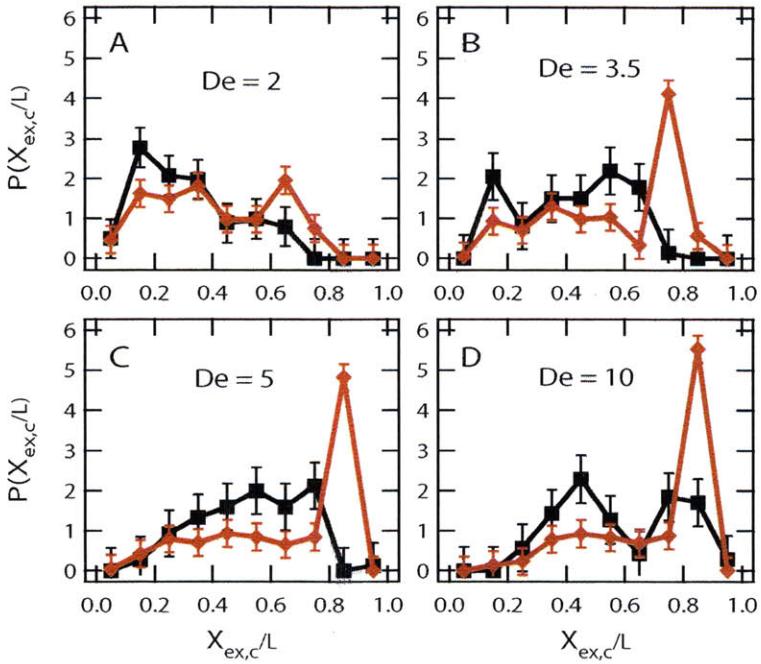

Fig. 3.5: *Distribution of the relative extensions of the chains as they reach the end of the contraction for several values of De. The black squares are the experimental data, and the red diamonds are the simulation data.*

guarantees strong stretching at the end of the contraction and additional predeformation beyond 20% adds little to the final stretch, as previously discovered in experiments.

On the other hand, there are some clear differences between the two results. First, the simulated chains seem to reach a larger maximum extension than molecules in experiments. This may suggest that De is not properly matched, but it is highly unlikely. The maximum extension found in the simulations is well-described by the infinite-strain limit predicted by a dumbbell model with the same De (the flat plateau region of the blue curve in Figure 3.6), and experimentally, even if De is off slightly due to uncertainty in the relaxation time of the molecules, correcting this small error would not change De enough to match the simulations. So simply claiming that the differences in maximum stretch are due to improperly matched time scales does not explain the differences.

The second discrepancy observed in Figure 3.6 is that the simulations predict that above a predeformation of about 20% the chains should almost always reach their maximum extension. This gives the stretch gain plots from simulations of De $\geq$ 3.5 (Figures 3.6B-D) a sharp "elbow" region where the trend turns flat. In contrast, experimental results show that the molecules often fall slightly short of their infinite-strain extension. Also, the amount the actual extension falls below the infinite-strain extension decreases with increasing predeformation. This leads to a wider elbow region in the stretch gain plots where the trend becomes slowly increasing instead of constant as in simulations. In order to demonstrate that our simulation results make sense based on the

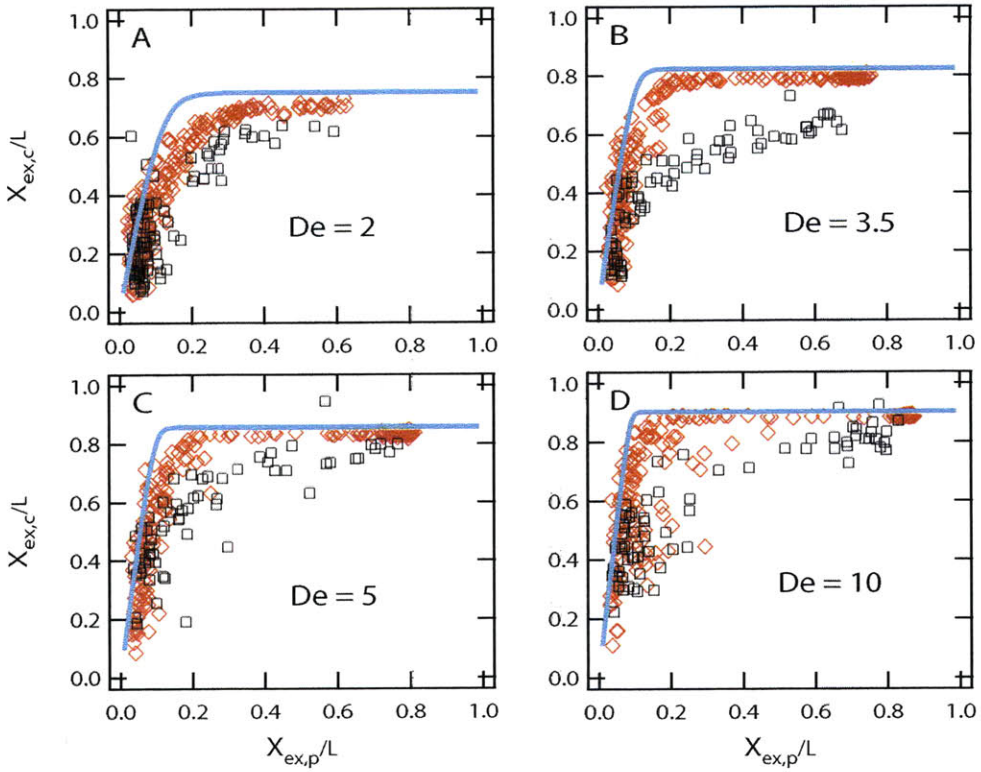

Fig. 3.6: *Scatter plots of the relative extension of the chains when they reach the end of the contraction vs the relative extension when the chains exit the post array for various De. The black squares are the experimental data, and the red diamonds are the simulation data. The solid blue line represents the predicted final stretch after an additional 2.5 units of strain using the dumbbell model given by eq. 3.1.*

physics incorporated, we have included in Figure 3.6 a prediction for the maximum stretch gain expected at the end of the contraction for a given amount of predeformation. This prediction was derived using the non-Brownian dumbbell model with a WLC spring force given by eq. 3.1. Based on the kinematic analysis of Randall et al., [22] we have assumed that after the post array there is approximately 2.5 units of strain left in the device. The model accounts for non-affine deformation of the chains, but does not include resistance to stretching due to internal configurations (i.e., molecular individualism) or the slightly different kinematic histories experienced by each chain. Nonetheless, it should provide a reasonable estimate for the maximum stretch gain expected. It is clearly seen from Figure 3.6 that the simulation results are well-described by the model while the experimental results only follow its qualitative trends.

Balducci and Doyle [97] also reported that many of the molecules in the elbow region, $0.2 < X_{ex,p}/L < 0.4$, contained a small fold in their conformation near their downstream ends as they

exited the contraction. The simulations do not predict this behavior since nearly all the molecules in this extension range after the post array will reach the infinite-strain limit. Indeed, movies of the simulated chains do not show the formation of these folded conformations.

Overall, our numerical model is capable of reproducing the broad qualitative behavior of the chains in the contraction after they have left the post array. For example, the simulations predict that mildly predeformed chains should stretch significantly in the contraction in agreement with experiments. However, the simulations do not correctly predict some of the finer qualitative behavior in the contraction.

3.5.3 Possible Reasons for the Observed Differences

The question, then, is why the simulation results do not always quantitatively match the results of the experiments? One possible reason already mentioned could be limited experimental statistics. But the systematic nature of the differences between simulations and experiments suggest that these differences are not artificial. A mismatch in time scales has also been discussed as one reason. This mismatch could be an improperly scaled De due to uncertainties in the relaxation time of the molecules, or it could be the slightly higher Pe in the simulations due to the inability of the simulations to match both the relaxation time and the diffusive time scale of experiments. However, neither of these possibilities has the potential to fully explain the differences seen.

A more plausible explanation is that additional physics is becoming important in the contraction, and a possible candidate is non-linear electrokinetic effects. The electric fields in the contraction are fairly strong, reaching $E \sim O(500\ \mathrm{V/cm})$, which could polarize the DNA molecules. Additionally, electric field gradients exist in the contraction that could potentially lead to dielectrophoretic effects which depend upon the term $\boldsymbol{E} \cdot \boldsymbol{\nabla} E$.

Dielectrophoresis occurs when particles (or macromolecules) polarize in strong electric fields. The resulting dipole then interacts with field gradients to attract or repel the particles to or from areas of strong field strengths. Most studies on the dielectrophoresis of DNA have used AC fields and created the necessary electric field gradients by placing the electrodes in close proximity to each other. There have been a few studies, however, that have considered electrodeless dielectrophoresis of DNA using microfabricated devices to shape the field lines, [111, 112, 113, 114] and some work has even been performed on DC fields. [113, 114]

Chou et al. [111] and Regtmeier et al. [112] used arrays of obstacles to bend and concentrate the field lines between the obstacles, and using an AC field, they trapped DNA between the obstacles. Regtmeier et al. also added a background DC field that led to the size-dependent separation of DNA molecules. This technique is similar to the previously proposed method of Ajdari and Prost [115] where AC dielectrophoretic traps transverse to a uniform DC field slow down DNA molecules in a size-dependent manner. Petersen et al. [113] also adapted the method suggested by Ajdari and Prost by using thin strips of gold laid down perpendicular to a DC electric field. The periodic strips attracted the electric field lines due to their high conductivity and created strong dielectrophoretic forces in a highly localized area near the edges of the gold strips. Parikesit et al. [114] used device walls to bend and concentrate field lines similar to Chou et al. [111] but with DC fields; however, their results were difficult to interpret and even seemed to contradict previous findings.

In our device, the magnitude of $\boldsymbol{E} \cdot \boldsymbol{\nabla} E$ reaches as high as $1.4 \times 10^7\ \mathrm{V^2/cm^3}$ which is only one order of magnitude smaller than that produced by Petersen et al. [113] in their trapping work. But in contrast to our device, the large values of $\boldsymbol{E} \cdot \boldsymbol{\nabla} E$ that led to trapping were highly localized near

the edges of the gold strips and only occurred over length scales of about 100 nm, comparable to the persistence length of DNA. This means that only small portions of the molecules would have been polarized and would have experienced a dielectrophoretic force. In our geometry, the strong fields and gradients exist over the entire length of the contraction which is $\ell_c = 80$ μm, which is much larger than the radius of gyration of T4-DNA and comparable to its contour length. So T4-DNA molecules in our device could polarize over their entire dimension which could possibly lead to even stronger non-linear electrokinetic effects than seen by Petersen et al. [113] In addition, the fact that DNA molecules are stretched in the contraction could render them more polarizable than when they are in their coiled state, [116] further increasing their sensitivity to non-linear electrokinetic effects.

It is currently difficult to study the possibility of such effects in the device because the molecules move very fast through the contraction due to the strong electric fields. A possible way to overcome this problem would be to tether the DNA molecule to a bead that can be optically trapped in the contraction so that the dynamic and steady-state extension behavior of the molecule can be studied.

Finally, it should again be noted that the current simulation model is able to match experimental results for a contraction without posts which raises the question, what is different about the situation with posts? The answer may lay in the fact that in an open channel, few of the chains actually come close to reaching the infinite-strain limit extension. Even in the case with posts, the simulations seem to be in fairly good agreements with experiments for those chains that do not stretch significantly. Additionally, in the case of open channels, the simulations have been shown to over predict the average stretch at higher De of 14 and 23 when compared to experiments [96]. At these De, the simulations began to over predict the populations of highly stretched molecules; however, the size of this population still only represented a small fraction of the total number of molecules. So any discrepancy in the behavior of highly stretched molecules between the simulations and experiments may not have been readily apparent. In the present situation, preconditioning leads to a large population of highly stretched molecules so that these differences should be more easily visible.

3.6 Conclusions

Simulations were performed for DNA molecules passing through a microcontraction preceded by a post array. The results were compared to those from previously performed experiments. Good qualitative and, at times, even quantitative agreement was found for the behavior of the chains during their interaction with the post array as measured by hooking probabilities and extension distributions of the chains as they exited the array. Qualitatively, the simulations strongly support the experimental finding that conformational preconditioning using an obstacle array can increase the stretching efficiency of a strain-limited microcontraction. Additionally, the simulations show that a predeformation of approximately 20% in the post array is nearly sufficient to guarantee strong stretching of a chain in the contraction in accordance with experiments.

Qualitative differences between the simulations and experiments were observed, particularly with respect to the population of highly stretched molecules. The simulations predict a very sharp peak in the extension distribution at high extensions for the molecules exiting the contraction while experimental results exhibited a broader and milder peak at high extensions. This difference causes simulations to over predict the average stretch of the molecules leaving the contraction. Finally, the molecules in experiments always seemed to fall slightly short of the infinite-strain

limit extension while simulations predict that nearly all molecules that left the post array with an extension above 20% would reach the infinite-strain limit by the end of the contraction. Possible reasons for the discrepancy between simulations and experiments are suggested with emphasis on non-linear electrokinetic effects. Additionally, experiments which might elucidate the behavior of molecules in the contraction are suggested.

Acknowledgments

The authors are grateful to Anthony Balducci and Jing Tang for many helpful discussions. This work was supported by the Singapore-MIT Alliance and by Award Number T32EB006348 from the National Institute of Biomedical Imaging and Bioengineering. The content is solely the responsibility of the authors and does not necessarily represent the official views of the National Institute of Biomedical Imaging and Bioengineering or the National Institutes of Health.

CHAPTER 4

Collisions with a Large, Ideally Conducting Post

Collisions of DNA molecules with microfabricated posts have received a great deal of attention over the last two decades. Fundamentally, post collisions are used to apply forces to polymers on the molecular length scale. This provides a simple and direct means to deform and manipulate individual molecules and has found possible application in the realm of DNA separations. Most previous studies on electrophoretic collisions with posts have either looked at insulating posts or completely neglected the field disturbances induced by the post. In this chapter, we consider collisions with conducting posts. In this case, molecules are attracted to and trapped on the post surface and only slowly escape due to a combination of diffusion and convection. We simplify this problem in order to distill the essential physics and develop analytical models that show that the important physics are well-understood. We simulate DNA collisions with large, conducting posts and compare the results to our theoretical predictions. Our findings, which are the first reported for conducting posts, should guide future studies and can be modified and applied to more complicated situations like moderately-sized posts or strong applied field strengths.

4.1 Overview

We theoretically treat the problem of DNA collisions with large, ideally conducting posts during electrophoresis. We exploit a separation of time and length scales that allows the problem to be broken into two connected problems: (i) compression of a molecule against a flat wall by an applied transverse field, and (ii) transport of a molecule across the post surface due to both tangential diffusion and convection. We address the former using a combination of statistical mechanics and blob theory, and the latter utilizing a Fokker-Planck approach. The theoretical predictions are then compared to the results of Brownian dynamics simulations.

4.2 Introduction

The development of microfluidics and "lab-on-a-chip" devices has opened a new era for the study of DNA electrophoresis and polymer physics more generally. Such devices have provided platforms to study fundamental problems in polymer physics [41, 30, 17, 105, 31, 32], and along the way, they have found applications in DNA separations [57, 15, 117] and genomic mapping [2, 118]. In particular, one problem that has received considerable attention is the collision of a DNA molecule with a cylindrical post [6, 5, 8, 49, 10, 119, 120].

Post arrays and similar devices have been used to achieve separation of large DNA molecules [121, 57, 92]. When a DNA molecule is electrophoretically or hydrodynamically driven into a post, it frequently forms a hook by wrapping around the post and into a hairpin-like configuration [52, 5, 8, 9, 93, 10]. The subsequent unhooking process, which is often described by a rope-over-pulley model, results in a length-dependent unhooking time and establishes the basis for length-based separations in large arrays of posts [52, 5, 6, 9, 98].

More fundamentally, collisions offer a simple way to manipulate individual molecules by applying forces on the molecular length scale. For example, post collisions have been used to deform DNA molecules so that their ensuing relaxation processes can be studied [30, 31]. In addition, our group has exploited collisions to "precondition" DNA for subsequent stretching in an elongational field [97] in order to overcome molecular individualism [24]. Cylindrical posts have also been used to create field gradients near the post surface that can stretch and deform molecules [49, 21].

Past post work has tended to focus on the small post limit where the posts are much smaller than the equilibrium DNA coil size. These "point obstacles" virtually guarantee the formation of a large number of molecular hooks as long as the field strength is strong enough [53] and the posts are properly positioned [55, 99]. However, from a theoretical perspective, modeling of the direct interactions between a point obstacle and a molecule is fairly simple with the post being treated as little more than a simple pivot point during a collision [9]. That is not to say that collisions with point obstacles are trivial. The dynamics of such events can be quite complex [9], but the characteristics of the post itself are completely neglected. When the finite size of the posts is taken into account, the problem becomes much richer. The relative size of the post becomes important [8, 49], and new types of collision processes are possible (e.g., "roll-offs" [8]). In addition, disturbances of the electrophoretic velocity field due to the presence of the post must be considered [49, 21, 122].

When finite-sized posts were first examined, the field disturbances due to the post were neglected, and a uniform field was assumed everywhere [8]. Later, when researchers began to account for the field disturbances, the posts were assumed to be electrically insulating so that the field lines

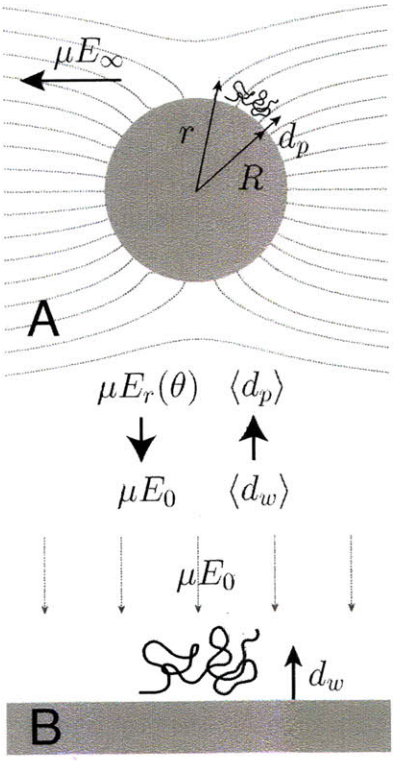

Fig. 4.1: *(A) Cartoon of a DNA molecule being electrophoretically driven into an ideally conducting post along with the field lines for the electrophoretic velocity field. This is referred to as the "post problem". (B) DNA molecule is driven into a flat surface by a uniform transverse electrophoretic velocity field. This problem is called the "local problem". Also shown is the information flow between the two problems.*

avoid and are repelled by the post surface [49, 21, 10]. Indeed, on the post surface, the field lines are everywhere tangential to the post. The deformation of the field lines leads to field gradients near the post surface that are able to deform molecules both on the front and backside of the posts [21], and this deformation aids in hook formation [49]. However, a large number of molecules are quickly swept around the post by the nearly tangential field lines close to the surface. These molecules and their trajectories are only weakly affected by the presence of the post.

4.3 Problem Statement

In this work, we consider the case of an ideally conducting post. By this, we mean a post whose dielectric constant ϵ_p is much greater than that of the surrounding fluid ϵ_f (i.e., $\epsilon_p \gg \epsilon_f$). Unlike the insulating case, the field lines for a conducting post, which are shown in Figure 4.1A, are attracted to and focused by the post. This means the molecules also tend to be attracted to the post and interact very strongly with it. We are interested in understanding the fundamental physics that govern a molecule that is being electrophoretically driven into an ideally conducting post. Since this is the first attempt to study conducting posts, we only consider linear electrophoresis in our analysis and neglect any nonlinear electrokinetic effects which may be present.

4.4 Initial Analysis of Problem

4.4.1 Qualitative Features of a Collision

The electrophoretic velocity field $\mu \boldsymbol{E}$ surrounding an ideally conducting post is given by

$$\frac{\mu \boldsymbol{E}}{\mu E_\infty} = -\left[1 + \left(\frac{r}{R}\right)^{-2}\right] \cos\theta \mathbf{e}_r + \left[1 - \left(\frac{r}{R}\right)^{-2}\right] \sin\theta \mathbf{e}_\theta, \tag{4.1}$$

where μ is the electrophoretic mobility of the molecule, E_∞ is the strength of the electric field far away from the post applied in the $-\mathbf{e}_x$ direction, R is the radius of the post, and r and θ give the position in polar coordinates with the origin at the post center.

On the post surface at $r = R$, it is clear from Equation 4.1 that μE_r is strong over most of the surface while μE_θ is identically equal to zero (see Figure 4.1A). Therefore, the field lines always intersect the post surface perpendicularly. On the upstream side of the post ($-\pi/2 < \theta < \pi/2$) the field lines are directed into the post while on the downstream side ($\pi/2 < \theta < 3\pi/2$) the field lines are directed away from and out of the post. As a molecule approaches the post, it is driven into the upstream side of the impenetrable surface. For our study, we have restricted our analysis to large posts, whereby we mean that $R \gg R_g$, where R_g is the radius of gyration of the colliding molecule. This guarantees that hooking of the molecule around the post is precluded and that, for reasonable applied field strengths, the field gradients are weak so that strong stretching of a molecule is also impossible. Therefore, the molecule is compressed and "trapped" against the post by the strong radial field.

There are two mechanisms by which a molecule can "escape" from the post: diffusion and convection. Clearly, the molecule experiences tangential diffusion, and given enough time, diffusion will guarantee eventual escape. But the molecule also experiences a weak tangential velocity v_θ.

Although $\mu E_\theta = 0$ for $r = R$, for $r > R$ it is nonzero. The strength of μE_θ increases with increasing r, and it is always directed toward the downstream side of the post. Since a compressed

molecule still has some finite size, it is exposed to the weak tangential field that exists just off the post surface. This means that the average tangential velocity of the molecule $\langle v_\theta \rangle \neq 0$, and it is slowly convected around the post and finally "escapes". Since $\langle v_\theta \rangle$ depends upon the distance of the molecule from the post surface, we must understand how μE_r compresses the molecule against the post and affects its size.

4.4.2 Analysis of Field Near the Post Surface

Because molecules are "trapped" against the post, we are particularly interested in the behavior of $\mu \boldsymbol{E}$ near the post surface. We can exploit the fact that $R \gg R_g$ and linearize the field around

$$\frac{r}{R} \approx \frac{R + R_g}{R} \approx 1. \tag{4.2}$$

Additionally, we can replace the radial position r with an new coordinate d_p (see Figure 4.1A) which is the distance from the post surface

$$\frac{d_p}{R} = \frac{r}{R} - 1 \ll 1. \tag{4.3}$$

Combining these two approximations, we can simplify the nonlinear radial term in Equation 4.1:

$$\left(\frac{r}{R}\right)^{-2} \approx 1 - 2\left(\frac{r}{R} - 1\right) \approx 1 - 2\frac{d_p}{R}. \tag{4.4}$$

If we use this result to approximate $\mu \boldsymbol{E}$ near the post surface, we obtain

$$\frac{\mu \boldsymbol{E}}{\mu E_\infty} \approx -2\cos\theta \mathbf{e}_r + 2\frac{d_p}{R}\sin\theta \mathbf{e}_\theta. \tag{4.5}$$

4.4.3 Two Connected Problems

The disparity of the length scales due to the large post size, leads to a separation of time scales between the dynamics occurring in each of the dimensions. In the $\mathbf{e}_\theta$ direction, the convective and diffusive time scales are based on the length R, so the molecular escape time is quite large. On the other hand, compression in the $\mathbf{e}_r$ direction is due to a competition between convection toward the post surface and diffusion away from it. This results in a time scale for compression based on lengths similar to R_g so that it is very short. Therefore, the dynamics in the $\mathbf{e}_r$ direction occur much more quickly than those in the $\mathbf{e}_\theta$ direction. This allows us to break the collision problem into the two connected problems shown in Figure 4.1.

We refer to the first of these as the "post problem" which occurs on the scale of the post $\sim R$. From this vantage point, the molecule looks as though it is being transported across the post surface due to a combination of tangential diffusion and convection. The average tangential velocity is approximated based on Equation 4.5:

$$\langle v_\theta \rangle \approx 2\mu E_\infty \frac{\langle d_p \rangle}{R}\sin\theta. \tag{4.6}$$

The average distance from the wall $\langle d_p \rangle$ is based on the fast compression dynamics that occur in the

radial dimension, and since $\langle d_p \rangle = f(\mu E_r \approx -2\mu E_\infty \cos\theta)$, it varies as the molecule moves across the post surface. But because the compression dynamics are fast, we can make a pseudosteady approximation and assume that $\langle d_p \rangle$ is always in equilibrium with the local radial field μE_r.

The second problem shown in Figure 4.1B is the "local problem" which occurs on the length scale of $\sim R_g$. Effectively, we have "zoomed" in on the molecule. We can neglect the curvature inherent in the post problem because the post surface now looks like a flat wall and $\mu \boldsymbol{E}$ looks uniform. The only important phenomenon occurring at this scale is the compression of the molecule by the transverse component of the uniform field which we call μE_0 for the local problem. We can analyze this situation to determine how the average distance from the wall, which we call $\langle d_w \rangle$ for the local problem, depends upon μE_0.

These two problems are clearly connected as seen in Figure 4.1. The post problem provides the local problem with the strength of the transverse field ($\mu E_0 = \mu E_r(\theta)$), and in return, the local problem feeds the post problem the average distance from the post ($\langle d_p \rangle = \langle d_w \rangle$) for use in determining the average tangential velocity $\langle v_\theta \rangle$.

4.4.4 Approach

In our detailed analysis of the collision problem, we begin by examining the local problem of a Gaussian chain driven into a flat wall by a uniform transverse field. We use a combination of blob theory and statistical mechanics to derive expressions and scalings for $\langle d_w \rangle$ as a function of μE_0. We confirm these scalings using Brownian dynamics simulations.

We then turn to the post problem where we use our results from the local case to predict $\langle v_\theta \rangle$. After confirming the validity of our predictions using simulations, we incorporate diffusion into our theoretical model by turning to a Fokker-Planck equation and calculating the mean escape time of a molecule based on the initial collision location. These results are compared to simulations as well.

4.5 Brownian Dynamics Simulation

DNA molecules are modeled as chains of N_b beads connected by $N_\mathrm{s} = N_\mathrm{b} - 1$ Hookean springs. The equation of motion for the position $\boldsymbol{r}_i$ of the ith bead is

$$\frac{d\boldsymbol{r}_i}{dt} = \mu \boldsymbol{E}(\boldsymbol{r}_i) + \frac{1}{\zeta_\mathrm{b}} \left(\boldsymbol{F}_i^\mathrm{S} + \boldsymbol{F}_i^\mathrm{B} \right) \tag{4.7}$$

where μ is the electrophoretic mobility of the chain, ζ_b is the bead drag coefficient, $\boldsymbol{F}_i^\mathrm{S}$ is the total spring force felt by the bead, and $\boldsymbol{F}_i^\mathrm{B}$ is the Brownian force.

We nondimensionalize Equation 4.7 based on the length and time scales of a spring: $\ell_\mathrm{s} \equiv \sqrt{k_\mathrm{B}T/H}$ and $\tau_\mathrm{b} \equiv \ell_\mathrm{s}^2/D_\mathrm{b}$, respectively, where H is the Hookean spring constant and D_b is the bead diffusivity. The nondimensional variables for the local problem are

$$\hat{\boldsymbol{r}} \equiv \frac{\boldsymbol{r}}{\ell_\mathrm{s}}, \hat{t} \equiv \frac{t}{\tau_\mathrm{b}}, \hat{\boldsymbol{E}} \equiv \frac{\boldsymbol{E}}{E_0}, \hat{\boldsymbol{F}} \equiv \frac{\boldsymbol{F}}{k_\mathrm{B}T/\ell_\mathrm{s}} \tag{4.8}$$

(for the post problem we nondimensionalize $\boldsymbol{E}$ using E_∞). This gives the dimensionless form of

the equation of motion:

$$\frac{d\hat{\boldsymbol{r}}_i}{d\hat{t}} = Pe_{\mathrm{b},0}\hat{\boldsymbol{E}}\left(\hat{\boldsymbol{r}}_i\right) + \hat{\boldsymbol{F}}_i^{\mathrm{S}} + \hat{\boldsymbol{F}}_i^{\mathrm{B}} \tag{4.9}$$

where $Pe_{\mathrm{b},0} = \mu E_0 \ell_{\mathrm{s}}/D_{\mathrm{b}}$ is the bead Péclet number (or for the post problem, $Pe_{\mathrm{b},\infty} = \mu E_\infty \ell_{\mathrm{s}}/D_{\mathrm{b}}$).

The nondimensional Brownian force is given by

$$\hat{\boldsymbol{F}}_i^{\mathrm{B}} = \sqrt{\frac{24}{\Delta\hat{t}}}\left[\mathbf{r}_{\mathrm{n}}\right]_i \tag{4.10}$$

where $\Delta\hat{t}$ is the dimensionless time step and $[\mathbf{r}_{\mathrm{n}}]_i$ are uniform random numbers such that each component $[\mathbf{r}_{\mathrm{n}}]_i^j \in [-1/2, 1/2]$, where j denotes the coordinate x, y, or z. Equation 4.10 has been normalized so that it provides the proper variance for the Brownian force in order to satisfy the fluctuation dissipation theorem.

The net dimensionless spring force on the ith bead is

$$\hat{\boldsymbol{F}}_i^{\mathrm{S}} = \begin{cases} \hat{\boldsymbol{f}}_{i,2}^{\mathrm{s}}, & i = 1, \\ \hat{\boldsymbol{f}}_{i,i+1}^{\mathrm{s}} + \hat{\boldsymbol{f}}_{i,i-1}^{\mathrm{s}}, & 1 < i < N_{\mathrm{b}}, \\ \hat{\boldsymbol{f}}_{i,N_{\mathrm{b}}-1}^{\mathrm{s}}, & i = N_{\mathrm{b}}, \end{cases} \tag{4.11}$$

where $\hat{\boldsymbol{f}}_{i,j}^{\mathrm{s}}$ is the force exerted on the ith bead by the jth bead. We have included two contributions to the spring force $\hat{\boldsymbol{f}}_{i,j}^{\mathrm{s}} = \hat{\boldsymbol{f}}_{i,j}^{\mathrm{s,b}} + \hat{\boldsymbol{f}}_{i,j}^{\mathrm{s,w}}$. The first is the simple bulk Hookean spring force:

$$\hat{\boldsymbol{f}}_{i,j}^{\mathrm{s,b}} = \hat{\boldsymbol{r}}_j - \hat{\boldsymbol{r}}_i. \tag{4.12}$$

The second contribution $\hat{\boldsymbol{f}}_{i,j}^{\mathrm{s,w}}$ is a correction for the presence of the post/wall.

When a spring is located near an impenetrable surface, it disrupts the underlying random walk upon which the entropic spring force is based. In bulk, the configuration space of a Gaussian chain exhibits axial symmetry around its spring (end-to-end) vector. This leads to a Hookean spring force that is always directed along the direction of the spring vector as is manifest in Equation 4.12. However, in the presence of a surface, the chain's configuration space is restricted and this axial symmetry is broken. This leads to purely entropic forces that push the chain away from the surface and that are not necessarily directed along the direction of the spring vector. Consideration of this force renders the spring behavior more realistic and actually allows us to use fewer beads (and, therefore, fewer computational resources) in order to reach the predicted scaling regimes.

We can account for this effect by including a correction term in the spring force [71]. If the surface is a flat plane that passes through the origin, the correction is given by

$$\hat{\boldsymbol{f}}_{i,j}^{\mathrm{s,w}} = \left\{ \frac{2\left(\hat{\boldsymbol{r}}_j \cdot \boldsymbol{n}_w\right)}{\exp\left[2\left(\hat{\boldsymbol{r}}_i \cdot \boldsymbol{n}_w\right)\left(\hat{\boldsymbol{r}}_j \cdot \boldsymbol{n}_w\right)\right] - 1} \right\} \boldsymbol{n}_w \tag{4.13}$$

where $\boldsymbol{n}_w$ is the unit normal pointing out of the surface. This term always pushes the beads away from the wall. It diverges as the beads approach the surface and is sufficient to prevent the beads from passing through the wall, so it has the secondary benefit that we do not have to include an additional force dedicated to imposing the wall excluded volume. This expression can be directly applied for the local problem since the surface is flat. For the post problem, we assume that locally

the post looks flat and neglect any correction due to the curvature of the post surface.

The time-stepping scheme we used for the local problem is as follows:

$$\Delta\hat{t} = \begin{cases} N_b^{-1} Pe_{b,0}^{-2}/5000, & Pe_{b,0} < N_b^{-3/2}, \\ Pe_{b,0}^{-4/3}/5000, & N_b^{-3/2} \leq Pe_{b,0} < 1, \\ Pe_{b,0}^{-2}/5000, & Pe_{b,0} \geq 1. \end{cases} \tag{4.14}$$

For the post problem, we used the same scheme with $Pe_{b,0} = 2Pe_{b,\infty}$.

4.6 Analysis of Local Problem/Field-Induced Compression

The local problem shown in Figure 4.1B is characterized by a polymer chain near a flat wall undergoing field-induced compression by a uniform electrophoretic velocity field μE_0 applied transverse to the wall in the $-\mathbf{e}_z$ direction. Note that for the local problem we have neglected the curvature inherent in the global post problem. Therefore, we use Cartesian coordinates when describing the local problem. But we will resume using cylindrical coordinates in Section 4.7 when we return to the global post problem. In our analysis of this problem, we first consider the behavior of a point particle and of a Hookean dumbbell. Using statistical mechanics, we can derive exact analytical results for these cases which provide basic insight into the problem and a way to validate our numerical model. We then look to blob theory to tackle the more complicated problem of a multibead Gaussian chain.

4.6.1 Point Particle and Dumbbell

The average distance from the wall for a point particle with a diffusivity of D is easily shown to be $\langle d_w^{\mathrm{pp}} \rangle = D/\mu E_0$. This result owes its simplicity to the fact that there is no geometric length scale in the problem because the wall is infinitely large and the particle is infinitely small (there is no spring to consider in this case). Therefore, the only length scale is the dynamic one, $\langle d_w^{\mathrm{pp}} \rangle$, which follows from balancing the opposing forces of convection and diffusion on the particle. If we arbitrarily define a field-independent length scale ℓ for the problem, then the result for a point particle becomes

$$\frac{\langle d_w^{\mathrm{pp}} \rangle}{\ell} = Pe_\ell^{-1} \tag{4.15}$$

where $Pe_\ell = \mu E_0 \ell / D$ is a Péclet number based on the arbitrary length scale ℓ. This result is useful because we expect that even large multibead chains should recover point particle behavior when the applied field strength is extremely weak.

The derivation for the average distance from the wall for a Hookean dumbbell $\langle d_w^{\mathrm{db}} \rangle$ is more involved. Due to the linearity of the Hookean spring, all three dimensions act independently, and the problem is 1D in the $\mathbf{e}_z$ direction. The probability density of finding a dumbbell with a center of mass located at d_w and a spring length of q is proportional to the Boltzmann distribution

$$P(d_w, q) \sim \exp\left(-2Pe_{b,0}\frac{d_w}{\ell_s}\right)\left[\exp\left(-\frac{1}{2}\frac{q^2}{\ell_s^2}\right) - \exp\left(-2\frac{d_w^2}{\ell_s^2}\right)\right] \tag{4.16}$$

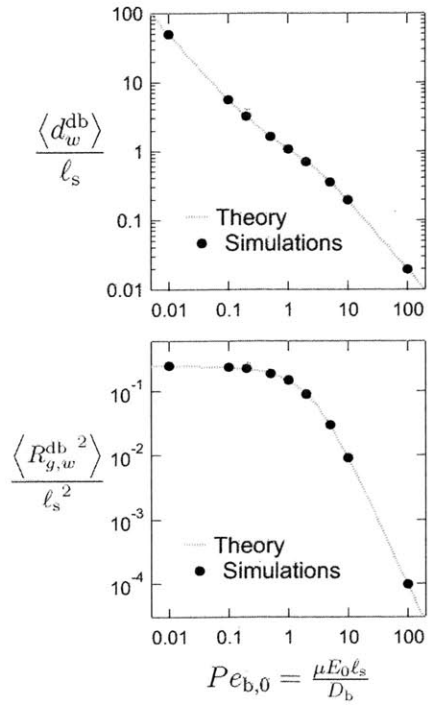

Fig. 4.2: *Plot of the average distance of the center of mass* $\langle d_w^{\mathrm{db}} \rangle$ *from a flat wall for a Hookean dumbbell in a uniform field versus the field strength for the BD simulations along with the analytical result given by Equation 4.17 (top). Plot of the radius of gyration squared of a Hookean dumbbell in the direction transverse to the wall* $\left\langle R_{g,w}^{\mathrm{db}\ 2} \right\rangle$ *versus the field strength for the simulations and the exact solution given by Equation 4.18 (bottom).*

where $Pe_{\mathrm{b},0} = \mu E_0 \ell_\mathrm{s}/D_\mathrm{b}$. From this, we can determine the average distance from the wall

$$\frac{\langle d_w^{\mathrm{db}} \rangle}{\ell_\mathrm{s}} = \frac{1}{2} \frac{\exp(-\frac{1}{2}Pe_{\mathrm{b},0}^2)\left(Pe_{\mathrm{b},0}^{-1} + Pe_{\mathrm{b},0}\right) + \sqrt{\frac{\pi}{2}}\mathrm{erfc}(\frac{1}{\sqrt{2}}Pe_{\mathrm{b},0})\left(Pe_{\mathrm{b},0}^{-2} - 2 - Pe_{\mathrm{b},0}^2\right)}{\sqrt{\frac{\pi}{2}}\mathrm{erfc}(\frac{1}{\sqrt{2}}Pe_{\mathrm{b},0})\left(Pe_{\mathrm{b},0}^{-1} + Pe_{\mathrm{b},0}\right) - \exp(-\frac{1}{2}Pe_{\mathrm{b},0}^2)} \quad . \tag{4.17}$$

This result is shown in Figure 4.2.

There are two regimes connected by a transition region that describe the behavior of $\langle d_w^{\mathrm{db}} \rangle$. The first is a weak field regime where $Pe_{\mathrm{b},0} \ll 1$. Under these conditions, the dumbbell typically is far away from the wall and only occasionally interacts with it. Therefore, the dumbbell behaves very much like a point particle. Indeed, in the limit of $Pe_{\mathrm{b},0} \ll 1$ the expression given in Equation 4.17 reduces to $\langle d_w^{\mathrm{db}} \rangle / \ell_\mathrm{s} \approx (2Pe_{\mathrm{b},0})^{-1}$ which is the expected behavior of a point particle with a diffusivity of $D = D_\mathrm{b}/2$ (see Figure 4.2).

The transition region occurs around $Pe_{\mathrm{b},0} \approx 1$. At this field strength, $\langle d_w^{\mathrm{db}} \rangle$ is comparable to the equilibrium spring length ℓ_s, and the dumbbell no longer acts like a single point particle. This can clearly be seen by considering the 1D radius of gyration of the dumbbell in the direction transverse to the wall $R_{g,w}^{\mathrm{db}}$ which is given by

$$\frac{\left\langle {R_{g,w}^{\mathrm{db}}}^2 \right\rangle}{{\ell_\mathrm{s}}^2} = \frac{1}{12} \frac{\sqrt{\frac{\pi}{2}}\mathrm{erfc}(\frac{1}{\sqrt{2}}Pe_{\mathrm{b},0})Pe_{\mathrm{b},0}\left(3Pe_{\mathrm{b},0}^{-2} + 6 + Pe_{\mathrm{b},0}^2\right) - \exp(-\frac{1}{2}Pe_{\mathrm{b},0}^2)\left(5 + Pe_{\mathrm{b},0}^2\right)}{\sqrt{\frac{\pi}{2}}\mathrm{erfc}(\frac{1}{\sqrt{2}}Pe_{\mathrm{b},0})\left(Pe_{\mathrm{b},0}^{-1} + Pe_{\mathrm{b},0}\right) - \exp(-\frac{1}{2}Pe_{\mathrm{b},0}^2)} \tag{4.18}$$

and can also be seen in Figure 4.2. For $Pe_{\mathrm{b},0} \ll 1$, $\left\langle {R_{g,w}^{\mathrm{db}}}^2 \right\rangle / {\ell_\mathrm{s}}^2$ remains unperturbed and maintains a constant value of 1/4. But as $Pe_{\mathrm{b},0}$ approaches 1, $\left\langle {R_{g,w}^{\mathrm{db}}}^2 \right\rangle / {\ell_\mathrm{s}}^2$ begins to drop as the internal mode of the dumbbell is affected by the wall presence.

The second regime is a high field limit where $Pe_{\mathrm{b},0} \gg 1$. When the field strength is very large, the dumbbell is strongly pushed against the wall, and both beads are always very near the wall surface ($r_{1,z}/\ell_\mathrm{s}, r_{2,z}/\ell_\mathrm{s} \ll 1$). This also guarantees that the distance between the beads in the transverse direction is always very small compared to the equilibrium spring size ($|r_{2,z} - r_{1,z}|/\ell_\mathrm{s} \ll 1$). The result of these two conditions is that the transverse component of the bulk spring force $(\hat{\boldsymbol{f}}_{i,j}^{\mathrm{s,b}})_z$ given by Equation 4.12 is negligible, and the wall correction for the spring force on the ith bead $(\hat{\boldsymbol{f}}_{i,j,}^{\mathrm{s,w}})_z$ given by Equation 4.13 approaches $\approx (r_{i,z}/\ell)^{-1}$. These two findings indicate that the beads become uncoupled in the $\mathbf{e}_z$ direction when the dumbbell is pushed strongly against the wall. So for large field strengths, the two ends of the dumbbell should act independently of each other and behave as point particles of diffusivity $D = D_\mathrm{b}$. Indeed, in the limit of $Pe_{\mathrm{b},0} \gg 1$, Equation 4.17 reduces to $\langle d_w^{\mathrm{db}} \rangle / \ell_\mathrm{s} \approx 2Pe_{\mathrm{b},0}^{-1}$ which, except for the factor of 2, is the expected result for a point particle (see Figure 4.2). The factor of 2 comes from the wall correction for the spring force $(\hat{\boldsymbol{f}}_{i,j,}^{\mathrm{s,w}})_z \approx (r_{i,z}/\ell)^{-1}$ which does not exist in the case of a true point particle. But this additional force does not change the predicted scaling with $Pe_{\mathrm{b},0}$; it just affects the numerical prefactor.

Also shown in Figure 4.2 are the results from our BD simulations of a molecule pushed against a flat wall. The data from the simulations match the exact analytical results thereby validating our numerical model.

4.6.2 Multibead Chain

The added complexity of multibead chains does not allow for exact analytical solutions; however, based on the point particle and dumbbell results we can predict the behavior of multibead chains at both very small and very large $Pe_{b,0}$. Additionally, the increased number of internal modes leads to the emergence of a third, intermediate "blob" regime, where globally a chain is strongly deformed by the applied field, but locally individual springs remain virtually unperturbed from their equilibrium configurations.

For very strong field strengths where $Pe_{b,0} \gg 1$, the beads become uncoupled in the transverse direction just as they do in the case of a dumbbell. Therefore, the individual beads behave very much like point particles so that $\langle d_w \rangle / \ell_s \approx 3Pe_{b,0}^{-1}$ in the case of $N_b \gg 1$. The prefactor is different from the dumbbell result because, except for the ends, each bead is connected to two springs instead of just one. Additionally, it can be shown that $\langle {R_{g,w}}^2 \rangle / {\ell_s}^2 \approx 3Pe_{b,0}^{-2}$.

For for very weak field strengths (we will define how weak momentarily), we expect to recover the point particle behavior exhibited by a dumbbell. In the case of a chain with N_b beads, the chain diffusivity is given by $D = D_b/N_b$ (we assume the chains are free-draining), and we predict that $\langle d_w \rangle / \ell_s \approx (N_b Pe_{b,0})^{-1}$. Additionally, we expect the 1D radius of gyration to take on its equilibrium value of $\langle {R_{g,w}}^2 \rangle_{eq} / {\ell_s}^2 \approx N_b/6$ (which assumes $N_b \gg 1$). The weak field regime is characterized by the condition that $\langle d_w \rangle \gg \sqrt{\langle {R_{g,w}}^2 \rangle_{eq}}$ which guarantees that the configuration of the chain is nearly unperturbed from its equilibrium configuration. This condition is first violated when $(N_b Pe_{b,0})^{-1} \sim \sqrt{N_b/6}$. So we can say that weak field regime is defined for $Pe_{b,0} \ll N_b^{-3/2}$.

This leaves a large region between the weak and high field regimes where $N_b^{-3/2} \ll Pe_{b,0} \ll 1$. This is the new "blob" regime that emerges as N_b increases, and it is characterized by strong global deformation of the chain structure while leaving smaller subunits of the chain fairly unperturbed. These subunits are referred to as "blobs" and are often used in scaling analyses associated with chains confined in slits and tubes. We can make use of the blob theory framework to analyze the problem of field-induced confinement by introducing an electrical energy associated with the applied electrophoretic velocity field as shown in Figure 4.3.

We start by considering the well-known problem of a chain confined between two parallel plates separated by a distance h. For an ideal chain consisting of N_K Kuhn steps of length b_K, it can be shown that the energy required to confine the chain is proportional to the number of blobs formed [68] and scales as

$$G_{conf} \sim k_B T N_K \left(\frac{h}{b_K} \right)^{-2}. \tag{4.19}$$

In the case of field-induced confinement, we replace the constant plate separation h with a field-dependent compression size d_w (see Figure 4.3). We also introduce an electrical energy for the chain

$$G_{elec} \sim N_K q_{K,eff} E_0 d_w \tag{4.20}$$

where $q_{K,eff}$ is the effective charge of a Kuhn segment. $q_{K,eff}$ can be derived by considering the free solution electrophoresis of a Kuhn segment. By balancing the electric force $q_{K,eff} E_0$ driving the segment forward against the opposing drag force $-\zeta_K v = -\zeta_K \mu E_0$, where ζ_K is the drag coefficient for a Kuhn step, we discover that $q_{K,eff} = \zeta_K \mu$.

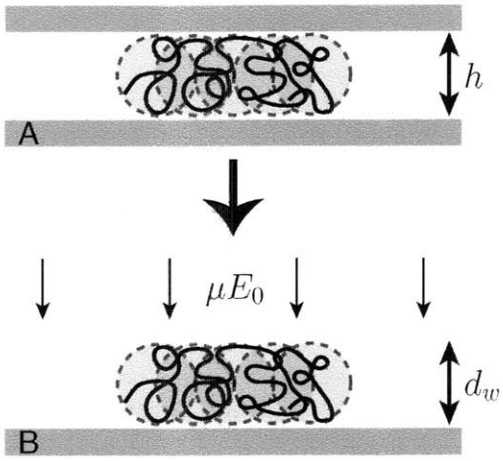

Fig. 4.3: *Cartoon depicting the blob scaling approach used to find d_w. The results for slitlike confinement are used to find the entropic penalty for confinement. This energy is then added to an electrical energy in the case of field-induced confinement. The total energy is minimized to find d_w.*

By minimizing the total energy $G_{\text{tot}} \sim G_{\text{conf}} + G_{\text{elec}}$ with respect to d_w, we find that

$$\frac{\langle d_w \rangle}{b_{\text{K}}} \sim \left(\frac{b_{\text{K}} \mu E_0}{k_{\text{B}} T / \zeta_{\text{K}}} \right)^{-1/3} \sim Pe_{\text{K}}^{-1/3} \tag{4.21}$$

where Pe_{K} is a Péclet number based on a Kuhn step. It is interesting to note that d_w is independent of chain length in the blob regime. This is because adding chain length increases the number of blobs, but it does not change their size.

Also, we expect in the blob and high field regimes that $R_{g,w} \sim d_w$. This is reasonable since both describe the size of the compressed chain given that it is always pushed against the wall. This is not the case in the weak field regime where $R_{g,w}$ is basically unperturbed from its bulk value.

Finally, we can adapt these results to bead-spring chains by substituting springs for Kuhn steps. In doing so, we replace b_{K} with ℓ_{s}, ζ_{K} with ζ_{b}, and Pe_{K} with $Pe_{\text{b},0}$.

Combining all of our above predictions for multibead chains, we have for the average distance from the wall:

$$\frac{\langle d_w \rangle}{\ell_{\text{s}}} \approx \begin{cases} (N_{\text{b}} Pe_{\text{b},0})^{-1}, & Pe_{\text{b},0} \ll N_{\text{b}}^{-3/2}, \\ \alpha Pe_{\text{b},0}^{-1/3}, & N_{\text{b}}^{-3/2} \ll Pe_{\text{b},0} \ll 1, \\ 3Pe_{\text{b},0}^{-1}, & Pe_{\text{b},0} \gg 1; \end{cases} \tag{4.22}$$

and for the average 1D radius of gyration squared:

$$\frac{\langle R_{g,w}^2 \rangle}{\ell_{\text{s}}^2} \approx \begin{cases} N_{\text{b}}/6, & Pe_{\text{b},0} \ll N_{\text{b}}^{-3/2}, \\ \beta Pe_{\text{b},0}^{-2/3}, & N_{\text{b}}^{-3/2} \ll Pe_{\text{b},0} \ll 1, \\ 3Pe_{\text{b},0}^{-2}, & Pe_{\text{b},0} \gg 1. \end{cases} \tag{4.23}$$

In both of these expressions, we have included proportionality constants, α and β, to describe the blob regime. This is to highlight the fact that, unlike the weak and strong field regimes, we only have scalings for the behavior of the chains in the blob regime. We have no way of determining α and β a priori, so we must fit real data if we wish to determine them.

In order to test our predictions, we simulated several different chain lengths (N_b = 20, 40, and 100) at various values of $Pe_{b,0}$. The results of these simulations are shown in Figure 4.4. The theoretical predictions for the three different regimes given in Equations 4.22 and 4.23 are also included as well as slope lines for the predicted scalings.

There is excellent agreement between simulations and theory. Not only do the strong and weak field regimes exhibit the predicted scalings, but they also asymptotically approach the predicted quantitative values as well. The locations of the transitions between regimes are also correctly predicted.

The emergence of an apparent scaling regime with increasing N_b between the strong and weak field regions confirms the existence of a blob regime. Indeed, the simulation results match the predicted blob theory scalings. But in order to more rigorously demonstrate the existence of the blob regime, we plotted the ratio of $\langle d_w \rangle$ and $\sqrt{\langle R_{g,w}^2 \rangle}$. In regions where both of these quantities are predicted to scale the same way, we expect to see a broad plateau in the plot of their ratio. $\langle R_{g,w}^2 \rangle$ is a constant in the weak field regime, so the ratio should diverge as $Pe_{b,0}$ decreases. In the strong field regime, the ratio should plateau to a constant value of $\sqrt{3}$. If the blob regime does, indeed, exist, then a similar plateau should be seen for $N_{b,0}^{-3/2} \ll Pe_{b,0} \ll 1$ although it ought to have a different numerical value than $\sqrt{3}$. In addition, it should become broader and flatter with increasing N_b. This is exactly what is seen in Figure 4.4, and it clearly and convincingly demonstrates the presence of the predicted blob regime.

It was found that $\alpha = 1.26$ and $\beta = 0.30$ by fitting the results of $N_b = 100$ to the predicted scalings for $\langle d_w \rangle$ and $\sqrt{\langle R_{g,w}^2 \rangle}$, respectively, in the blob regime.

4.7 Analysis of Global/Post Problem

With our results for the local problem in hand, we are now equipped to fully address the post problem shown in Figure 4.1A. We begin by determining the average tangential velocity of the molecule $\langle v_\theta \rangle$. We then use this result to develop a 1D Fokker-Planck equation to balance the effects of convection and diffusion along the post surface. From this, we calculate the mean escape time $\langle T_{esc} \rangle$ of a molecule as a function of its initial collision location θ_0. We compare all of our predictions against simulation results.

We also restrict our analysis to field strengths where the compressed chains are in the blob regime for the local problem. Clearly, depending on the strength of the applied field, we could develop different velocity predictions for each of the low field, high field and blob regimes. However, it seems sufficient to analyze only one of these, knowing that the same type of analysis should be applicable to the other two. We have chosen the blob regime because it seems to be the richest of the three.

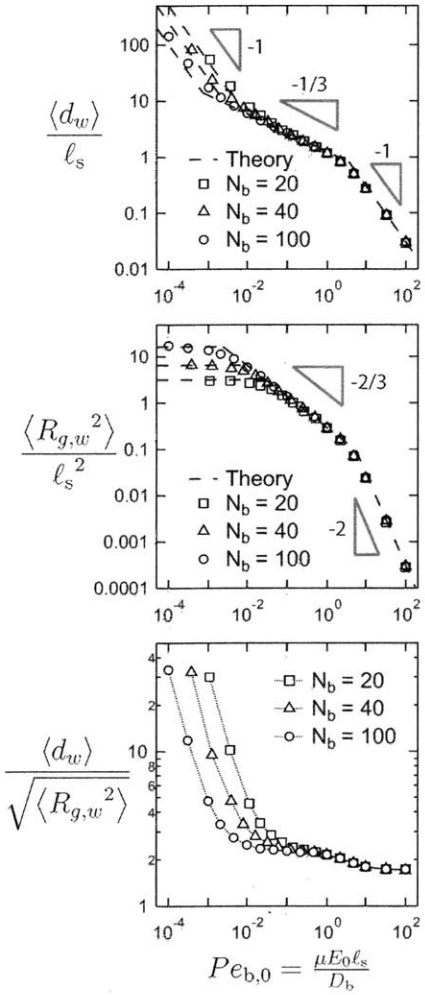

Fig. 4.4: *Plot of the average distance of the center of mass from a flat wall* $\langle d_w \rangle$ *for multibead chains in a uniform field versus the field strength along with the theoretical prediction given by Equation 4.22 (top). Plot of the radius of gyration squared of the chains in the direction transverse to the wall* $\langle R_{g,w}{}^2 \rangle$ *versus the field strength along with the theoretical prediction given by Equation 4.23 (middle). Plot of the ratio of* $\langle d_w \rangle$ *and* $\sqrt{\langle R_{g,w}{}^2 \rangle}$ *versus the field strength (bottom).*

4.7.1 Determination of $\langle v_\theta \rangle$

We have previously shown in Equation 4.6 that $\langle v_\theta \rangle \sim \langle d_p \rangle$. From the result in Equation 4.22 for the blob regime, we expect that

$$\langle d_p \rangle \approx \alpha \ell_s Pe_b[\mu E_r(\theta)]^{-1/3} \tag{4.24}$$

where $Pe_b[\mu E_r(\theta)]$ is the Péclet number based on the local value of $\mu E_r(\theta)$ which is given in Equation 4.5. Combining these results we arrive at

$$\frac{\langle d_p \rangle}{\ell_s} \approx \alpha \left(2Pe_{b,\infty} \cos\theta\right)^{-1/3}. \tag{4.25}$$

If we insert this expression into Equation 4.6, we find that

$$\frac{\langle v_\theta \rangle}{D_b/N_b R} \approx \alpha N_b \left(2Pe_{b,\infty}\right)^{2/3} \cos^{-1/3}\theta \sin\theta. \tag{4.26}$$

where we have nondimensionalzed the velocity based upon the post length scale R and the chain diffusion time scale $N_b R^2/D_b$. Based on this equation for the velocity, we can define a governing Péclet number for the post problem:

$$Pe_P = N_b \left(2Pe_{b,\infty}\right)^{2/3}. \tag{4.27}$$

In Figure 4.5, we compare the prediction for $\langle d_p \rangle$ versus $Pe_b(\theta)$ given in Equation 4.24 to the results from simulating the collisions of several different chain lengths at various values of Pe_P with a post of radius $R/\ell_s = 50$. Excellent agreement is seen, except for $Pe_P = 40$. This discrepancy at high Pe_P occurs because the smaller chain lengths ($N_b = 10$ and 20) have been pushed beyond the blob regime into the high field regime ($Pe_b \gg 1$) where Equation 4.24 is not applicable. These results confirm that our analysis of the local problem, particularly Equation 4.22, is correct even for the more complicated post problem. We also compare our predictions for $\langle v_\theta \rangle$ given in Equation 4.26 to the simulation data in Figure 4.6. We have nondimensionalized $\langle v_\theta \rangle$ by the predicted scaling $\alpha Pe_P D_b/N_b R$ to achieve universal collapse of all the curves. Our theoretical treatment matches the data except when blob theory breaks down for the smaller chains at large Pe_P.

The velocity $\langle v_\theta \rangle$ at the most upstream point on the post ($\theta = 0$) is zero, and initially, it increases nearly linearly with increasing θ. But $\langle v_\theta \rangle$ begins to rise rapidly as θ approaches $\pi/2$. This is due to a sharp decrease of $\mu E_r(\theta)$ near $\theta = \pi/2$ which causes the chain to quickly expand. This increase in $\langle d_p \rangle$ leads to greater exposure of the chain to the tangential electrophoretic velocity field and a rapid increase in the average molecular velocity $\langle v_\theta \rangle$. Our prediction for $\langle v_\theta \rangle$ given in Equation 4.26 actually diverges at $\theta = \pi/2$ which is clearly aphysical. This is because our model neglects several realities including that our linearization of μE_θ is not valid for large $\langle d_p \rangle$ and that the chain cannot expand instantaneously (i.e., separation of the radial and angular dynamics breaks down). However, our prediction is still very good over the entire domain except very near $\theta = \pi/2$.

Another problem with our model is that it predicts that a chain located at $\theta = 0$ will never escape from the post since $\langle v_\theta \rangle = 0$. In order to accurately predict the behavior of a chain near $\theta = 0$, we must incorporate diffusion into our model.

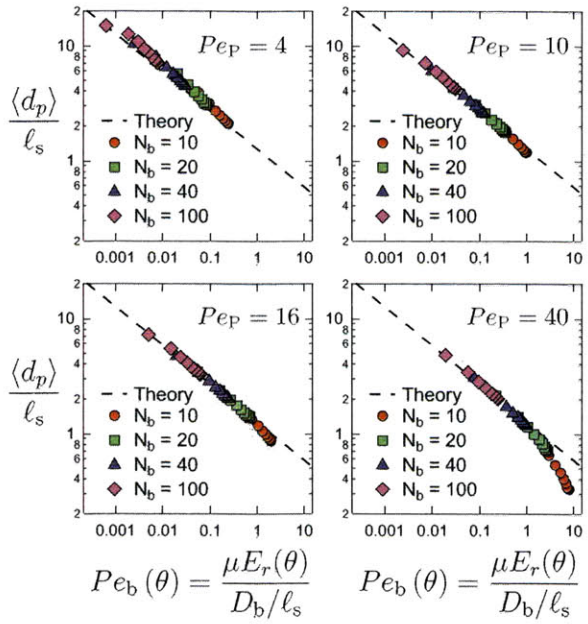

Fig. 4.5: *Plot of the average distance of the center of mass from the post surface* $\langle d_p \rangle$ *for multibead chains trapped against a conducting post versus the local transverse field strength* μE_r. *The fitted scaling from the flat wall studies is shown for comparison (Equation 4.24).*

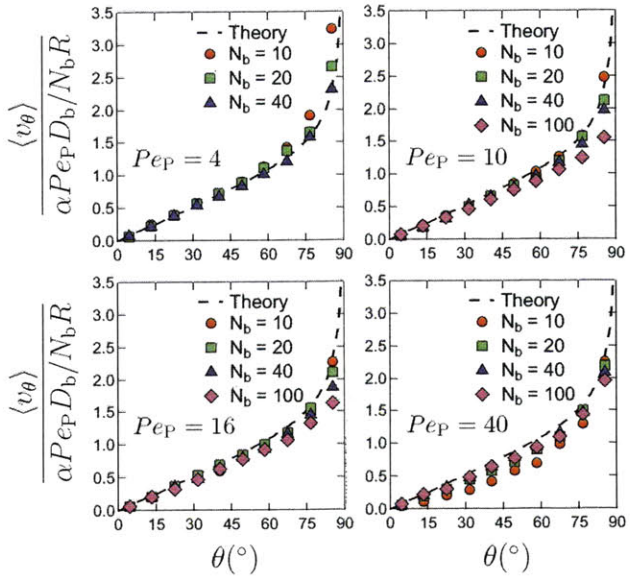

Fig. 4.6: *Plots of the average tangential velocity $\langle v_\theta \rangle$ of multibead chains trapped against a conducting post as a function of location on the post surface θ. The theoretical prediction given by Equation 4.26 is also plotted.*

4.7.2 Incorporating Diffusion

In order to include diffusion in our theory, we turn to a Fokker-Planck (FP) approach. We consider the post problem to be a time dependent 1D problem in the $\mathbf{e}_\theta$ direction with $r = R$. We develop a Fokker-Planck equation for a molecule with a diffusivity of $D = D_b/N_b$. If we assume the molecule is being transported in a velocity field $\langle v_\theta \rangle$, then we can write

$$\frac{\partial p}{\partial t} = \frac{D_b}{N_b} \frac{\partial^2 p}{\partial (R\theta)^2} - \frac{\partial}{\partial (R\theta)} \left(\langle v_\theta \rangle p \right) \tag{4.28}$$

where p is the probability density of finding a molecule at given time and location and $R\theta$ is the arclength. Due to the symmetry around the most upstream point of the post at $\theta = 0$, we restrict our analysis to the domain $0 \leq \theta \leq \pi/2$. We use our previously determined expression for $\langle v_\theta \rangle$ given in Equation 4.26. For tractability, we make the approximation $\cos^{-1/3}\theta \sin\theta \approx \theta$ which is very good over most of the domain. Finally, we nondimensionalize time based upon the diffusion time scale of the chain over the length scale of the post: $\tau = N_b R^2/D_b$. This leads to the nondimensional form of the FP equation:

$$\frac{\partial p}{\partial \tau} = \frac{\partial^2 p}{\partial \theta^2} - \alpha Pe_P \frac{\partial}{\partial \theta} (\theta p) \tag{4.29}$$

We use a reflecting boundary condition at $\theta = 0$ due to symmetry and an absorbing boundary condition at $\theta = \pi/2$ to signify the "escape" of the molecule:

$$\frac{\partial p}{\partial \theta}(\tau, \theta = 0) = p(\tau, \theta = \pi/2) = 0 \tag{4.30}$$

For the initial condition, we choose a unit impulse at θ_0 to model the initial collision location of a molecule at that location:

$$p(\tau = 0, \theta) = \delta(\theta - \theta_0) \tag{4.31}$$

This is the problem of a particle diffusing in an inverted harmonic potential, and interestingly, it has been considered before in DNA collisions with point obstacles [52, 119]. Although we cannot obtain a solution for $p(\tau, \theta)$, we can calculate the mean first passage time to $\theta = \pi/2$ of a particle that starts at $\theta = \theta_0$. This is exactly the average escape time of a molecule from the post surface $\langle T_{esc} \rangle$. The theory of first passage times [123] tells us that for this particular problem

$$\frac{\langle T_{esc} \rangle}{N_b R^2/D_b} = \int_{\theta_0}^{\pi/2} dx \exp\left(-\frac{\alpha Pe_P}{2} y^2\right) \int_0^x dy \exp\left(\frac{\alpha Pe_P}{2} x^2\right) \tag{4.32}$$

We can recast this expression in terms of Dawson's integral[124] $\left[D(x) = e^{-x^2} \int_0^x e^{y^2} dy\right]$:

$$\frac{\langle T_{esc} \rangle}{N_b R^2/D_b} = \sqrt{\frac{2}{\alpha Pe_P}} \int_{\theta_0}^{\pi/2} D\left(\sqrt{\frac{\alpha Pe_P}{2}} x\right) dx \tag{4.33}$$

Finally, the integral of $D(x)$ can be written in terms of generalized hypergeometric functions [124] $[{}_pF_q(a_1, \ldots, a_p; b_1, \ldots, b_q; z)]$:

$$\frac{\langle T_{esc} \rangle}{N_b R^2/D_b} = \frac{1}{2}\left[\frac{\pi^2}{4} {}_2F_2\left(1, 1; 3/2, 2; -\frac{\alpha Pe_P}{2}\frac{\pi^2}{4}\right) - \theta_0^2 {}_2F_2\left(1, 1; 3/2, 2; -\frac{\alpha Pe_P}{2}\theta_0^2\right)\right] \tag{4.34}$$

In Figure 4.7, we have plotted this prediction for $\langle T_{esc} \rangle$, nondimensionalized by the convective time scale $N_b R^2/\alpha Pe_P D_b$, for several values of Pe_P including for the purely convective case (i.e., $Pe_P = \infty$).

We expect that in the region of the domain dominated by convection the curve will collapse onto the result for pure convection, and indeed, this is what occurs for θ near $\pi/2$ where the velocity is the strongest. On the other hand, near $\theta = 0$ diffusion dominates, and the curve falls well below that of pure convection since diffusion is helping to speed up the escape process. It is also clear in Figure 4.7 that the location of this transition from the diffusive region to the convective region occurs at smaller and smaller values of θ as Pe_P increases. This is expected because a larger portion of the domain is dominated by convection at large values of Pe_P. Indeed, this increasingly small diffusive region near $\theta = 0$ forms a boundary layer for $Pe_P \gg 1$.

We can derive a scaling for the size of the region dominated by diffusion θ_{BL} by estimating where the convective and diffusive time scales are comparable. The convective time scale is $N_b R^2/\alpha Pe_P D_b$ while the diffusive time scale is $N_b(R\theta_{BL})^2/D_b$. Balancing these two gives the scaling $\theta_{BL} \sim Pe_P^{-1/2}$.

In order to confirm this scaling for θ_{BL}, we used the location of the intersection of $\langle T_{esc} \rangle$ for a finite Pe_P with the curve for the purely convective case as a measure of θ_{BL}. Figure 4.7 shows the

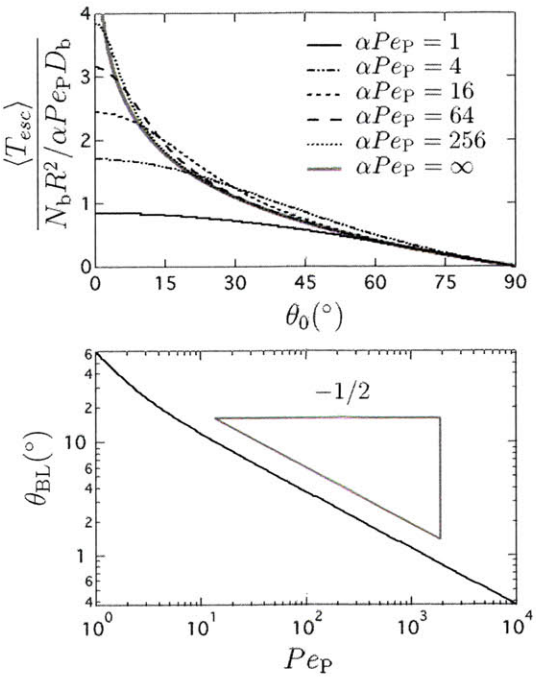

Fig. 4.7: *Plots of the average "escape" time* $\langle T_{esc} \rangle$ *predicted by Equation 4.34 for various values of* αPe_P*, including the purely convective case (i.e.,* $Pe_P = \infty$*) (top). Plot of the location of the intersection point* θ_{BL} *of* $\langle T_{esc} \rangle$ *for a given value of* Pe_P *with the purely convective case (bottom). The predicted scaling for* θ_{BL}*, which is a measure of the boundary layer size, is shown for comparison.*

results of this analysis. At high Pe_P, the predicted scaling is correct.

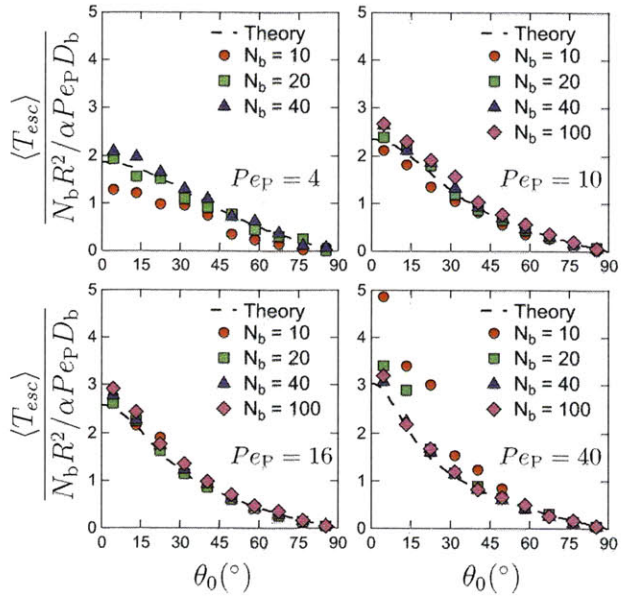

Fig. 4.8: *Plots of the average escape time $\langle T_{esc} \rangle$ of multibead chains as a function of where they are initially trapped by a conducting post θ_0. The theoretical prediction given by Equation 4.34 is also shown.*

The results for $\langle T_{esc} \rangle$ from our simulations are shown in Figure 4.8 where we have non-dimensionalized the escape time by the convective time scale. Good agreement is seen between the simulations and the predictions of Equation 4.34. The only notable exception is for $N_b = 10$ at $Pe_P = 40$ which is expected since the chain has been pushed well beyond the blob regime as previously shown. Our model clearly does a very good job of predicting the behavior of these chains.

4.8 Conclusion

We have examined the problem of electrophoretic collisions of DNA with large, ideally conducting posts, and we have identified and characterized the essential physics that govern the problem. We have purposefully simplified this problem in order to develop analytically solvable models and scaling theories that prove that the important physics are well-understood. In particular, we have studied the field-induced compression a molecule against the post surface and how it determines the velocity of the chain as it moves around the post. Although we have used the simple model of an ideal, Gaussian chain, we believe the basic physics and fundamental character of the problem have been captured. However, our approach allows for a more realistic molecular description. For example, excluded volume effects could easily be incorporated into our blob theory framework, and new scalings could be derived.

Also, by considering large posts, we have precluded all hooking phenomena. But in applications involving DNA separations, hooking and the subsequent unhooking process are typically the major reasons that length-dependent separation arises. However, our results can still be applied to examine the more realistic and complicated situation of moderately-sized, conducting posts where hooking should occur. For example, our prediction for the tangential velocity of a molecule (Equation 4.26) is nearly linear in θ which makes it look very similar to an elongational field. This suggests that for strong enough field gradients, molecules will stretch around the post. Such behavior would be important for understanding hook formation in these more realistic cases.

We believe that conducting posts could offer advantages over insulating posts due to the way they attract and directly interact with DNA molecules. Insulating and dielectrically-matched posts tend to quickly move molecules around their surfaces, and detrimental channeling is often seen in arrays of such posts [122]. The attractive nature of conducting posts might decrease the effects of channeling and enhance separation efficiency. Additionally, it could also lead to new modes of separation that have not yet been observed or predicted.

Currently, we know of no experimental studies that have looked at conducting posts, but we can imagine at least two different ways to achieve such a system. The first would be to use metal posts with biased AC fields. Because metal posts are impenetrable to ions, a DC field would simply polarize the surrounding double layer, and eventually, the field lines would resemble those of an insulating post. Using properly timed AC fields should prevent this polarization from occurring [125]. The second way would be to use a charged hydrogel that is impermeable to DNA. Unlike a metal post, a charged hydrogel would be permeable to small ions, and its higher conductivity than the bulk fluid would result in the desired field lines.

To end, we would like to provide estimates of some of the parameters and measurables that might be used or seen in a real experiment under reasonable conditions. For order of magnitude purposes, we assume that, for DNA in buffers typically used by our group [9] and others, the length and the diffusivity of a Kuhn segment are around $b_\mathrm{K} \approx 100$ nm and $D_\mathrm{K} \approx 20\ \mu\mathrm{m}^2/\mathrm{s}$, respectively, and that a typical value for the electrophoretic mobility is $\mu \approx 1.5\ \mu\mathrm{m/s}$. For T4-DNA, which has a contour length of $L \approx 70\ \mu\mathrm{m}$, a bulk radius of gyration of $R_g \approx 1.5\ \mu\mathrm{m}$, and a bulk diffusivity of $D \approx 1\ \mu\mathrm{m}^2/\mathrm{s}$, we estimate that the blob regime occurs at applied field strengths in the range of $E_\infty \approx 0.005 - 50$ V/cm. We obtain this estimate from Equation 4.22 by replacing the bead Péclet number Pe_b with the Péclet number based on a Kuhn step Pe_K. Using this range of field strengths, we can estimate the characteristic escape time T_{esc} for a particular post size using the convective time scale of the global post problem $R^2/\left(2Pe_{\mathrm{K},\infty}\right)^{2/3} D_\mathrm{K}$. However, we must also ensure that the convective time scale is faster than the diffusive time scale R^2/D which provides the upper limit for T_{esc}. Based on this calculation, we find that the convection-dominated blob regime occurs in the range of $E_\infty \approx 1 - 50$ V/cm. For a post size of $R = 5\ \mu\mathrm{m}$, the characteristic escape time would be $T_{esc} \approx 1$ s - 20 s. For a post size of $R = 15\ \mu\mathrm{m}$, this would increase to $T_{esc} \approx 10$ s - 3 min.

Acknowledgments

The authors thank the Singapore-MIT Alliance for Research and Technology (SMART) and the National Science Foundation grant CBET-0852235 for funding. Additionally, the authors would like to thank Jing Tang and Will Uspal for their many insightful discussions.

CHAPTER 5

Relaxation in Slitlike Confinement

Relaxation of polymers in confined environments has received a great deal of attention recently due to the emergence of micro- and nanofluidic devices which attempt to manipulate single molecules. More fundamentally, many naturally occurring polymeric molecules exist in highly confined cellular environments. While there has been much previous work on the bulk relaxation of polymers, there has been relatively little work considering the confined case. In this chapter, we consider the relaxation of an initially stretched DNA molecule in slitlike confinement. We report the first observance using simulations of two distinct relaxation times in the linear force regime. We also conclusively show that the emergence of the second relaxation time is due to excluded volume effects. Finally, we assess the validity of a previously proposed mechanistic model confined relaxation. Our results are important for the design and optimization of devices that attempt to use confinement to modulate the dynamic properties of DNA molecules.

5.1 Overview

Brownian dynamics simulations of bead-spring chains were used to study the relaxation of an initially stretched DNA molecule in slitlike confinement. Taking into account excluded volume effects but neglecting hydrodynamic interactions, the simulations are able to reproduce the two relaxation times in the linear force regime that our group has experimentally studied and recently reported. The relaxation dynamics of the transverse dimensions are extensively studied, and a theoretical model is developed to describe them. The interplay between the longitudinal and transverse dynamics is investigated and used to corroborate a physical model previously proposed to describe polymer relaxation in a slit.

5.2 Introduction

5.2.1 Motivation

The emergence of micro- and nanofluidic devices has led to many new and exciting developments in the field of single-molecule manipulations. For example, DNA separations [57, 15] and genomic mapping [2, 118] have benefited greatly from the precise control offered by so-called "lab-on-a-chip" devices. More generally, these microscopic systems have provided an important new platform to study fundamental problems in polymer physics [36, 30, 17, 105, 126, 31, 32].

One recent problem that has received a considerable amount of attention, is the relaxation dynamics of DNA in different types of confined environments [30, 127, 128, 31]. This is particularly important for many single-molecule mapping devices that rely upon collisions [97] and field gradients [2, 97] to deform DNA for subsequent analysis. This deformation process is highly dependent upon the balance between the stretching rate of the device and the relaxation of the polymer. Therefore, understanding how confinement affects the relaxation process of confined polymers is critical both to optimizing current technologies and to developing novel device designs.

Additionally, many important biological molecules are polymeric in nature (e.g., DNA, actin, and microtubules), and most cellular environments are highly confined. For example, 3 m of human DNA is packed into a nucleus of around 5 μm in diameter. Study of the dynamics of confined DNA molecules is critical to understanding how the cell stores, accesses, and replicates it's genetic information. In vivo relaxation of chromosomal DNA has even been used to probe the intracellular environment [129].

5.2.2 Past Work

Over the last two decades, the relaxation of unconfined polymers has been studied comprehensively both experimentally [36] and via simulations [130, 131, 132]. They have confirmed the theoretical prediction that single molecule relaxation in bulk is well-described by a single longest relaxation time τ_1 over all extensions within the chain's linear force regime [133] (from equilibrium to $\sim 30\%$ fractional extension [36]). However, relaxation in slitlike confinement has been studied much less extensively, with several studies offering contradictory findings [134, 30, 135, 136, 71, 128]. It is only recently that these results have begun to be reconciled by suggesting the existence of two relaxation times in the linear force regime [31].

The dynamics of polymers in slitlike confinement were first treated theoretically by Brochard [28] using blob theory. The first direct observation of such confined relaxation, by Bakajin and coworkers

[30], was of molecules relaxing after having been highly stretched by collisions with microfabricated posts. The results produced scalings for the relaxation time that were more in line with those in bulk [31]. Nearly a decade later, new experiments from our group obtained the confined relaxation time by measuring the rotational autocorrelation function of chains at equilibrium [128]. This study found good agreement with the blob theory predictions, contradicting the previous work of Bakajin et al. [30] Interestingly, several simulation studies found evidence to support the findings of both of the aforementioned experimental works. Simulating the relaxation of initially stretched chains [136, 71] reproduced the bulklike results of Bakajin et al. [30], while Monte Carlo simulations of chains at equilibrium [134, 135] corroborated the blob theory scalings seen by our group [128].

Although seemingly contradictory, taken together these studies hint at the cause of the discrepancies. All the work where chains were perturbed from equilibrium agree with each other and demonstrate bulklike behavior. On the other hand, agreement was also seen amongst the studies of chains at equilibrium which exhibited blob scalings. To explain this, our group suggested that two distinct relaxation times existed in the linear force regime [31]. When the molecule is stretched, the width of the chain in the transverse dimension is smaller that the height of the channel, and the confining walls do not significantly affect the conformation of the molecule. Therefore, the chain is governed by a bulklike relaxation time τ_I. However, at or near equilibrium, the polymer feels the full steric effects of the confining walls, and its dynamics slow as a consequence. A second relaxation time τ_{II} emerges which is longer than τ_I and which follows the predictions of blob theory.

Our group has shown that both of these relaxation times can be seen and measured by observing the longitudinal relaxation of initially stretched molecules over time scales long enough for the chain to reach equilibrium [31, 137]. A physical model based upon blob theory has also been proposed that assumes this extension-dependence of the relaxation time is due entirely to excluded volume effects (EV) and not hydrodynamic interactions (HI). Although there is some experimental evidence that this model is correct, experiments are greatly hampered by the fact that the dynamics cannot be accurately measured on small time and length scales, especially in the dimension transverse to the plane of the channel.

5.2.3 Problem Statement

In this chapter, we study the relaxation of a bead-spring chain in slitlike confinement from a stretched configuration that is initially straight using a combination of simulations and theory. Since simulations allow us to set which physics will be included, we can conclusively determine if excluded volume effects are sufficient to reproduce the qualitative features observed in experiments (e.g., two relaxation times). In addition, simulations can probe dynamics of the relaxation process on length and time scales that are inaccessible to experiments, particularly in the confined dimension. This allows us to consider the interplay between the dynamics in the direction of initial stretch and the confined dimension, enabling us to assess the validity of the current physical model for confined relaxation and its underlying assumptions.

5.3 Background

We now describe the theory of polymer relaxation both in bulk and slitlike confinement. We start by considering the equilibrium size of a polymer chain and the basics of blob theory. We then use these results to develop scalings for the relaxation times of these chains. We also explain the

current physical model of relaxation in slitlike confinement and some of its consequences.

In particular, we concern ourselves with the expected theoretical scalings based upon the physics included in our simulations. Therefore, we take EV into account, but we neglect the effects of HI. The chains are assumed to be free-draining so that

$$\zeta = N_{\mathrm{K}}\zeta_{\mathrm{K}}. \tag{5.1}$$

Additionally, HI with the channel walls is neglected, and changes in the chain diffusivity due to confinement are ignored.

5.3.1 Equilibrium Chain Size

The polymer is modeled as a chain composed of N_{K} Kuhn steps each of length b_{K}. In bulk, the equilibrium radius of gyration $R_{g,0}$ of the chain can be determined from the statistics of random walks

$$\frac{R_{g,0}}{b_{\mathrm{K}}} \sim {N_{\mathrm{K}}}^{\nu_{3\mathrm{D}}}, \tag{5.2}$$

where $\nu_{3\mathrm{D}}$ is the scaling exponent for the equilibrium chain size in a 3D environment. If the chain is ideal and intramolecular excluded volume effects are neglected, then $\nu_{3\mathrm{D}} = 1/2$. The inclusion of EV causes the chain to swell and increases the scaling exponent to $\nu_{3\mathrm{D}} \approx 3/5$.

In slit-like confinement, the polymer is squashed like a pancake, and due to EV, it swells in size even further. Blob theory is often used to describe confined polymers [29]. In this framework, the polymer is represented by a string of N_{K}/g blobs, where g is the number of Kuhn segments per blob (see Figure 5.1). The size of a blob is set by the height of the channel, h.

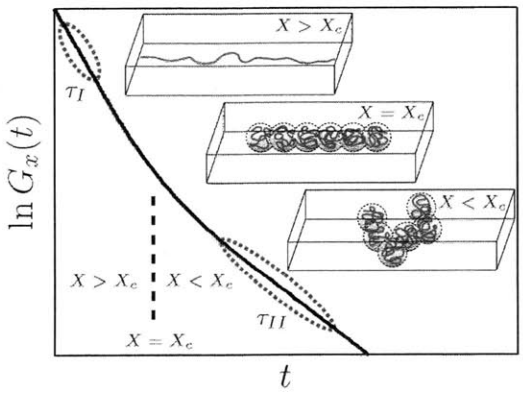

Fig. 5.1: *A cartoon depicting the physical model of confined relaxation based upon tensions-blobs and how it relates to the longitudinal relaxation function $G_x(t)$. Above a certain crossover extension X_c, the chain is not sterically confined and relaxes as if it were in bulk. Below X_c, the confining walls become important, and the chain relaxes by rearranging its self-avoiding blobs.*

On length scales smaller than h (i.e., within a blob), the polymer retains its bulk-like behavior.

So using Equation 5.2, we can say that $h \sim g^{\nu_{3D}} b_K$, and upon rearrangement, the number of Kuhn segments g in a blob is given by

$$g \sim \left(\frac{h}{b_K}\right)^{1/\nu_{3D}}. \tag{5.3}$$

On scales larger than h, the blobs, which repel each other due to EV, obey the scalings of a 2D self-avoiding walk (2D-SAW). So in slitlike confinement, the size of the chain is given by

$$\frac{R_{g,0}}{b_K} \sim \left(\frac{N_K}{g}\right)^{\nu_{2D}} \frac{h}{b_K} \sim {N_K}^{\nu_{2D}} \left(\frac{h}{b_K}\right)^{1-\nu_{2D}/\nu_{3D}}, \tag{5.4}$$

where $\nu_{2D} = 3/4$.

5.3.2 *Relaxation Times*

Bulk

First, we consider the relaxation of a linear polymer in the bulk. The longest relaxation time of the chain can be derived by considering a force balance between the elastic spring force F_E of the chain and the drag force F_D that opposes it. The force required to stretch a chain away from its equilibrium size $R_{g,0}$ by an amount δR_g is given by

$$F_E \approx -\frac{k_B T}{{R_{g,0}}^2} \delta R_g, \tag{5.5}$$

where k_B is the Boltzmann constant and T is the temperature. The drag force felt by the chain is

$$F_D \approx -\zeta \delta \dot{R}_g, \tag{5.6}$$

where $\dot{R}_g$ is the rate of change of the size of the chain. Balancing these forces gives the longest relaxation time τ_I for the chain

$$\tau_I \approx -\frac{\delta R_g}{\delta \dot{R}_g} \approx \frac{\zeta {R_{g,0}}^2}{k_B T}. \tag{5.7}$$

Introducing the results from Equations 5.1 and 5.2 and noting that $\zeta_K = k_B T / D_K$, we arrive at

$$\frac{\tau_I}{{b_K}^2 / D_K} \sim {N_K}^{1+2\nu_{3D}}, \tag{5.8}$$

where D_K is the diffusivity of a Kuhn segment.

Slitlike Confinement

When a molecule in a slit is stretched strongly enough, it is not sterically confined by the walls of the channel (see Figure 5.1). Therefore, the initial relaxation process is unaffected by the presence of the confining walls, and the molecule relaxes with the bulklike time constant τ_I given by Equation 5.8. However, as the molecule relaxes, its lateral dimensions grow in size, and the confining effects of the wall become significant. This slows down the relaxation process, and a new, longer relaxation time τ_{II} emerges that governs the remaining relaxation to equilibrium.

A simple physical model based upon a quasi-steady tension-blob framework was proposed by Balducci and coworkers [31] to describe the transition between these two relaxation times. The stretched molecule can be represented by a string of N_K/g tension-blobs [68] of size ξ, where g is again the number of Kuhn segments per blob. Bulk scalings hold within each blob so $g \sim (\xi/b_K)^{1/\nu_{3D}}$. The fractional extension of the chain X is then given by $X = \xi/gb_K \sim (\xi/b_K)^{1-1/\nu_{3D}}$. If the crossover from τ_I to τ_{II} occurs when the tension-blob size reaches the height of the channel (i.e., $\xi = h$), then the critical fractional extension X_c at which this crossover occurs is given by

$$X_c \sim (h/b_K)^{1-1/\nu_{3D}}. \tag{5.9}$$

Above X_c, the molecule relaxes by growing the size of the tension-blobs. But below X_c, tension-blob growth is restricted by the confining walls, and the molecule relaxes by rearranging the blobs. An interesting consequence of this model is that X_c is independent of chain length.

In order to determine τ_{II}, we employ Equation 5.7 which is valid near equilibrium. We simply use the blob scalings for $R_{g,0}$ as given in Equation 5.4. At or near equilibrium, the relaxation time of a confined molecule is given by

$$\frac{\tau_{II}}{{b_K}^2/D_K} \sim {N_K}^{1+2\nu_{2D}} \left(\frac{h}{b_K}\right)^{2(1-\nu_{2D}/\nu_{3D})}. \tag{5.10}$$

5.4 Simulation Method

We simulated the relaxation of DNA using a model developed by Kim and Doyle [100]. This method is based upon Brownian Dynamics and is well-suited for studying the dynamics of DNA in microfludic devices. A brief description of the numerical model is presented here.

5.4.1 Brownian Dynamics

DNA molecules are modeled as chains of N_b beads connected by $N_s = (N_b - 1)$ springs. The equation of motion for the position $\boldsymbol{r}_i$ of the ith bead is:

$$\frac{d\boldsymbol{r}_i}{dt} = \frac{1}{\zeta_b}\left[\boldsymbol{F}_i^{\mathrm{B}}(t) + \boldsymbol{F}_i^{\mathrm{S}}(t) + \boldsymbol{F}_i^{\mathrm{EV}}(t) + \boldsymbol{F}_i^{\mathrm{EV,wall}}(t)\right], \tag{5.11}$$

where ζ_b is the bead drag coefficient, $\boldsymbol{F}_i^{\mathrm{B}}$ is the Brownian force, $\boldsymbol{F}_i^{\mathrm{S}}$ is the total spring force felt by the bead, $\boldsymbol{F}_i^{\mathrm{EV}}$ is the intrachain excluded volume force due to nearby beads, and $\boldsymbol{F}_i^{\mathrm{EV,wall}}$ represents the interaction of the bead with the wall of the device.

We non-dimensionalize the variables as follows:

$$\hat{\boldsymbol{r}} \equiv \frac{\boldsymbol{r}}{l_s},\ \hat{t} \equiv \frac{t}{\zeta_b {l_s}^2/k_{\mathrm{B}}T}, \tag{5.12}$$

where $\boldsymbol{r}$ is position, l_s is the maximum extension of a single spring ($l_s \equiv L/N_s$), t is time, k_{B} is Boltzmann's constant, and T is the absolute temperature. We non-dimensionalize the forces $\boldsymbol{F}$ as follows:

$$\hat{\boldsymbol{F}}(\hat{\boldsymbol{r}}) \equiv \frac{\boldsymbol{F}}{k_{\mathrm{B}}T/l_s}. \tag{5.13}$$

This leads to the non-dimensional form of Equation (5.11):

$$\frac{d\hat{\boldsymbol{r}}_i}{d\hat{t}} = \hat{\boldsymbol{F}}_i^{\mathrm{B}} + \hat{\boldsymbol{F}}_i^{\mathrm{S}} + \hat{\boldsymbol{F}}_i^{\mathrm{EV}} + \hat{\boldsymbol{F}}_i^{\mathrm{EV,wall}}, \tag{5.14}$$

The non-dimensional Brownian force is given by:

$$\hat{\boldsymbol{F}}_i^{\mathrm{B}} = \sqrt{\frac{24}{\Delta\hat{t}}}\,(\boldsymbol{r}_n)_i\,, \tag{5.15}$$

where $\Delta\hat{t}$ is the dimensionless time step and $(\boldsymbol{r}_n)_i$ are uniform random numbers such that each component $(\boldsymbol{r}_n)_i^j \in [-1/2, 1/2]$, where j denotes the coordinate x, y, or z. The net non-dimensional spring force on the ith bead is:

$$\hat{\boldsymbol{F}}_i^{\mathrm{S}} = \begin{cases} \hat{\boldsymbol{f}}_{i,2}^{\mathrm{s}}, & i = 1; \\ \hat{\boldsymbol{f}}_{i,i+1}^{\mathrm{s}} + \hat{\boldsymbol{f}}_{i,i-1}^{\mathrm{s}}, & 1 < i < N_{\mathrm{b}}; \\ \hat{\boldsymbol{f}}_{i,N_{\mathrm{b}}-1}^{\mathrm{s}}, & i = N_{\mathrm{b}}; \end{cases} \tag{5.16}$$

where the spring force $\hat{\boldsymbol{f}}_{i,j}^{\mathrm{s}}$ is given by a spring law developed by Underhill and Doyle [69] to correctly reproduce the Marko-Siggia spring force law for a wormlike chain [33] at varying degrees of coarse-graining [59]:

$$\hat{\boldsymbol{f}}_{i,j}^{\mathrm{s}} = \upsilon \left[\frac{1}{\left(1 - \hat{r}_{j,i}^2\right)^2} - \frac{7}{\upsilon\left(1 - \hat{r}_{j,i}^2\right)} + C + B\left(1 - \hat{r}_{j,i}^2\right) \right] \hat{\boldsymbol{r}}_j - \hat{\boldsymbol{r}}_i, \tag{5.17}$$

where υ is the number of persistence lengths represented by each spring ($\upsilon \equiv l_s/A_p$), $\hat{r}_{j,i}$ represents the distance between $\hat{\boldsymbol{r}}_j$ and $\hat{\boldsymbol{r}}_i$, $C = 3/32 - 3/4\upsilon - 6/\upsilon^2$, and $B = \left(13/32 + 0.8172/\upsilon - 14.79/\upsilon^2\right) / \left(1 - 4.225/\upsilon +\right.$ The intrachain excluded volume force $\hat{\boldsymbol{F}}_i^{\mathrm{EV}}$ is modeled with the soft potential used by Jendrejack et al.: [82]

$$\hat{\boldsymbol{F}}_i^{\mathrm{EV}} = -\sum_{j=1(j\neq i)}^{N_{\mathrm{b}}} \frac{9}{2}\hat{\nu}^{\mathrm{ev,p}} \left(\frac{3}{4\sqrt{\pi}}\right)^3 \upsilon^{9/2} \exp\left[-\frac{9}{4}\upsilon\hat{r}_{i,j}^2\right] \hat{\boldsymbol{r}}_{j,i}, \tag{5.18}$$

where $\hat{\nu}^{\mathrm{ev,p}} \equiv \nu^{\mathrm{ev,p}}/{l_s}^3$ is the dimensionless form of the excluded volume parameter $\nu^{\mathrm{ev,p}}$.

The interactions between a bead and the walls represented by $\hat{\boldsymbol{F}}_i^{\mathrm{EV,wall}}$ are resolved using a modified Heyes-Melrose algorithm. [110, 100] Whenever a bead moves outside the domain during a time step, it is moved to the nearest point on the domain boundary before commencing the next time step:

$$\Delta\hat{\boldsymbol{r}}_i^{\mathrm{HM}} = \Delta\boldsymbol{p}_i H\left(\Delta p_i\right), \tag{5.19}$$

where $\Delta\hat{\boldsymbol{r}}_i^{\mathrm{HM}}$ is the displacement vector due to the Heyes-Melrose algorithm, $\Delta\boldsymbol{p}_i$ is the vector pointing from the bead outside the domain to the nearest boundary point, and the Heaviside step function $H\left(\Delta p_i\right)$ restricts the application of the algorithm to only the beads that have penetrated the domain boundaries.

5.4.2 Parameters

Many different lengths of DNA were simulated in this study, ranging from $N_s = 10$ to $N_s = 300$. The chosen discretization of DNA was $\upsilon = 5.571$, which, assuming a persistence length of $A_p = 53$ nm, corresponds to DNA contour lengths of $L \approx 3 - 90$ μm. The excluded volume parameter was set to $\nu^{\mathrm{ev,p}} = 3.71 \times 10^{-4}$ μm^3 in order to accurately reproduce the bulk radius of gyration of a T4-DNA molecule ($N_s = 254$ and $L = 75$ μm).

For the relaxation of initially extended molecules, the chains were uniformly stretched to the desired fractional extension (typically $X = 75\%$) along the x-direction and placed in the center of a 300 nm slit where the z-direction was transverse to the plane of the channel. The chains were then allowed to relax, and their configurations were saved for later analysis. Two different time steps were used. To obtain the short time behavior, a time step of $\Delta\hat{t} = 2 \times 10^{-5}$ was employed, and the chains were observed for a time of $\approx \tau_{II}$. For the long time behavior, a time step of $\Delta\hat{t} = 5 \times 10^{-4}$ was used, and the chains run for $\approx 10\tau_{II}$. For all measurements, at least 100 individual chains were simulated and averaged together for each chain length.

The equilibrium properties were obtained by initially placing the chains in the channel in a Gaussian manner and allowing them to equilibrate for $\approx 50\tau_{II}$. Configurations were then saved at specified time intervals for subsequent analysis. At least $\approx 300\tau_{II}$ worth of data was obtained.

5.5 Results

Before we begin analyzing the relaxation dynamics of confined chains, we would like to ascertain that we are using chains of adequate length for blob theory scalings to be valid. To do this, we look at the 2D, in-plane radius of gyration $R_{g,2D}$ of the chains at equilibrium. These results are shown in Figure 5.2 along with the predicted scaling of $R_{g,2D} \sim {N_s}^{3/4}$. It is clear that blob theory scalings are valid for chains with $N_s \geq 75$, and in our future analysis, we often only present results for these chain lengths.

In our study of the relaxation dynamics of confined chains, we first consider experimentally accessible measurables such as the relaxation of the longitudinal stretch at long times both at equilibrium and when initially perturbed away from equilibrium. This allows us to compare our findings to experimental results and validate our simulation model. We then look at the relaxation process in the transverse dimensions and attempt to build simple models based on Rouse-like chains to describe the observed dynamics. Finally, we consider how adding in additional physics, like intramolecular excluded volume and nonlinear springs, affects the relaxation dynamics.

5.5.1 Experimental Measurables

Typical measurables that are experimentally accessible are usually restricted to those involving the in-plane stretch of the molecule's major axis. We start by looking at the scaled longitudinal relaxation function $G_x(t) = \langle X(t)^2 \rangle - \langle {X_{\mathrm{eq}}}^2 \rangle$, where $X(t)$ is the fractional extension in the longitudinal direction and X_{eq} is its average equilibrium value. Figure 5.3A shows a characteristic curve for $G_x(t)$ when the number of springs is $N_s = 164$. As seen in experiments, there are two distinct regions that are well-approximated by a single decaying exponential, each with a different time constant. The first region, with time constant τ_I, occurs at fractional extensions near $X = 30\%$ and represents the bulk-like relaxation process where the chain is not sterically constrained. The second region occurs very near the chain's equilibrium size and, in agreement with experiments,

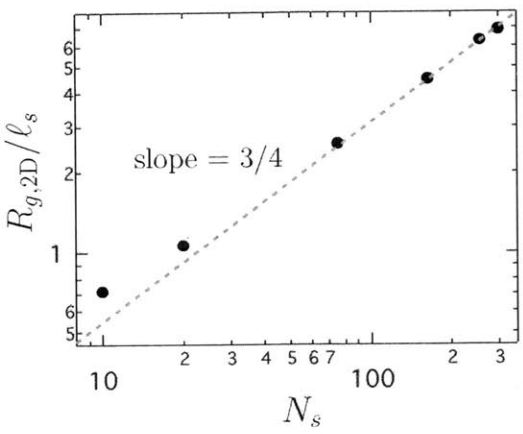

Fig. 5.2: *Plot of the 2D, in-plane radius of gyration $R_{g,2D}$ of chains at equilibrium in a 300 nm channel vs. the chain length N_s. The predicted blob theory scaling $R_{g,2D} \sim {N_s}^{3/4}$ is also shown.*

has a longer time constant τ_{II} than the bulk-like relaxation time ($\tau_{II} > \tau_I$). This second linear relaxation process is governed by the rearrangement of the blobs that compose the sterically confined chain. Finally, these two linear relaxation periods are connected by a nonlinear transition region.

In Figure 5.3C, we have plotted both τ_I and τ_{II} as a function of chain length along with their predicted blob theory scalings. The simulation results for τ_{II} clearly follow the predicted scaling of $\tau_{II} \sim {N_s}^{2.5}$ while the results for τ_I appear to fall slightly below the theoretical scaling of $\tau_I \sim {N_s}^{2.2}$. The apparent discrepancy between the simulations and theory for τ_I is not unexpected and can be explained by noting that when Equation 5.18 is used to account for EV, moderately extended chains are only mildly affected by the EV force. Because the bulk-like relaxation time τ_I is seen near fractional extensions of $X \approx 30\%$, EV effects are not as significant as they are near the equilibrium extension. Therefore, the observed scaling for τ_I falls somewhere between the ideal chain scaling of $\sim {N_s}^2$ and the real chain scaling of $\sim {N_s}^{2.2}$.

Experiments have shown that relaxation processes measured when a confined molecule is at equilibrium should correspond to the second relaxation region where steric confinement is important. In order to confirm that our simulations can reproduce this finding, we considered the conformational relaxation time of a chain at equilibrium τ_c. The conformational autocorrelation functions $C_c(\delta t)$ for several different chain lengths are shown in Figure 5.3B along with their respective linear fittings, and the measured conformational relaxation times τ_c are plotted in Figure 5.3C. τ_c is very near the value of τ_{II} and follows the same predicted scaling $\tau_c \sim \tau_{II} \sim {N_s}^{2.5}$, in agreement with experiments.

We have clearly shown that our simulation model can reproduce the qualitative features seen in experiments. These include two distinct linear relaxation times for $G_x(t)$ with $\tau_{II} > \tau_I$, the proper scaling for τ_{II} with chain length, very near the predicted scaling for τ_I, and finally that near-equilibrium relaxation processes are associated with τ_{II} as demonstrated by the fact that $\tau_c \sim \tau_{II}$.

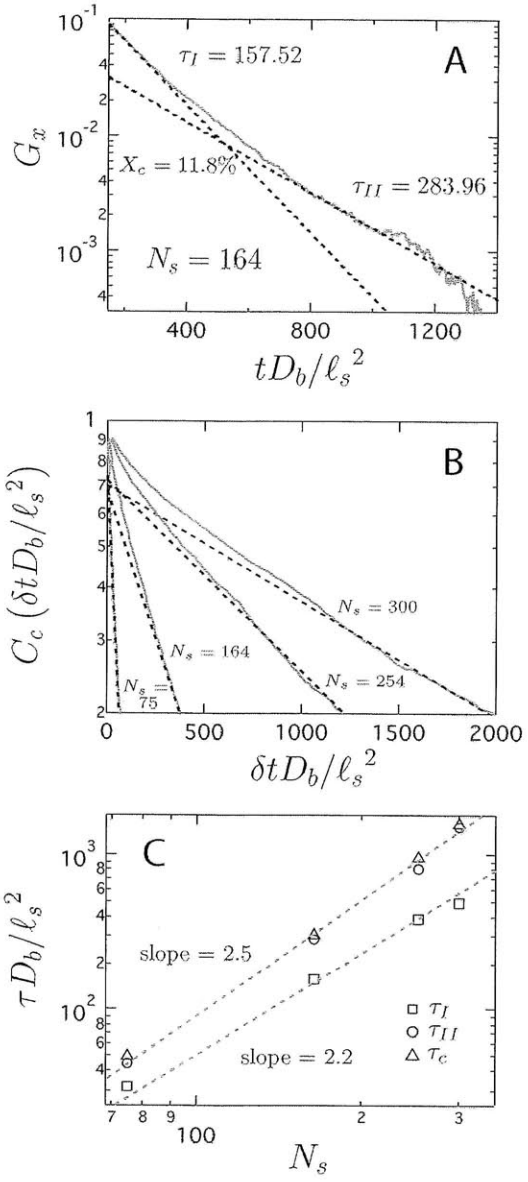

Fig. 5.3: *(A) Characteristic plot of the scaled longitudinal relaxation function* $G_x(t) = \langle X(t)^2 \rangle - \langle {X_{\text{eq}}}^2 \rangle$ *for chain length* $N_s = 164$. *The fittings for the two linear regions are also shown along with their respective time constants* (τ_I *and* τ_{II}) *and the predicted crossover extension* X_c. *(B) Plot of the equilibrium conformational autocorrelation function* $C_c(\delta t)$ *vs. the lag time* δt *for several chain lengths* ($N_s = 75, 164, 254, 300$). *The linear fittings for each curve are also shown. (C) Plot of various measured relaxation times vs. chain length* N_s. *Included are the bulk-like relaxation time* τ_I, *the near-equilibrium relaxation time* τ_{II}, *and the conformational relaxation time* τ_c. *Also shown are the predicted scalings* $\tau_I \sim {N_s}^{2.2}$ *and* $\tau_{II} \sim \tau_c \sim {N_s}^{2.5}$.

One final experimentally accessible measurement we obtained is the time t_{cross} at which the crossover extension occurs. This is defined as the time where the two linear fittings for $G_x(t)$ intersect (see Figure 5.3A). Although t_{cross} can be found from experiments, to date this analysis has not been performed. t_{cross} is a measure of the when the transition between bulk-like relaxation and near-equilibrium, sterically confined relaxation occurs. Based upon the current mechanisitic model of confined relaxation, the approach to this transition should be driven by the bulk-like relaxation process leading up to it. Therefore, it is expected that t_{cross} should scale as $t_{\text{cross}} \sim \tau_I \sim {N_s}^{2.2}$. Indeed, this is clearly seen in Figure 5.4.

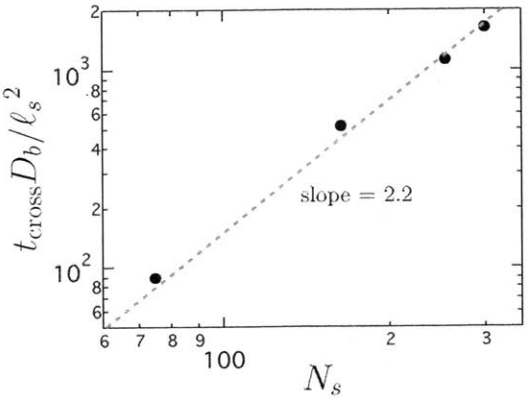

Fig. 5.4: *Plot of the computed crossover time t_{cross} vs. chain length N_s. Also shown is the predicted scaling $t_{\text{cross}} \sim {N_s}^{2.2}$.*

5.5.2 Transverse Dynamics

We now turn to the relaxation dynamics in the two transverse directions (y and z) which cannot currently be determined by experiments. Studying the of the out-of-plane behavior of these chains is particularly important because it can shed light on the physics of relaxation in confinement and help assess the validity of the current physical model.

General Features and Characteristics

We measured the 1D radius of gyration squared ${R_{g,i}}^2$ in the direction of each of the three coordinates (i can be either x, y, or z). Characteristic relaxation curves for all ${R_{g,i}}^2$, both in bulk and in a 300 nm channel, are shown in Figure 5.5A for a single chain length $N_s = 75$. In the longitudinal, or x-direction, ${R_{g,x}}^2$ remains fairly constant and slowly relaxes to its equilibrium value in an exponential manner only at long times. The behavior for the transverse directions is richer. In the case of relaxation in the bulk, ${R_{g,y}}^2$ and ${R_{g,z}}^2$ are equivalent, and two power law regimes are seen as they approach their equilibrium values. The first regime is linear in time while the second appears to follow a scaling close to $\sim t^{1/2}$. We will derive these scalings for a Rouse chain shortly. In bulk, all three directions are equivalent at equilibrium so that ${R_{g,x}}^2 = {R_{g,y}}^2 = {R_{g,z}}^2 = {R_{g,0}}^2/3$, and this is clearly seen in Figure 5.5A.

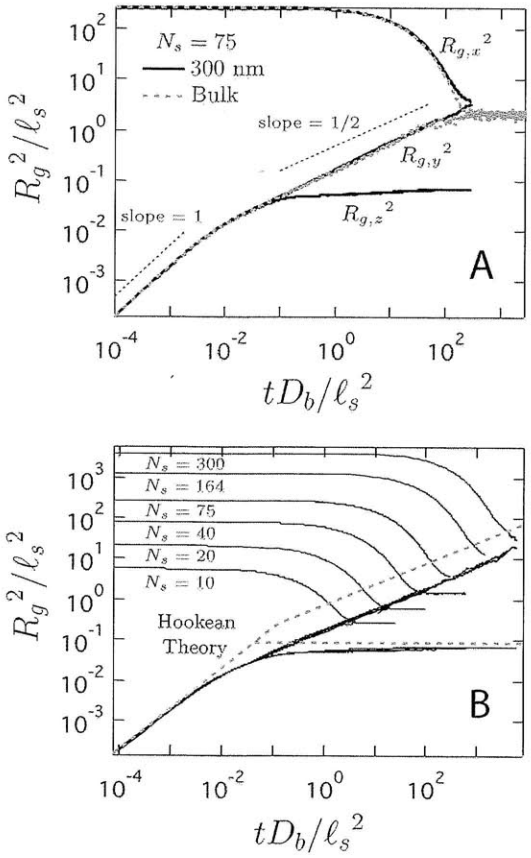

Fig. 5.5: *(A) Plot of the 1D radius of gyration squared in all three directions for a single chain length ($N_s = 75$) both in bulk and in a 300 nm channel. The observed power law regions and their approximate scalings with time are also shown. (B) Plot of the 1D radius of gyration squared in all three directions for several chain lengths in a 300 nm channel. Also shown are the predicted values for each of the power law regimes as determined from the Hookean, Rouse-like theory given in Equation 5.41.*

When the chain is placed in a slit, much of the relaxation process is similar to the bulk case. For example, ${R_{g,x}}^2$ still decays exponentially at long times, albeit with an increased time constant and to a slightly higher equilibrium value. ${R_{g,y}}^2$ and ${R_{g,z}}^2$, initially, are quantitatively equivalent to their bulk counterparts. However, at some point, the size of the chain in the confined dimension ${R_{g,z}}^2$ peels off from the bulk curve and quickly approaches a new and reduced equilibrium value. In the unconfined, transverse direction, ${R_{g,y}}^2$ continues to follow the bulk curve even after ${R_{g,z}}^2$ has deviated from the bulk behavior. ${R_{g,y}}^2$ follows this behavior until it reaches its new, slightly increased equilibrium value so that at long times ${R_{g,y}}^2 = {R_{g,x}}^2$.

Now that we have commented on the general features of the relaxation for a single chain, we look at the effect of chain length on the relaxation dynamics. In Figure 5.5B, we show the three 1D radii of gyration squared for several different chain lengths. As expected, ${R_{g,x}}^2$ is highly length dependent since its initial value is proportional to the chain length squared. Additionally, the relaxation times for the exponential decay and the final equilibrium values of ${R_{g,x}}^2$ are length dependent and have already been studied in Section 5.5.1. On the other hand, the relaxation of the two transverse dimensions appears to change little based upon the length of the chain. ${R_{g,z}}^2$ nearly falls on a universal curve for all time and chain lengths, with only slight deviations which will be discussed later. ${R_{g,y}}^2$ also falls on a universal curve until it nears its equilibrium value, at which point it stops growing and plateaus at its length dependent final size.

Now that we have identified the general features of the relaxation process in the transverse dimensions, we turn to understanding the mechanisms behind the observed behavior. In particular, we would like to identify the important physics governing each of the observed power law regimes. And with this in hand, we can study how the dynamics in the confined dimension affect, and are affected by, the longitudinal stretch.

Unconfined, Ideal Hookean Chain

Before we consider the relaxation dynamics in the confined dimension, we will look at the much simpler case of the transverse relaxation of an unconfined, Hookean chain. Because all three directions act independently for a linear chain, we only need to consider a 1D bead-spring chain with N_s springs each with a Hookean spring constant of H_s. Initially, the chain starts with all of the beads at the same point or, alternatively, with all of the springs having an initial stretch of zero. In this case, three different regimes arise during the relaxation process. We start by considering each of these from a scaling perspective and then use a continuous 1D Rouse model to prove some of our scalings and develop more quantitative expressions for the chain's size as a function of time.

At very short times, the bead movement is dominated by thermal forces. The springs are not yet extended enough to exert any significant force on the beads, so the beads act independently like an ideal gas. Therefore, the chain size initially grows in a diffusive manner such that ${R_g}^2 \sim D_b t$.

This growth continues until the spring forces are large enough to compete with the thermal forces. If this occurs when the spring lengths are of order ℓ^*, then the spring forces are approximately $H_s \ell^*$ and the thermal forces are $k_B T/\ell^*$. Balancing these forces gives $\ell^* \sim \sqrt{k_B T/H_s}$. At this point, the scaling of the chain size with time changes to a new power law ${R_g}^2 \sim A t^\alpha$, where A and α will be determined below. Due to the influence of the significant spring forces, which impede the advancement of individual beads, the chain begins to grow subdiffusively so that $\alpha < 1$. We will refer to this new regime as the tension-dominated regime. The transition from the diffusive regime to the tension-dominated regime begins when ${R_g}^2$ is approximately $k_B T/H_s$ which occurs

at $t \sim k_B T / H_s D_b$.

The third regime, which we call the equilibrium regime, occurs when the chain reaches its final size of ${R_g}^2 \sim N_s k_B T / H_s$. This should occur at times on the order of the longest Rouse relaxation time of the chain or $t \sim {N_s}^2 k_B T / H_s D_b$. We can determine the power law exponent α and the scaling of the prefactor A for the tension-dominated regime by matching the end of the diffusive regime and the beginning of the equilibrium regime to the beginning and the end of the tension-dominated regime, respectively. Matching to the diffusive regime gives the expression ${R_g}^2 \sim k_B T / H_s \sim A \left(k_B T / H_s D_b\right)^{\alpha}$, and matching to the equilibrium regime gives ${R_g}^2 \sim N_s k_B T / H_s \sim A \left({N_s}^2 k_B T / H_s D_b\right)^{\alpha}$. This only holds valid for $\alpha = 1/2$ and $A \sim \sqrt{k_B T D_b / H_s}$. Combining all of our results, we finally arrive at a scaling for the chain size in all three regimes as a function of time

$$ {R_g}^2 \sim \begin{cases} D_b t, & t \ll \frac{k_B T}{H_s D_b}; \\ \left(\frac{k_B T D_b}{H_s} t\right)^{1/2}, & \frac{k_B T}{H_s D_b} \ll t \ll \frac{{N_s}^2 k_B T}{H_s D_b}; \\ \frac{N_s k_B T}{H_s}, & t \gg \frac{{N_s}^2 k_B T}{H_s D_b}. \end{cases} \tag{5.20} $$

In order to more rigorously confirm our scalings, particularly in the tension-dominate regime, we now develop a continuous 1D Rouse model for the transverse relaxation of an initially straight chain. We start with a discrete bead-spring chain with N_b beads connected by $N_s = N_b - 1$ Hookean springs with spring constant H_s. The 1D equation of motion for the nth bead position r_n is given by

$$ \zeta_b \frac{dr_n}{dt} = \begin{cases} H_s \left(r_2 - r_1\right) + F_1^{\mathrm{B}}, & n = 1, \\ H_s \left(r_{n+1} - 2r_n + r_{n-1}\right) + F_n^{\mathrm{B}}, & 1 < n < N_b, \\ -H_s \left(r_{N_b} - r_{N_b - 1}\right) + F_{N_b}^{\mathrm{B}}, & n = N_b, \end{cases} \tag{5.21} $$

where the random Brownian force F_n^{B} is characterized by

$$ \left\langle F_n^{\mathrm{B}}(t) \right\rangle = 0, \left\langle F_n^{\mathrm{B}}(t) F_m^{\mathrm{B}}(t') \right\rangle = 2 k_B T \zeta_b \delta_{nm} \delta(t - t') \tag{5.22} $$

The initial condition for the system is

$$ r_n|_{t=0} = 0 \tag{5.23} $$

If we allow n to be a continuous variable, we can rewrite Equations 5.21-5.23 as a partial differential equation

$$ \zeta_b \frac{\partial r_n}{\partial t} = H_s \frac{\partial^2 r_n}{\partial n^2} + F_n^{\mathrm{B}} \tag{5.24} $$

where the second moment of the Brownian force is now

$$ \left\langle F_n^{\mathrm{B}}(t) \right\rangle = 0, \left\langle F_n^{\mathrm{B}}(t) F_m^{\mathrm{B}}(t') \right\rangle = 2 k_B T \zeta_b \delta(n - m) \delta(t - t') \tag{5.25} $$

The initial condition and boundary conditions are given by

$$ r_n|_{t=0} = \left.\frac{\partial r_n}{\partial n}\right|_{n=0} = \left.\frac{\partial r_n}{\partial n}\right|_{n=N_b} = 0 \tag{5.26} $$

By solving the eigenvalue problem, we find that the normal coordinates are given by

$$x_p \equiv \frac{1}{N_b}\int_0^{N_b} dn \cos\left(\frac{p\pi n}{N_b}\right) r_n, \text{ with } p = 0, 1, 2, ... \tag{5.27}$$

and Equations 5.24-5.26 become

$$\zeta_p \frac{\partial x_p}{\partial t} = -H_{s,p} x_p + F_p^{\mathrm{B}} \tag{5.28}$$

where

$$\zeta_0 = N_b \zeta_b \text{ and } \zeta_p = 2N_b\zeta_b \text{ for } p = 1, 2, ... \tag{5.29}$$

$$H_{s,p} = 2\pi^2 H_s p^2 / N_b \text{ for } p = 0, 1, 2, ... \tag{5.30}$$

$$\left\langle F_p^{\mathrm{B}}(t)\right\rangle = 0, \left\langle F_p^{\mathrm{B}}(t) F_q^{\mathrm{B}}(t')\right\rangle = 2k_{\mathrm{B}}T\zeta_p\delta(p-q)\delta(t-t') \tag{5.31}$$

and

$$x_p|_{t=0} = 0 \tag{5.32}$$

We are interested in the chain's ensemble-averaged radius of gyration squared

$$\left\langle {R_g}^2(t)\right\rangle = \left\langle \frac{1}{N_b}\int_0^{N_b} dn \left[r_n(t) - R_{\mathrm{c.m.}}(t)\right]^2 \right\rangle \tag{5.33}$$

where $R_{\mathrm{c.m.}}(t)$ is the center of mass of the chain. The difference in the integrand can be rewritten in terms of the normal coordinates as

$$r_n(t) - R_{\mathrm{c.m.}}(t) = 4\sum_{p=1}^{\infty} x_p(t) \cos\left(\frac{p\pi n}{N_b}\right) \tag{5.34}$$

Plugging this expression into Equation 5.33 gives

$$\left\langle {R_g}^2(t)\right\rangle = \frac{4}{N_b}\sum_{p=1}^{\infty}\sum_{q=1}^{\infty} \left\langle x_p(t) x_q(t)\right\rangle \int_0^{N_b} dn \cos\left(\frac{p\pi n}{N_b}\right)\cos\left(\frac{q\pi n}{N_b}\right) \tag{5.35}$$

From linear response theory, it can be shown that for Equations 5.28-5.32

$$\left\langle x_p(t) x_q(t)\right\rangle = \delta_{pq}\frac{k_{\mathrm{B}}T}{H_{s,p}}\left[1 - \exp\left(\frac{-2t}{\zeta_p/H_{s,p}}\right)\right] \tag{5.36}$$

Combining this with Equation 5.35, we finally find

$$\left\langle {R_g}^2(t)\right\rangle = \frac{N_b k_{\mathrm{B}}T}{\pi^2 H_s}\sum_{p=1}^{\infty} p^{-2}\left[1 - \exp\left(\frac{-2\pi^2 H_s p^2}{{N_b}^2\zeta_b}t\right)\right] \tag{5.37}$$

At long times, the exponential dies off, and only the sum $\sum_{p=1}^{\infty} p^{-2} = \pi^2/6$ remains. This gives an equilibrium value of $\left\langle {R_g}^2(t)\right\rangle = \frac{N_b k_{\mathrm{B}}T}{6H_s}$ which is exactly the expected theoretical result.

If we transform the summation $\sum_{p=1}^{\infty}$ in Equation 5.37 to an integral $\int_{6/\pi^2}^{\infty} dp$ (the lower bound

has been chosen so that the equilibrium value remains the same) then our expression becomes

$$\langle {R_g}^2(t)\rangle = \frac{N_b k_B T}{6H_s}\left[1-\exp\left(\frac{-72H_s}{\pi^2 {N_b}^2\zeta_b}t\right)+\sqrt{\frac{72H_s}{\pi N_b{}^2\zeta_b}}\operatorname{terfc}\left(\sqrt{\frac{72H_s}{\pi^2 {N_s}^2\zeta_b}}t\right)\right] \tag{5.38}$$

Finally, since we are interested in short times (i.e., $t \ll \frac{\pi^2 {N_b}^2\zeta_b}{72H_s}$), we can expand this expression into a power series and keep only the leading order term

$$\langle {R_g}^2(t)\rangle = \sqrt{\frac{2k_B T D_b}{\pi H_s}}t \tag{5.39}$$

As predicted by our previous scaling arguments, in the tension-dominated regime ${R_g}^2 \sim t^{1/2}$.

For the diffusion-dominated regime, ${R_g}^2$ is simply the mean-squared displacement of a gas of beads that all initially start at the same point. This gives the well-known result ${R_g}^2 = 2D_b t$.

If we take all of our results, we can determine the locations of the regime transitions from the intersections of the expressions. Finally, combining all of our findings, we find

$${R_g}^2 \approx \begin{cases} 2D_b t, & t \ll \frac{k_B T}{H_s D_b}, \\ \left(\frac{2k_B T D_b}{\pi H_s}t\right)^{1/2}, & \frac{k_B T}{H_s D_b} \ll t \ll \frac{{N_s}^2 k_B T}{H_s D_b}, \\ \frac{N_s k_B T}{6H_s}, & t \gg \frac{{N_s}^2 k_B T}{H_s D_b}, \end{cases} \tag{5.40}$$

Comparing this to Equation 5.20, we find that our predicted scalings are, indeed, correct.

Our theoretical predictions for the two power law regimes of the unconfined case are plotted in Figure 5.5B to be compared to ${R_{g,y}}^2$. It is clear that our expression catches the qualitative behavior seen in the simulations. It quantitatively predicts the value in the diffusive regime at short times, but it overestimates the time at which the transition to the tension-dominated regime occurs. This leads to an overprediction of ${R_{g,y}}^2$ in the tension-dominated regime. These discrepancies are due to the non-linearities in the spring law when the chain is initially stretched beyond its linear regime. Effectively, this increases the spring constant H_s felt by the beads which, according to Equation 5.40, should decrease the time of the transition to the tension-dominated regime as well as the value of ${R_{g,y}}^2$ in this regime. So taking the spring law nonlinearities into account should bring the theoretical prediction more in line with the simulation results. The effects of these nonlinearities will be discussed in greater detail later.

Confined, Ideal Hookean Chain

When a Hookean chain relaxes in a channel of height $h \ll \sqrt{N_s k_B T/H_s}$, the equilibrium size of the chain in the confined dimension decreases to ${R_g}^2 \sim h^2$. Going further, if we assume that the bead distribution across the channel height is uniform, then ${R_g}^2 = h^2/12$. This is actually an overprediction of ${R_g}^2$ since the bead distribution is not truly uniform and has a Gaussian quality to it.

Assuming that $h \gg \sqrt{k_B T/H_s}$, the effect of confinement is both to limit the chain size and to

truncate the width of the tension-dominated regime so that

$$R_g{}^2 \approx \begin{cases} 2D_b t, & t \ll \frac{k_B T}{H_s D_b}, \\ \left(\frac{2k_B T D_b}{\pi H_s} t\right)^{1/2}, & \frac{k_B T}{H_s D_b} \ll t \ll \frac{\pi H_s h^4}{288 k_B T D_b}, \\ \frac{h^2}{12}, & t \gg \frac{\pi H_s h^4}{288 k_B T D_b}, \end{cases} \tag{5.41}$$

A similar expression can be written if $h \ll \sqrt{k_B T / H_s}$, but in that case, the diffusive regime is truncated and the tension-dominated regime is eliminated entirely.

This prediction for the confined case is also plotted in Figure 5.5B to be compared to $R_{g,z}{}^2$. Again, fairly good qualitative agreement exists between theory and simulations except that the tension-dominated regime is not seen in the theoretical prediction, as $h \ll \sqrt{k_B T / H_s}$, but it is present in the simulation results. As in the unconfined case, this is due to the nonlinearities in the spring law.

Excluded Volume

As mentioned in Section 5.5.1, the EV forces are not significant for moderately stretched chains. This means that the effects of EV will not be seen until the chain has relaxed significantly in the longitudinal direction, which only occurs on time scales on the order of τ_I or longer. This can clearly be seen in Figure 5.6 where the curves for the chain with EV do not deviate from those without EV until very near equilibrium. Therefore, the effects of EV on the transverse dynamics are minimal except at very long times.

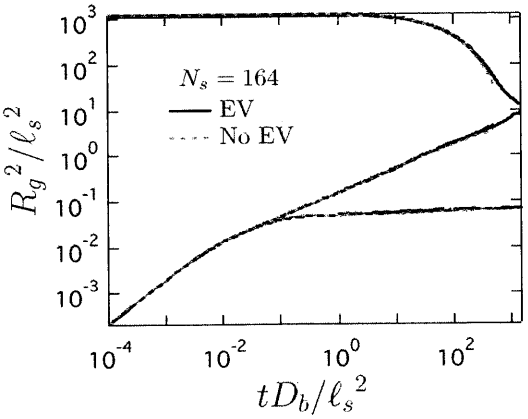

Fig. 5.6: *Plot of the 1D radius of gyration squared in all three directions for a single chain length of $N_s = 164$ both with and without EV. The initial stretch of the chain was 75% in a 300 nm channel.*

We can demonstrate this by considering a scaling analysis to estimate the fractional extension X_{ev} at which EV becomes important. Using a Flory-type approach, we begin by viewing the chain as a series of tension blobs whose in-plane dimensions are ξ_y and whose transverse dimensions are

h (i.e., they are small disks). Therefore, the pervaded volume of a tension blob scales as $\sim h{\xi_y}^2$. If there are g_y Kuhn lengths in a blob, then the z-interaction parameter of a blob is given by

$$z \sim \frac{F_\mathrm{I}}{k_\mathrm{B}T} \sim \nu^{\mathrm{ev,p}} \frac{{g_y}^2}{h{\xi_y}^2} \sim \frac{\nu^{\mathrm{ev,p}}}{h{b_\mathrm{K}}^2} g_y \tag{5.42}$$

where F_I is the Flory interaction energy of a blob and $\nu^{\mathrm{ev,p}}$ is the excluded volume parameter for a Kuhn length. The last scaling comes from assuming ideal chain statistics within a blob, as Flory did (i.e., $\xi_y \sim {g_y}^{1/2} b_\mathrm{K}$). The point at which EV becomes important is when $z \approx 1$. Therefore, the critical number of Kuhn lengths in a tension blob $g_{y,\mathrm{ev}}$ where EV becomes important is

$$g_{y,\mathrm{ev}} \sim \frac{h{b_\mathrm{K}}^2}{\nu^{\mathrm{ev,p}}} \tag{5.43}$$

which corresponds to a fractional extension of

$$X_\mathrm{ev} \sim \frac{(N_\mathrm{K}/g_{y,\mathrm{ev}})\,\xi_{y,\mathrm{ev}}}{N_\mathrm{K} b_\mathrm{K}} \sim {g_{y,\mathrm{ev}}}^{-1/2} \sim \sqrt{\frac{\nu^{\mathrm{ev,p}}}{h{b_\mathrm{K}}^2}} \tag{5.44}$$

For our choice of parameters, in a 300 nm channel, this corresponds to a fractional extension of $X_\mathrm{ev} \approx 0.3$. Of course, this is a scaling analysis, so order unity prefactors have been ignored. But this suggests that a chain must relax significantly in the longitudinal direction before EV effects become important, and this only occurs at very long times. This means that examining chain growth across multiple time scales by plotting the chain size against a logarithmic scale of time is inappropriate for the study of the effects of EV. In order to see these effects, a linear time scale must be used which is precisely the sort of analysis performed in Section 5.5.1.

EV does not directly affect the dynamics of the confined dimension, even at long time scales, as will be shown in the following section. However, we will show that under certain conditions spring nonlinearities can lead to coupling between the confined and longitudinal dimensions that affects the relaxation of ${R_{g,z}}^2$ to its true equilibrium value at long times. Therefore, ${R_{g,z}}^2$ is sensitive to EV insofar as the longitudinal dimension is affected by EV at long times. On the other hand, the unconfined, transverse dimension certainly feels the effects of EV as it nears the equilibrium value it shares with the longitudinal dimension, but at this point, these two unconfined dimensions are governed by the same linear relaxation processes which have already been studied in significant detail in Section 5.5.1. So no further analysis is required.

Nonlinearities

Finally, we consider the effects of the spring nonlinearities, which are most evident at the beginning of the relaxation process when the springs are highly stretched. One consequence of these nonlinearities is that the spring force is no longer independent for each dimension. This means that the strong stretching in the longitudinal direction leads to an increased effective spring constant in both of the transverse directions. As already pointed out in Sections 5.5.2 and 5.5.2, this can lead to deviations from the Hookean theory and retards the growth of the transverse dimensions during the tension-dominated regime.

In order to clearly demonstrate this effect, we simulated the relaxation of a chain from several different initial fractional extensions. The results are shown in Figure 5.7. It has been observed

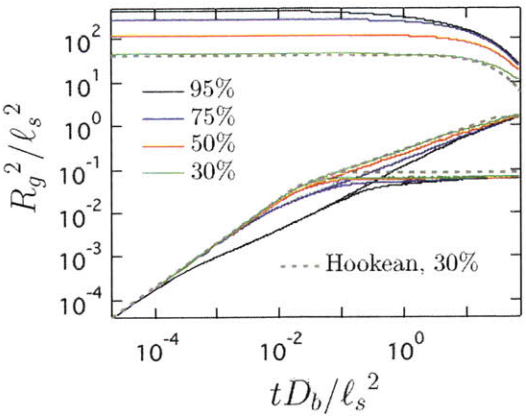

Fig. 5.7: *Plot of the 1D radius of gyration squared in all three directions for a single chain length of $N_s = 75$ in a 300 nm channel. The results for various values of the initial fractional extension are shown. Also included is the Hookean theory given by Equation 5.40 and 5.41.*

that chains behave in a Hookean manner up to fractional extensions around 30%. In accordance with this, excellent agreement is seen between the Hookean theory and the chain initially stretched to 30%. As the initial extension is increased, the size in the transverse dimensions falls farther below that of the theory. This is precisely the expected effect of the strong nonlinearities in the springs at high extensions.

The nonlinearities also affect the equilibrium regime of the confined, transverse dimension. Figure 5.8A shows a zoomed in view of Figure 5.5B in this region for several different chain lengths. ${R_{g,z}}^2$ is the same for all three chain lengths through the diffusive and tension-dominated regimes, but they behave somewhat differently once they reach the equilibrium regime. The Hookean theory of Section 5.5.2 predicts that ${R_{g,z}}^2$ should immediately plateau to its final equilibrium value after the tension-dominated regime, but clearly the dynamics are richer for real chains. All three chain lengths exit the tension-dominated regime by temporarily pausing their growth of ${R_{g,z}}^2$ at an intermediate value slightly below their final equilibrium. The duration of this pause is dependent upon the chain length. For $N_s = 10$, the pause is only barely evident, while it is quite significant for $N_s = 300$. After this interruption in its growth, ${R_{g,z}}^2$ slowly approaches its final value.

In order to prove that this behavior is due to the spring nonlinearities, we ran a simulation where an initially stretched chain was allowed to relax in the transverse directions, but its initial longitudinal stretch was held fixed for all time. The result is shown in Figure 5.8B along with the results for chains with and without EV that are allowed to relax in the longitudinal direction. The two chains that are allowed to relax in all dimensions are nearly identical except that the chain with EV has a slightly higher final equilibrium value at long times. Therefore, EV cannot account for this behavior. On the other hand, the chain whose stretch is held fixed plateaus at its final value precisely where the other chains temporarily pause. Clearly, this temporary arrest in the growth is due to the nonlinearities of the springs, and the subsequent slow approach to equilibrium is due to the relaxation of the longitudinal stretch which reduces the tension in the springs.

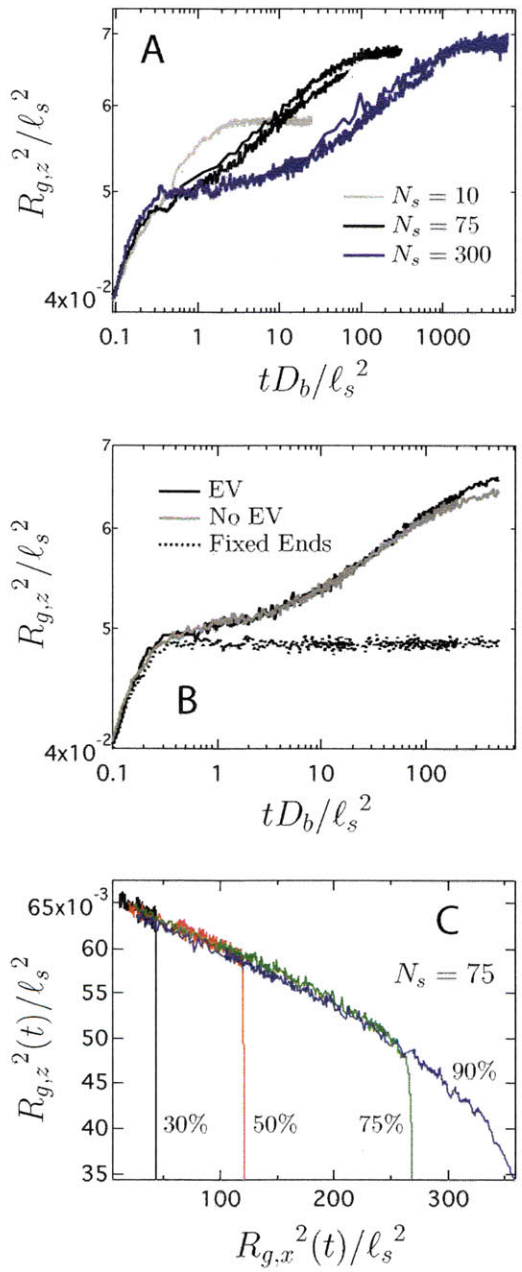

Fig. 5.8: *(A) Plot of 1D radius of gyration squared in the confined, transverse dimension $R_{g,z}{}^2$ for several different chain lengths in a 300 nm channel with an initial fractional extension of 75%. Only the equilibrium regime is shown (see Figure 5.5B for the entire relaxation process). Two curves are seen for $N_s = 75$ and 300 because the data from both the short time and long time simulations are plotted. (B) Plot of 1D radius of gyration squared in the confined, transverse dimension $R_{g,z}{}^2$ for a single chain length of $N_s = 75$ in a 300 nm channel with an initial fractional extension of 75%. The results for three different cases are shown: with EV, without EV, and the longitudinal stretch held fixed. Only the equilibrium regime is shown. (C) Plot of 1D radius of gyration squared in the confined, transverse dimension $R_{g,z}{}^2$ versus the 1D radius of gyration squared in the longitudinal dimension $R_{g,x}{}^2$ for a single chain length of $N_s = 75$ in a*

To demonstrate that relaxation of the longitudinal stretch is responsible for the slow approach to equilibrium after the pause, we have taken the data from Figure 5.7 and plotted ${R_{g,z}}^2$ against ${R_{g,x}}^2$. This is shown in Figure 5.8C for different initial chain extensions. Initially, ${R_{g,z}}^2$ grows during the diffusive and tension-dominated regimes without much change in ${R_{g,x}}^2$ which relaxes on much longer timescales. But once the equilibrium regime is reached, all the curves fall on the same universal curve. This reveals that a quasi-steady equilibrium exists for ${R_{g,z}}^2$ during the equilibrium regime, and it is slaved to the relaxation of the longitudinal stretch. This is also verifies the quasi-steady assumption made in the tension-blob physical model for the relaxation as discussed in Section 5.3.2.

A consequence of this quasi-steady equilibrium is that during the equilibrium regime, ${R_{g,z}}^2$ is a measure of the relaxation of the longitudinal stretch. This means analyzing ${R_{g,z}}^2$ provides another way of studying the relaxation times of the chain. We can do this by defining a relaxation function $G_z(t) = [{R_{g,z,0}}^2 - {R_{g,z,0}}^2]/{\ell_s}^2$ for the confined dimension. A characteristic curve for $G_z(t)$ is shown in Figure 5.9A. An obvious linear region is seen, indicative of a single exponential decay with the time constant $\tau_{{R_{g,z}}^2}$. Since this approach to equilibrium is due the nonlinearities in the spring law when the longitudinal direction is extended beyond 30%, it is expected that $\tau_{{R_{g,z}}^2}$ should provide an estimate of the bulklike relaxation time τ_I. Indeed, good agreement is found between the two as seen in Figure 5.9B, and it is clear that they follow the same scaling $\tau_{{R_{g,z}}^2} \approx \tau_I \sim {N_s}^{2.2}$.

5.6 Conclusions

We have used Brownian Dynamics simulations to study the relaxation of initially stretched chains in slitlike confinement. We have shown that our simulation technique is capable of reproducing the qualitative findings of recent experimental studies. In particular, our simulations clearly show the existence of two distinct relaxation times in the linear force regime: one that scales similar to a bulklike relaxation time, and another that follows the scalings predicted by blob theory. We have conclusively demonstrated that the emergence of the second relaxation time is due to excluded volume effects and not hydrodynamic interactions.

We developed a Rouse-like theory to describe the confined relaxation of the transverse dimensions of an initially straight bead-spring chain and find good agreement between our theory and the simulations. The effects of excluded volume and spring nonlinearities on the dynamics were also explored. It was found that these nonlinearities lead to a quasi-steady equilibrium between the size of the chain in the confined dimension and in the longitudinal dimension. This corroborates one of the underlying assumptions of the physical model for confined relaxation proposed by Balducci and coworkers [31].

Our results are important to developing a clear mechanistic understanding of the relaxation of polymers in slitlike confinement. Not only is this a problem of fundamental importance in polymer physics, it is also has practical interest for the development of microfluidic devices that exploit confinement to manipulate DNA molecules. This work only considered the scalings of the relaxation times with chain length, and the height of the channel was not varied. Future studies should examine the predicted scalings of the relaxation times with channel height. Additionally, hydrodynamics interactions were not included in the simulation model, and their effects should be explored at a later date.

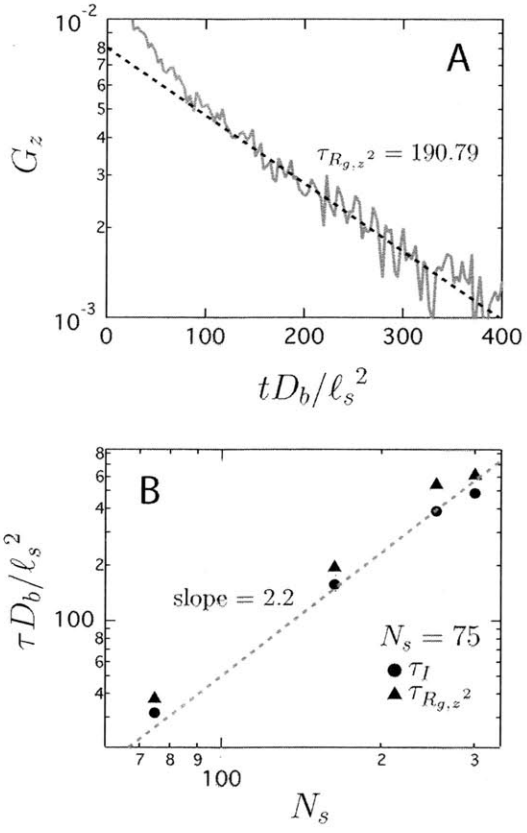

Fig. 5.9: *(A) Characteristic plot of the confined transverse relaxation function* $G_z(t) = [R_{g,z,0}{}^2 - R_{g,z,0}{}^2]/\ell_s{}^2$ *for chain length* $N_s = 164$. *The fitting for the linear region is shown. (B) Plot of the bulklike relaxation times* τ_I *and* $\tau_{R_{g,z}{}^2}$ *vs. chain length* N_s. *Also shown is the predicted scaling* $\tau_{R_{g,z}{}^2} \sim \tau_I \sim N_s{}^{2.2}$.

CHAPTER 6

Outlook

In this thesis, we have presented simulations of the single molecule behavior of DNA in microfluidic devices related to gene mapping. In particular, we have considered the use of a post array to precondition molecules for subsequent stretching in a contraction, the electrophoretic collision of a DNA molecule with a large, ideally conducting post, and the relaxation process of an initially stretched molecule in slitlike confinement. In this final chapter, we would like to briefly summarize our findings, their impact, and suggested future directions.

In our study of conformational preconditioning using an array of posts, we found good qualitative agreement between experiments and our simulations for the behavior of DNA in the post array. But our simulations consistently overpredicted the final stretch of molecules at the end of the contraction. Our study suggests that nonlinear electrokinetic effects play a significant role in the dynamics of the contraction. This should be investigated in the future, and indeed, preliminary results from a nascent experimental study in our group seem to support this finding.

After this study using an array of insulating posts, we considered the electrophoretic collisions with conducting posts. As this was the first study of such collisions, we simplified the problem in order to help distill out the essential physics the govern the problem. In particular, we found that field-induced compression plays a critical role in understanding the escape process of a molecule trapped on the post surface. We performed an extensive theoretical analysis both for this problem, which also had not been previously studied, and the larger collision problem. Of course, our simulation results should be compared to future experiments. A question that still remains is what the effect of including intramolecular excluded volume would be. Additionally, we expect

that collisions with moderately sized conducting posts and movement through arrays of such posts should prove very different than their insulating counterparts. Indeed, they may offer distinct advantages for separation and concentration purposes as they induce strong interactions between the molecules and the posts.

Finally, we looked at the confined relaxation of DNA in a slit. We presented the first simulation results that show two distinct relaxation times in the linear force regime as previously reported in recent experiments. We focused on the dynamics in the transverse directions, particularly at short times and on small length scales, because they are experimentally inaccessible. We developed a theoretical model to describe the transverse dynamics at all time scales, finding several different scaling regimes. We used our simulation results to compare to a recent mechanistic model developed to describe confined relaxation and found qualitative agreement with its predictions. Future studies should attempt to probe even tighter confinement, moving into the Odijk regime, where the physics of relaxation should qualitatively change. Our simulations were limited, however, by the accuracy of our numerical model in tight confinement. Future work should be directed toward developing new simulation models that are more accurate in confinement without becoming too computationally costly. In particular, this means developing new spring laws that take into account the restricted phase space of the spring and new excluded volume potentials based upon blob theory models to accurately predict the strength of EV effects, particularly as a function of gap height.

The overall impact of this thesis is to have either confirmed, explained, or suggested the behavior and underlying physics of DNA in microfluidic devices of particular import to gene mapping technologies. We have hypothesized that nonlinear electrokinetic effects are important in microcontractions. We have developed an extensive theory for collisions with conducting posts and have introduced the notion of field-induced confinement. Finally, we corroborated the tension blob model for confined relaxation as well as developing theory for the transverse dynamics. All of these findings are significant and will play an important role in developing new device designs both for gene mapping and other applications.

Appendix A

Green's Function Approach to Field-induced Compression

A.1 Green's Function

A.1.1 Problem Statement

The Green's function $G(z, z'; n)$ represents the statistical weight (or the partition function) of the chain which starts from z' and ends at z in n steps. It obeys the partial differential equation

$$\left[\frac{\partial}{\partial n} - \frac{k_B T}{2H}\frac{\partial^2}{\partial z^2} + \frac{1}{k_B T}U_e(z)\right] G(z, z'; n) = \delta(z - z')\,\delta(n), \tag{A.1}$$

where H is the spring constant associated with a Kuhn segment, $U_e(z)$ is the external potential acting upon each chain segment, and both $\delta(z - z')$ and $\delta(n)$ are the Dirac delta functions.

For the case of a uniform transverse field compressing a chain against a flat wall, the potential is given by

$$U_e(z) = \Gamma_K E_0 z, \tag{A.2}$$

where Γ_K is the effective charge per Kuhn segment, E_0 is the applied electric field, and z is the

distance from the wall. We can nondimensionalize Equation A.1 based upon

$$\eta = \frac{n}{N_{\mathrm{K}}}, \tag{A.3}$$

$$\hat{z} = \frac{z}{\sqrt{N_{\mathrm{K}} k_{\mathrm{B}} T / H}}, \tag{A.4}$$

$$\hat{G}\left(\hat{z}, \hat{z}'; \eta\right) = \sqrt{N_{\mathrm{K}} k_{\mathrm{B}} T / H} G\left(z, z'; n\right), \tag{A.5}$$

$$Pe = \frac{N_{\mathrm{K}} \Gamma_{\mathrm{K}} E_0 \sqrt{N_{\mathrm{K}} k_{\mathrm{B}} T / H}}{k_{\mathrm{B}} T} = {N_{\mathrm{K}}}^{3/2} \frac{\Gamma_{\mathrm{K}} E_0}{\sqrt{k_{\mathrm{B}} T H}} = {N_{\mathrm{K}}}^{3/2} Pe_{\mathrm{K}}, \tag{A.6}$$

where N_{K} is the number of Kuhn steps in the chain, Pe is the chain Péclet number, and Pe_{K} is the Péclet number based upon a Kuhn segment. This leads to the following dimensionless form of Equation A.1

$$\frac{\partial \hat{G}}{\partial \eta} = \frac{1}{2} \frac{\partial^2 \hat{G}}{\partial \hat{z}^2} - Pe \hat{z} \hat{G} + \delta\left(\hat{z} - \hat{z}'\right) \delta(\eta). \tag{A.7}$$

For our boundary conditions, we choose to place the chain between two parallel, impenetrable separated by a distance L. Because the chain cannot pass through the walls, the probability of finding any segment of the chain at $z = 0$ or $z = L$ is zero:

$$\hat{G}\left(\hat{z} = 0, \hat{z}'; \eta\right) = \hat{G}\left(\hat{z} = \hat{L}, \hat{z}'; \eta\right) = 0. \tag{A.8}$$

Equations A.7 and A.8 define our problem which can be solved using a finite Fourier transform.

A.1.2 Associated Eigenvalue Problem

To begin, we solve the associated eigenvalue problem:

$$\frac{1}{2} \frac{d^2 \phi_i}{d \hat{z}^2} - Pe \hat{z} \phi_i = -{\lambda_i}^2 \phi_i, \tag{A.9}$$

$$\phi_i\left(\hat{z} = 0\right) = \phi_i\left(\hat{z} = \hat{L}\right) = 0, \tag{A.10}$$

where ϕ_i and λ_i are the ith eigenfunction and eigenvalue, respectively. If we perform the following change of variables

$$u_i = (2Pe)^{1/3} \left(\hat{z} - \frac{{\lambda_i}^2}{Pe}\right), \tag{A.11}$$

then Equation A.9 becomes

$$\frac{d^2 \phi_i}{d {u_i}^2} = u_i \phi_i. \tag{A.12}$$

The two linearly independent solutions of this equation are the Airy functions of the first and second kind $\mathrm{Ai}(x)$ and $\mathrm{Bi}(x)$, respectively:

$$\phi_i\left(u_i\right) = c_{1,i} \mathrm{Ai}\left(u_i\right) + c_{2,i} \mathrm{Bi}\left(u_i\right), \tag{A.13}$$

where $c_{1,i}$ and $c_{2,i}$ are chosen to meet the orthonormality requirement of the eigenfunctions. Returning to the variable $\hat{z}$, the eigenfunctions are given by

$$\phi_i(\hat{z}) = c_{1,i}\mathrm{Ai}\left[(2Pe)^{1/3}\left(\hat{z} - \frac{{\lambda_i}^2}{Pe}\right)\right] + c_{2,i}\mathrm{Bi}\left[(2Pe)^{1/3}\left(\hat{z} - \frac{{\lambda_i}^2}{Pe}\right)\right], \tag{A.14}$$

and the eigenvalues are chosen such that the boundary conditions are met and are defined by the equation

$$\lambda_i\text{: } \mathrm{Ai}\left[\frac{-2^{1/3}{\lambda_i}^2}{Pe^{2/3}}\right]\mathrm{Bi}\left[(2Pe)^{1/3}\left(\hat{L} - \frac{{\lambda_i}^2}{Pe}\right)\right] - \mathrm{Ai}\left[(2Pe)^{1/3}\left(\hat{L} - \frac{{\lambda_i}^2}{Pe}\right)\right]\mathrm{Bi}\left[\frac{-2^{1/3}{\lambda_i}^2}{Pe^{2/3}}\right] = 0. \tag{A.15}$$

$c_{1,i}$ and $c_{2,i}$ must be chosen so that ϕ_i is orthonormal.

A.1.3 Solution

We assume $\hat{G}(\hat{z}, \hat{z}'; \eta)$ can be written in the form

$$\hat{G}(\hat{z}, \hat{z}'; \eta) = \sum_i \hat{g}_i(\hat{z}'; \eta)\phi_i(\hat{z}), \tag{A.16}$$

where $\hat{g}_i(\hat{z}'; \eta)$ is the weighting of the ith eigenfunction and is defined as the inner product of the ith eigenfunction $\phi_i(\hat{z})$ with $\hat{G}(\hat{z}, \hat{z}'; \eta)$:

$$\hat{g}_i(\hat{z}'; \eta) = \left\langle \phi_i(\hat{z}), \hat{G}(\hat{z}, \hat{z}'; \eta) \right\rangle_{\hat{z}}, \tag{A.17}$$

where the subscript $\hat{z}$ denotes that the inner product is taken with respect to the variable $\hat{z}$.

If we transform Equation A.7 by taking the inner product of each side with the ith eigenfunction $\phi_i(\hat{z})$, perform two rounds of integration by parts, and then make use of Equations A.9 and A.17, we arrive at the following ordinary differential equation for the weightings $\hat{g}_i(\hat{z}'; \eta)$

$$\frac{d\hat{g}_i}{d\eta} + {\lambda_i}^2\hat{g}_i = \phi_i(\hat{z}')\delta(\eta). \tag{A.18}$$

By integrating both sides as follows

$$\int_{-\infty}^{\eta} \frac{d}{d\eta'}\left[\exp\left({\lambda_i}^2\eta'\right)\hat{g}_i\right]d\eta' = \int_{-\infty}^{\eta} \phi_i(\hat{z}')\exp\left({\lambda_i}^2\eta'\right)\delta(\eta')d\eta', \tag{A.19}$$

gives

$$\exp\left({\lambda_i}^2\eta\right)\hat{g}_i - 0 = \phi_i(\hat{z}')\exp(0), \tag{A.20}$$

so the weightings are given by

$$\hat{g}_i(\hat{z}'; \eta) = \phi_i(\hat{z}')\exp\left(-{\lambda_i}^2\eta\right). \tag{A.21}$$

Using this result along with Equation A.16, we have the general solution for the Green's function:

$$\hat{G}\left(\hat{z},\hat{z}';\eta\right)=\sum_{i}\exp\left(-{\lambda_i}^2\eta\right)\phi_i(\hat{z})\phi_i(\hat{z}'). \tag{A.22}$$

A.1.4 Semi-infinite Domain, $L\to\infty$

We now take the limit of our general solution given by Equation A.22 as $L\to\infty$ in order to obtain the special case of the two walls being separated by an infinite distance. Because the chain is electrophoretically pushed toward the wall at $z=0$, the second wall at $z=\infty$ has no effect on the chain, and the solution will be identical to a chain in a semi-infinite domain being pushed against a single wall.

We begin by considering Equation A.15 for the eigenvalues in the limit $\hat{L}\to\infty$ (note that the following is only valid if $Pe>0$). Because $\mathrm{Ai}(\infty)=0$, the second term on the RHS of Equation A.15 vanishes. On the other hand, $\mathrm{Bi}(\infty)=\infty$ so that the first term on the RHS blows up unless the eigenvalues are chosen such that

$$\lambda_i\text{: }\mathrm{Ai}\left[\frac{-2^{1/3}{\lambda_i}^2}{Pe^{2/3}}\right]=0. \tag{A.23}$$

Therefore, the eigenvalues are given by

$$\lambda_i=\left(\frac{Pe}{\sqrt{2}}\right)^{1/3}\sqrt{-a_i}, \tag{A.24}$$

where a_i is the ith root of the Airy function $\mathrm{Ai}(x)$ ordered such that $a_{j+1}<a_j<0$ for $j=1,2,3,...$ The eigenfunctions given in Equation A.14 become

$$\phi_i\left(\hat{z}\right)=c_{1,i}\mathrm{Ai}\left[(2Pe)^{1/3}\left(\hat{z}-\frac{{\lambda_i}^2}{Pe}\right)\right]=c_{1,i}\mathrm{Ai}\left[(2Pe)^{1/3}\,\hat{z}+a_i\right]. \tag{A.25}$$

This suggests a rescaling of the length and a new variable ξ is defined as

$$\xi=(2Pe)^{1/3}\hat{z}. \tag{A.26}$$

Therefore, the eigenfunctions become

$$\phi_i(\xi)=c_{1,i}\mathrm{Ai}\left(\xi+a_i\right), \tag{A.27}$$

and the orthonormality requirement demands that

$$c_{1,i}=(2Pe)^{1/6}\left\{\int_0^\infty d\xi\left[\mathrm{Ai}(\xi+a_i)\right]^2\right\}^{-1/2}. \tag{A.28}$$

The Green's function $\Psi\left(\xi,\xi';\eta\right)$ based upon the new length variable ξ is defined as

$$\Psi\left(\xi,\xi';\eta\right)=(2Pe)^{-1/3}\hat{G}\left(\hat{z},\hat{z}';\eta\right). \tag{A.29}$$

Finally, we can state that the Green's function for the field-induced compression of a Gaussian chain against a flat wall by a uniform transverse field is described by

$$\Psi\left(\xi,\xi';\eta\right) = \sum_{i=1}^{\infty} \exp\left[a_i \left(\frac{Pe}{\sqrt{2}}\right)^{2/3} \eta\right] \frac{\mathrm{Ai}\left(\xi + a_i\right) \mathrm{Ai}\left(\xi' + a_i\right)}{\int_0^\infty d\xi \left[Ai(\xi + a_i)\right]^2}. \tag{A.30}$$

A.1.5 Blob Regime, $Pe \to \infty$

We now simplify our result for the case of $Pe \to \infty$. This can be seen as either the long chain limit $N_\mathrm{K} \to \infty$ or the strong field limit $Pe_\mathrm{K} \to \infty$. In essence, this is the blob regime. As long as the dimensionless number of steps $\eta \gg \left(Pe/\sqrt{2}\right)^{-2/3}$, then only the first term of the infinite series in Equation A.30 contributes to the sum, so

$$\Psi\left(\xi,\xi';\eta\right) = \exp\left[a_1 \left(\frac{Pe}{\sqrt{2}}\right)^{2/3} \eta\right] \frac{\mathrm{Ai}\left(\xi + a_1\right) \mathrm{Ai}\left(\xi' + a_1\right)}{\int_0^\infty d\xi \left[Ai(\xi + a_1)\right]^2}. \tag{A.31}$$

It must be stressed, however, that the restrictions on this equation are that $Pe > 0$ and $\eta \gg \left(Pe/\sqrt{2}\right)^{-2/3}$.

A.2 Calculation of $\left\langle \hat{d}_w \right\rangle$ and $\left\langle \hat{R}_{g,w}^2 \right\rangle$

A.2.1 Probability Distribution Function for ξ_η

The probability of finding an internal segment of the chain $0 < \eta < 1$ at position ξ is given by

$$P(\xi_\eta) = \frac{\int_0^\infty \int_0^\infty d\xi_0 d\xi_1 \Psi\left(\xi_0,\xi_\eta;\eta\right) \Psi\left(\xi_\eta,\xi_1;1-\eta\right)}{\int_0^\infty \int_0^\infty d\xi_0 d\xi_1 \Psi\left(\xi_0,\xi_1;1\right)}. \tag{A.32}$$

If we use our blob regime result given by Equation A.31, then we find that

$$P(\xi_\eta) = \frac{\left[\mathrm{Ai}\left(\xi_\eta + a_1\right)\right]^2}{\int_0^\infty d\xi \left[Ai(\xi + a_1)\right]^2}. \tag{A.33}$$

We can also say that by "internal" we mean that both η and $1 - \eta$ are $\gg \left(Pe/\sqrt{2}\right)^{-2/3}$.

A.2.2 Moments of $P(\xi_\eta)$

We can calculate the moments of this probability distribution by noting that

$$a_1 \approx -2.33811. \tag{A.34}$$

The first moment of ξ_η is given by

$$\langle \xi_\eta \rangle = \int_0^\infty d\xi_\eta \xi_\eta P(\xi_\eta) = \frac{\int_0^\infty d\xi_\eta \xi_\eta \left[\mathrm{Ai}\left(\xi_\eta + a_1\right)\right]^2}{\int_0^\infty d\xi \left[Ai(\xi + a_1)\right]^2} \approx 1.558740, \tag{A.35}$$

and the second moment is

$$\left\langle {\xi_\eta}^2 \right\rangle = \int_0^\infty d\xi_\eta {\xi_\eta}^2 P(\xi_\eta) = \frac{\int_0^\infty d\xi_\eta {\xi_\eta}^2 \left[\mathrm{Ai}\left(\xi_\eta + a_1\right)\right]^2}{\int_0^\infty d\xi \left[Ai(\xi + a_1)\right]^2} \approx 2.9156. \tag{A.36}$$

A.2.3 $\langle d_w \rangle$ *and* $\left\langle {R_{g,w}}^2 \right\rangle$

With these moments in hand, we are now prepared to calculate the average distance from the wall $\langle d_w \rangle$ of a chain and its average radius of gyration squared $\left\langle {R_{g,w}}^2 \right\rangle$:

$$\frac{\langle d_w \rangle}{\sqrt{k_\mathrm{B}T/H}} = {N_\mathrm{K}}^{1/2}(2Pe)^{-1/3} \langle \xi_\eta \rangle \approx 1.558740 {N_\mathrm{K}}^{1/2}(2{N_\mathrm{K}}^{3/2}Pe_\mathrm{K})^{-1/3} = 1.237173 {Pe_\mathrm{K}}^{-1/3}, \tag{A.37}$$

and

$$\frac{\left\langle {R_{g,w}}^2 \right\rangle}{k_\mathrm{B}T/H} = N_\mathrm{K}(2Pe)^{-2/3} \left(\left\langle {\xi_\eta}^2 \right\rangle - \langle \xi_\eta \rangle^2 \right) \approx (2.9156 - 1.558740^2)(2Pe_\mathrm{K})^{-2/3} = 0.3061 {Pe_\mathrm{K}}^{-2/3}. \tag{A.38}$$

These scalings are exactly those predicted using the simply blob theory framework. Additionally, the analytically prefactors derived here nearly match those found by fitting simulation results.

Bibliography

[1] Lander, E. S.; et. al., *Nature* **2001**, *409*, 860.

[2] Chan, E. Y.; Goncalves, N. M.; Haeusler, R. A.; Hatch, A. J.; Larson, J. W.; Maletta, A. M.; Yantz, G. R.; Carstea, E. D.; Fuchs, M.; Wong, G. G.; Gullans, S. R.; Gilmanshin, R., *Genome Res.* **2004**, *14*, 1137.

[3] Viovy, J. L., *Rev. Mod. Phys.* **2000**, *72*, 813.

[4] Volkmuth, W. D.; Austin, R. H., *Nature* **1992**, *358*, 600.

[5] Nixon, G.; Slater, G., *Phys. Rev. E* **1994**, *50*, 5033.

[6] Sevick, E. M.; Williams, D. R. M., *Phys. Rev. E* **1994**, *50*, R3357.

[7] Sevick, E. M.; Williams, D. R. M., *Phys. Rev. Lett.* **1996**, *76*, 2595.

[8] Saville, P.; Sevick, E. M., *Macromolecules* **1999**, *32*, 892.

[9] Randall, G. C.; Doyle, P. S., *Macromolecules* **2006**, *39*, 7734.

[10] Kim, J. M.; Doyle, P. S., *Macromolecules* **2007**, *40*, 9151.

[11] Duke, T.; Austin, R. H., *Phys. Rev. Lett.* **1998**, *80*, 1552.

[12] Huang, L.; Silberzan, P.; Tegenfeldt, J.; Cox, E.; Sturm, J.; Austin, R. H.; Craighead, H. G., *Phys. Rev. Lett.* **2002**, *89*, 178301.

[13] Baba, M.; Sano, T.; Iguchi, N.; Iida, K.; Sakamoto, T.; Kawaura, H., *App. Phys. Lett.* **2003**, *83*, 1468.

[14] Han, J.; Turner, S.; Craighead, H. G., *Phys. Rev. Lett.* **1999**, *83*, 1688.

[15] Han, J.; Craighead, H. G., *Science* **2000**, *288*, 1026.

[16] Han, J.; Craighead, H. G., *Anal. Chem.* **2002**, *74*, 394.

[17] Turner, S.; Cabodi, M.; Craighead, H. G., *Phys. Rev. Lett.* **2002**, *88*, 128103.

[18] Cabodi, M.; Turner, S.; Craighead, H. G., *Anal. Chem.* **2002**, *74*, 5169.

[19] Mannion, J.; Reccius, C.; Cross, J.; Craighead, H. G., *Biophys. J.* **2006**, *90*, 4538.

[20] Meagher, R.; Won, J.; McCormick, L.; Nedelcu, S.; Bertrand, M.; Bertram, J.; Drouin, G.; Barron, A.; Slater, G., *Electrophoresis* **2005**, *26*, 331.

[21] Randall, G. C.; Doyle, P. S., *Macromolecules* **2005**, *38*, 2410.

[22] Randall, G. C.; Schultz, K.; Doyle, P. S., *Lab Chip* **2006**, *6*, 516.

[23] Long, D.; Viovy, J.; Ajdari, A., *Phys. Rev. Lett.* **1996**, *76*, 3858.

[24] de Gennes, P. G., *Science* **1997**, *276*, 1999.

[25] Duggal, R.; Pasquali, M., *J. Rheol.* **2004**, *48*, 745.

[26] Deutsch, J. M., *Science* **1988**, *240*, 922.

[27] Austin, R. H.; Volkmuth W. D., *Analusis* **1993**, *21*, 235.

[28] Brochard, F., *J. Phys. (Paris)* **1977**, *38*, 1285.

[29] Daoud, M.; de Gennes, P. G., *J. Phys. (Paris)* **1977**, *38*, 85.

[30] Bakajin, O. B.; Duke, T. A. J.; Chou, C. F.; Chan, S. S.; Austin, R. H.; Cox, E. C., *Phys. Rev. Lett.* **1998**, *80*, 2737.

[31] Balducci, A.; Hsieh, C.-C.; Doyle, P. S., *Phys. Rev. Lett.* **2007**, *99*, 238102.

[32] Bonthuis, D. J.; Meyer, C.; Stein, D.; Dekker, C., *Phys. Rev. Lett.* **2008**, *101*, 108303.

[33] Marko, J. F.; Siggia, E. D., *Macromolecules* **1995**, *28*, 8759.

[34] Smith, S.; Cui, Y.; Bustamante, C., *Science* **1996**, *271*, 795.

[35] Ashkin, A.; Dziedzic, J.; Bjorkholm, J.; Chu, S., *Opt. Lett.* **1986**, *11*, 288.

[36] Perkins, T. T.; Quake, S. R.; Smith, D. E.; Chu, S., *Science* **1994**, *264*, 822.

[37] Perkins, T.; Smith, D.; Larson, R.; Chu, S., *Science* **1995**, *268*, 83.

[38] Ferree, S.; Blanch, H., *Biophys. J.* **2003**, *85*, 2539.

[39] Bird, R. B.; Armstrong, R. C.; Hassager, O., *Dynamics of Polymeric Liquids*; Vol. 1: Fluid Mechanics; Wiley, New York, second ed., 1987.

[40] Smith, D.; Babcock, H.; Chu, S., *Science* **1999**, *283*, 1724.

[41] Perkins, T.; Smith, D.; Chu, S., *Science* **1997**, *276*, 2016.

[42] Nollert, M.; Olbricht, W., *Rheol. Acta.* **1985**, *24*, 3.

[43] Larson, R., *J. Non-Newtownian Fluid Mech.* **2000**, *94*, 37.

[44] Chopra, M.; Li, L.; Hu, H.; Burns, M.; Larson, R., *J. Rheol.* **2003**, *47*, 1111.

[45] Panwar, A.; Kumar, S., *J. Chem. Phys.* **2003**, *118*, 925.

[46] Beck, V.; Shaqfeh, E., *J. Chem. Phys.* **2006**, *124*, 094902.

[47] Szeri, A.; Wiggins, S.; Leal, L., *J. Fluid Mech.* **1991**, *228*, 207.

[48] Underhill, P.; Doyle, P. S., *Phys. Rev. E* **2007**, *76*, 011805.

[49] Randall, G. C.; Doyle, P. S., *Phys. Rev. Lett.* **2004**, *93*, 058102.

[50] Deutsch, J.; Madden, T., *J. Chem. Phys.* **1989**, *90*, 2476.

[51] Deutsch, J., *J. Chem. Phys.* **1989**, *90*, 7436.

[52] Volkmuth, W. D.; Duke, T.; Wu, M. C.; Austin, R. H.; Szabo, A., *Phys. Rev. Lett.* **1994**, *72*, 2117.

[53] André, P.; Long, D.; Ajdari, A., *Eur. Phys. J. B* **1998**, *4*, 307.

[54] Sevick, E. M.; Williams, D. R. M., *Europhys. Lett.* **2001**, *56*, 529.

[55] Patel, P.; Shaqfeh, E., *J. Chem. Phys.* **2003**, *118*, 2941.

[56] Dorfman, K.; Viovy, J., *Phys. Rev. E* **2004**, *69*, 011901.

[57] Doyle, P. S.; Bibette, J.; Bancaud, A.; Viovy, J.-L., *Science* **2002**, *295*, 2237.

[58] Bird, R. B.; Curtiss, C. F.; Armstrong, R. C.; Hassager, O., *Dynamics of Polymeric Liquids*; Vol. 2: Kinetic Theory; Wiley, New York, second ed., 1987.

[59] Underhill, P. T.; Doyle, P. S., *J. Non-Newtownian Fluid Mech.* **2004**, *122*, 3.

[60] Kim, S.; Panwar, A.; Kumar, S.; Ahn, K.; Lee, S., *J. Chem. Phys.* **2004**, *121*, 9116.

[61] Panwar, A.; Kumar, S., *Macromolecules* **2006**, *39*, 1279.

[62] Öttinger, H. C., *Stochastic Processes in Polymeric Fluids: Tools and Examples for Developing Simulation Algorithms*; Springer, Berlin, 1996.

[63] Groot, R.; Warren, P., *J. Chem. Phys.* **1997**, *107*, 4423.

[64] Lowe, C., *Europhys. Lett.* **1999**, *47*, 145.

[65] Usta, O.; Ladd, A.; Butler, J., *J. Chem. Phys.* **2005**, *122*, 094902.

[66] Succi, S.; Filippova, O.; Smith, G.; Kaxiras, E., *Comput. Sci. Eng.* **2001**, *3*, 26.

[67] Flory, P. J., *Principles of Polymeric Chemistry*; Cornell University Press, Ithica, 1953.

[68] Rubinstein, M.; Colby, R. H., *Polymer Physics*; Oxford University Press, New York, 2003.

[69] Underhill, P. T.; Doyle, P. S., *J. Rheol.* **2006**, *50*, 513.

[70] Underhill, P.; Doyle, P. S., *J. Rheol.* **2005**, *49*, 963.

[71] Woo, N. J.; Shaqfeh, E. S. G.; Khomami, B., *J. Rheol.* **2004**, *48*, 281.

[72] Doyle, P. S.; Shaqfeh, E.; Gast, A., *J. Fluid Mech.* **1997**, *334*, 251.

[73] Jendrejack, R.; Dimalanta, E.; Schwartz, D.; Graham, M.; de Pablo, J., *Phys. Rev. Lett.* **2003**, *91*, 038102.

[74] Jendrejack, R.; Schwartz, D.; Graham, M.; de Pablo, J., *J. Chem. Phys.* **2003**, *119*, 1165.

[75] Jendrejack, R.; Schwartz, D.; de Pablo, J.; Graham, M., *J. Chem. Phys.* **2004**, *120*, 2513.

[76] Long, D.; Dobrynin, A.; Rubinstein, M.; Ajdari, A., *J. Chem. Phys.* **1998**, *108*, 1234.

[77] Kim, S.; Karrila, S. J., *Microhydrodynamics: Principles and Selected Applications*; Dover Publications, New York, 2005.

[78] Long, D.; Viovy, J.; Ajdari, A., *J. Phys. Cond. Matt.* **1996**, *8*, 9471.

[79] Long, D.; Viovy, J.; Ajdari, A., *Biopolymers* **1996**, *39*, 755.

[80] Stigter, D.; Bustamante, C., *Biophys. J.* **1998**, *75*, 1197.

[81] Larson, R., *J. Rheol.* **2005**, *49*, 1.

[82] Jendrejack, R. M.; de Pablo, J. J.; Graham, M. D., *J. Chem. Phys.* **2002**, *116*, 7752.

[83] Dobrynin, A.; Rubinstein, M., *Prog. Polym. Sci.* **2005**, *30*, 1049.

[84] Phillips, K.; Larson, J.; Yantz, G.; D'Antoni, C.; Gallo, M.; Gillis, K.; Goncalves, N.; Neely, L.; Gullans, S.; Gilmanshin, R., *Nucleic Acids Res.* **2005**, *33*, 5829.

[85] Tegenfeldt, J.; Bakajin, O.; Chou, C.; Chan, S.; Austin, R. H.; Fann, W.; Liou, L.; Chan, E.; Duke, T.; Cox, E., *Phys. Rev. Lett.* **2001**, *86*, 1378.

[86] de Gennes, P.-G., *Scaling Concepts in Polymer Physics*; Cornell University Press, Ithica, 1979.

[87] Tegenfeldt, J.; Prinz, C.; Cao, H.; Chou, S.; Reisner, W.; Riehn, R.; Wang, Y.; Cox, E.; Sturm, J.; Silberzan, P.; Austin, R. H., *Proc. Nat. Acad. Sci. U.S.A.* **2004**, *101*, 10979.

[88] Riehn, R.; Lu, M.; Wang, Y.; Lim, S.; Cox, E.; Austin, R. H., *Proc. Nat. Acad. Sci. U.S.A.* **2005**, *102*, 10012.

[89] Smith, S.; Finzi, L.; Bustamante, C., *Science* **1992**, *258*, 1122.

[90] Strick, T.; Allemand, J.; Bensimon, D.; Bensimon, A.; Croquette, V., *Science* **1996**, *271*, 1835.

[91] Wang, M.; Yin, H.; Landick, R.; Gelles, J.; Block, S., *Biophys. J.* **1997**, *72*, 1335.

[92] Minc, N.; Futterer, C.; Dorfman, K.; Bancaud, A.; Gosse, C.; Goubault, C.; Viovy, J., *Anal. Chem.* **2004**, *76*, 3770.

[93] Teclemariam, N. P.; Beck, V. A.; Shaqfeh, E. S. G.; Muller, S. J., *Macromolecules* **2007**, *40*, 3848.

[94] Shaqfeh, E., *J. Non-Newtownian Fluid Mech.* **2005**, *130*, 1.

[95] Larson, J.; Yantz, G.; Zhong, Q.; Charnas, R.; D'Antoni, C.; Gallo, M.; Gillis, K.; Neely, L.; Phillips, K.; Wong, G.; Gullans, S.; Gilmanshin, R., *Lab Chip* **2006**, *6*, 1187.

[96] Kim, J. M.; Doyle, P. S., *Lab Chip* **2007**, *7*, 213.

[97] Balducci, A.; Doyle, P. S., *Macromolecules* **2008**, *41*, 5485.

[98] Dorfman, K., *Phys. Rev. E* **2006**, *73*, 061922.

[99] Mohan, A.; Doyle, P. S., *Phys. Rev. E* **2007**, *76*, 040903.

[100] Kim, J. M.; Doyle, P. S., *J. Chem. Phys.* **2006**, *125*, 074906.

[101] Liu, T., *J. Chem. Phys.* **1989**, *90*, 5826.

[102] Larson, R.; Magda, J., *Macromolecules* **1989**, *22*, 3004.

[103] Smith, D.; Chu, S., *Science* **1998**, *281*, 1335.

[104] Larson, R.; Hu, H.; Smith, D.; Chu, S., *J. Rheol.* **1999**, *43*, 267.

[105] Schroeder, C. M.; Babcock, H. P.; Shaqfeh, E. S. G.; Chu, S., *Science* **2003**, *301*, 1515.

[106] Tang, J.; Doyle, P. S., *App. Phys. Lett.* **2007**, *90*, 224103.

[107] Bustamante, C.; Marko, J.; Siggia, E.; Smith, S., *Science* **1994**, *265*, 1599.

[108] Barrat, J.; Joanny, J., *Adv. Chem. Phys.* **1996**, *94*, 1.

[109] Balducci, A.; Mao, P.; Han, J.; Doyle, P. S., *Macromolecules* **2006**, *39*, 6273.

[110] Heyes, D.; Melrose, J., *J. Non-Newtownian Fluid Mech.* **1993**, *46*, 1.

[111] Chou, C.; Tegenfeldt, J.; Bakajin, O.; Chan, S.; Cox, E.; Darnton, N.; Duke, T.; Austin, R. H., *Biophys. J.* **2002**, *83*, 2170.

[112] Regtmeier, J.; Duong, T. T.; Eichhorn, R.; Anselmetti, D.; Ros, A., *Anal. Chem.* **2007**, *79*, 3925.

[113] Petersen, E.; Li, B.; Fang, X.; Luo, H.; Samuilov, V.; Gersappe, D.; Sokolov, J.; Chu, B.; Rafailovich, M., *Phys. Rev. Lett.* **2007**, *98*, 088102.

[114] Parikesit, G.; Markesteijn, A.; Piciu, O.; Bossche, A.; Westerweel, J.; Young, I.; Garini, Y., *Biomicrofluidics* **2008**, *2*, 024103.

[115] Ajdari, A.; Prost, J., *Proc. Nat. Acad. Sci. U.S.A.* **1991**, *88*, 4468.

[116] Bowers, J.; Prudhomme, R., *J. Chem. Phys.* **1992**, *96*, 7135.

[117] Kaji, N.; Tezuka, Y.; Takamura, Y.; Ueda, M.; Nishimoto, T.; Nakanishi, H.; Horiike, Y.; Baba, Y., *Anal. Chem.* **2004**, *76*, 15.

[118] Jo, K.; Dhingra, D. M.; Odijk, T.; de Pablo, J. J.; Graham, M. D.; Runnheim, R.; Forrest, D.; Schwartz, D. C., *Proc. Nat. Acad. Sci. U.S.A.* **2007**, *104*, 2673.

[119] Laachi, N.; Cho, J.; Dorfman, K. D., *Phys. Rev. E* **2009**, *79*, 031928.

[120] Dorfman, K. D., *Under Review* .

[121] Duke, T.; Austin, R. H.; Cox, E.; Chan, S., *Electrophoresis* **1996**, *17*, 1075.

[122] Ou, J.; Cho, J.; Olson, D. W.; Dorfman, K. D., *Phys. Rev. E* **2009**, *79*, 061904.

[123] Gardiner, C. W., *Handbook of Stochastic Methods for Physics, Chemistry, and the Natural Sciences*; Springer, New York, 1983.

[124] Abramowitz, M.; Stegun, I. A., *Handbook of Mathematical Functions*; Dover Publications, New York, 1964.

[125] Squires, T.; Bazant, M., *J. Fluid Mech.* **2004**, *509*, 217.

[126] Reisner, W.; Morton, K. J.; Riehn, R.; Wang, Y. M.; Yu, Z.; Rosen, M.; Sturm, J. C.; Chou, S. Y.; Frey, E.; Austin, R. H., *Phys. Rev. Lett.* **2005**, *94*, 196101.

[127] Reccius, C. H.; Mannion, J. T.; Cross, J. D.; Craighead, H. G., *Phys. Rev. Lett.* **2005**, *95*, 268101.

[128] Hsieh, C.-C.; Balducci, A.; Doyle, P. S., *Macromolecules* **2007**, *40*, 5196.

[129] Fisher, J. K.; Ballenger, M.; O'Brien, E. T.; Haase, J.; Superfine, R.; Bloom, K., *Proc. Nat. Acad. Sci. U.S.A.* **2009**, *106*, 9250.

[130] Grassia, P.; Hinch, E. J., *J. Fluid Mech.* **1996**, *308*, 255.

[131] Doyle, P. S.; Shaqfeh, E. S. G.; McKinley, G. H.; Spiegelberg, S. H., *J. Non-Newtonian Fluid Mech.* **1998**, *76*, 79.

[132] Dimitrakopoulos, P., *J. Fluid Mech.* **2004**, *513*, 265.

[133] Doi, M.; Edwards, S., *The Theory of Polymer Dynamics*; Oxford University Press, New York, 1986.

[134] Milchev, A.; Binder, K., *J. Phys. II (France)* **1996**, *6*, 21.

[135] Hagita, K.; Koseki, S.; Takano, H., *J. Phys. Soc. Japan* **1999**, *68*, 2144.

[136] Stigter, D., *Biophys. Chem.* **2002**, *101*, 447.

[137] Tang, J.; Trahan, D. W.; Doyle, P. S., *Macromolecules* **2010**, *43*, 3081.